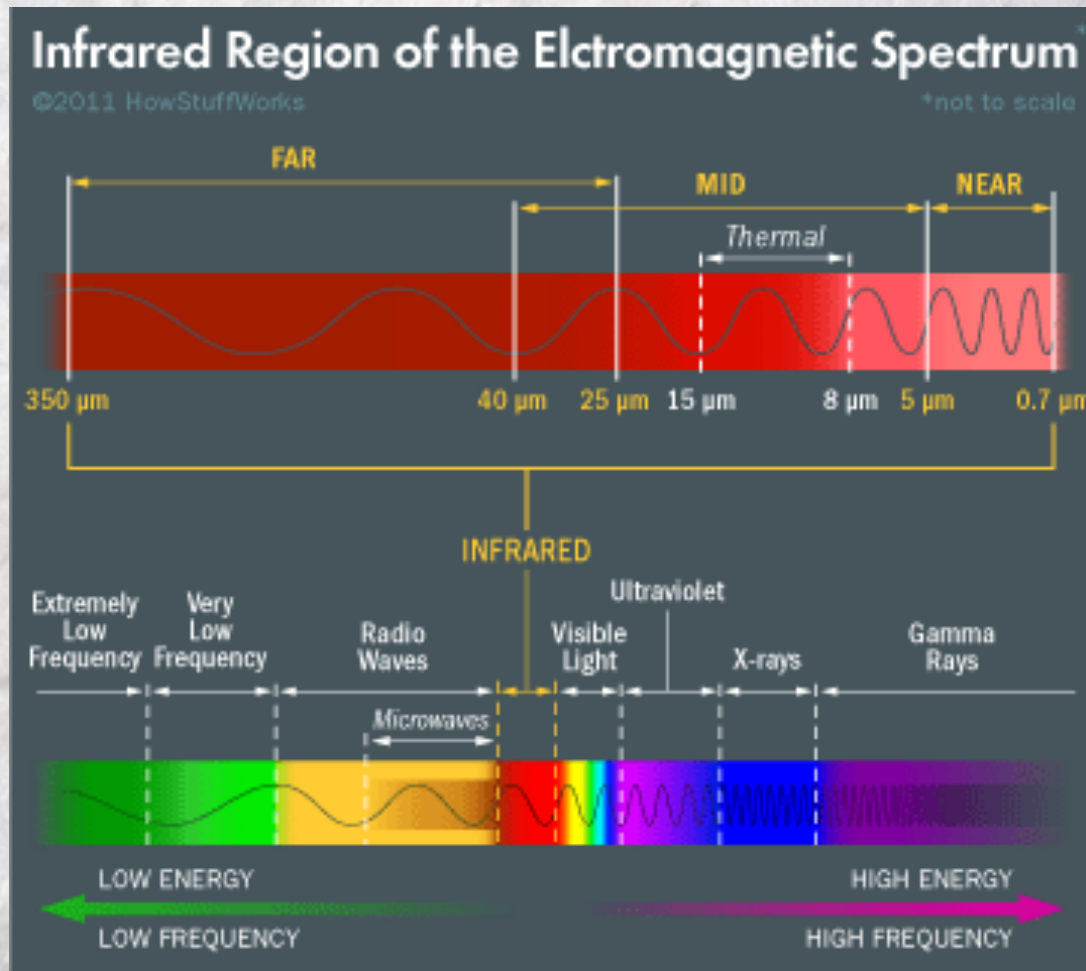# The infrared range corresponds to vibrational energies in molecules and solids
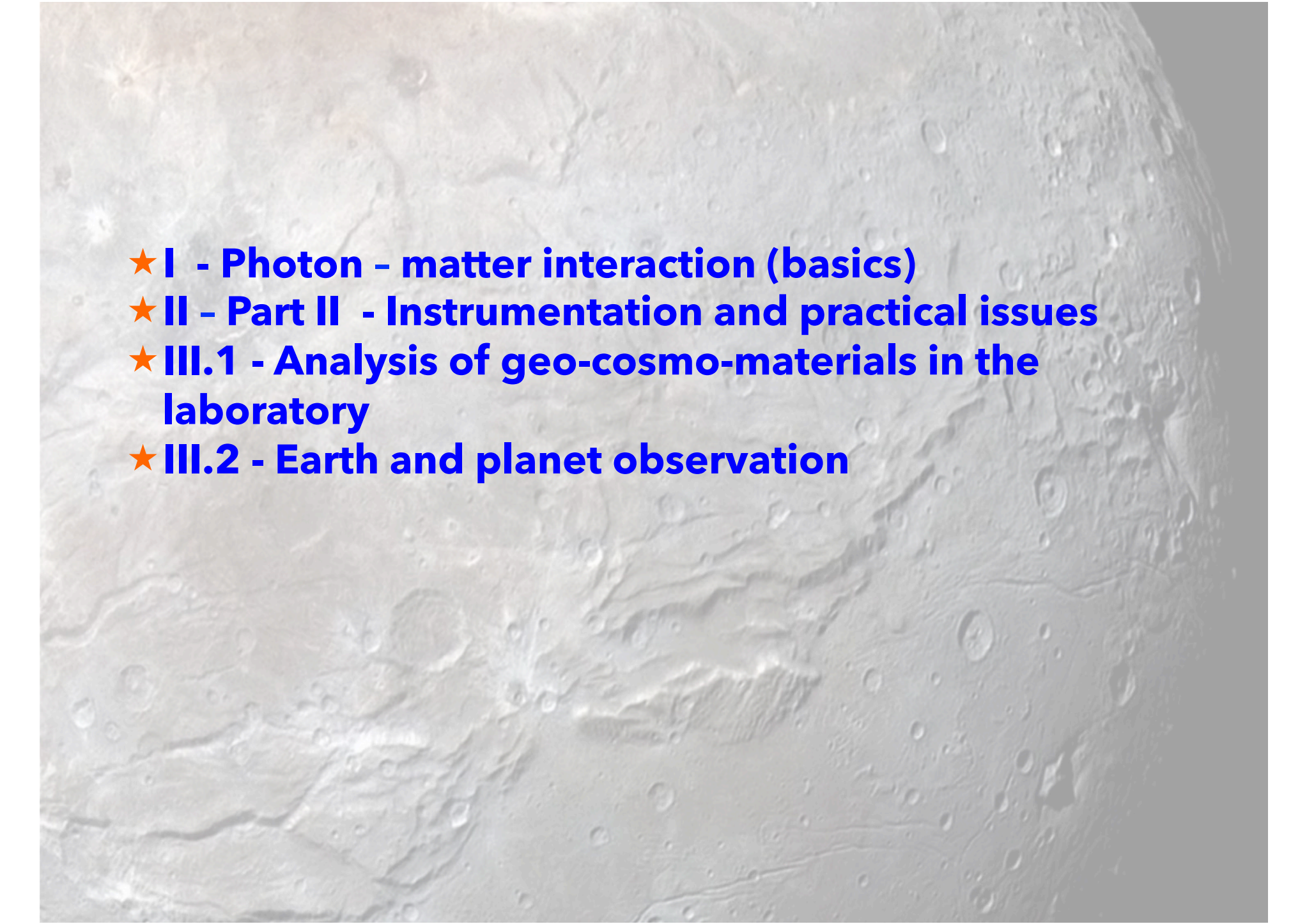

Infrared Region of the Electromagnetic Spectrum
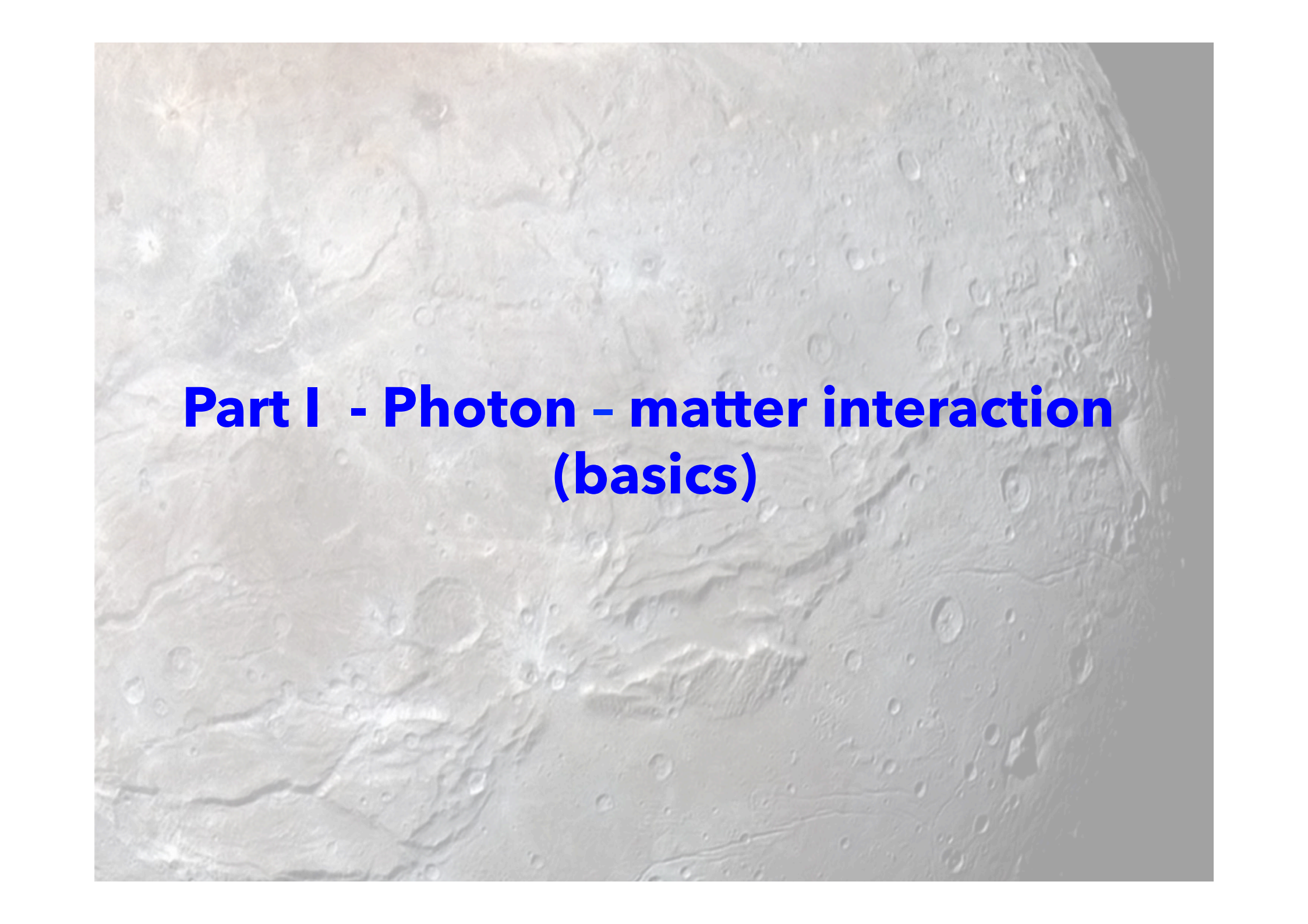
... but not forget thermal emission!

Spatial resolution: 100s km to 40 nm

The HOLY GRAIL of chemical microscopy

High — MRI

IR
RM

AFM-IR
Raman-TERS

STXM

Chemical Information Content

XPS

EDS

EELS

FM

TEM

NSOM   SEM

OM

STM

AFM

Low

| 10 μm | 1 μm | 50 nm | 1 nm | 1 Å |

Spatial Resolution →
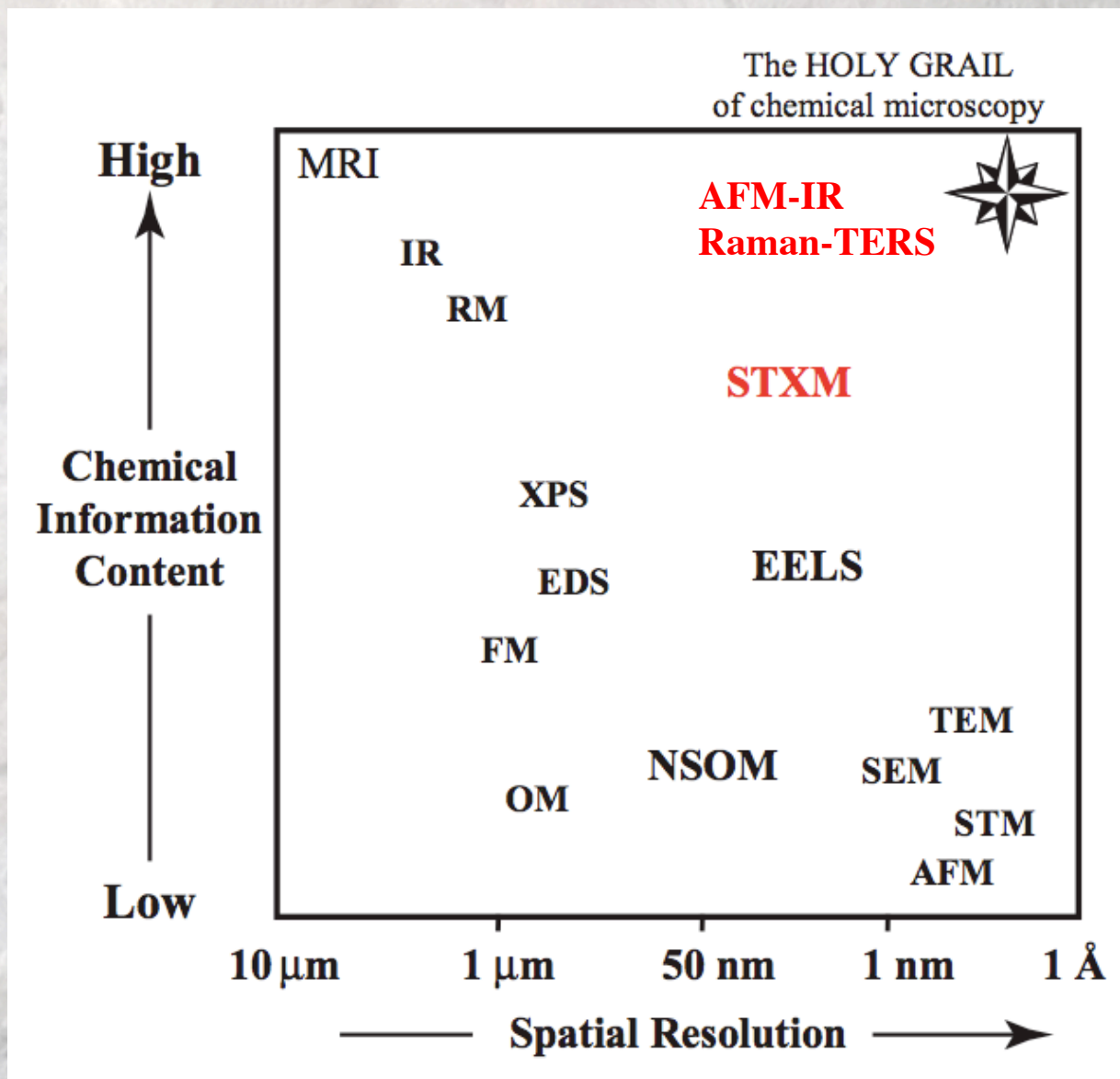
★ **I - Photon – matter interaction (basics)**
★ **II – Part II - Instrumentation and practical issues**
★ **III.1 - Analysis of geo-cosmo-materials in the laboratory**
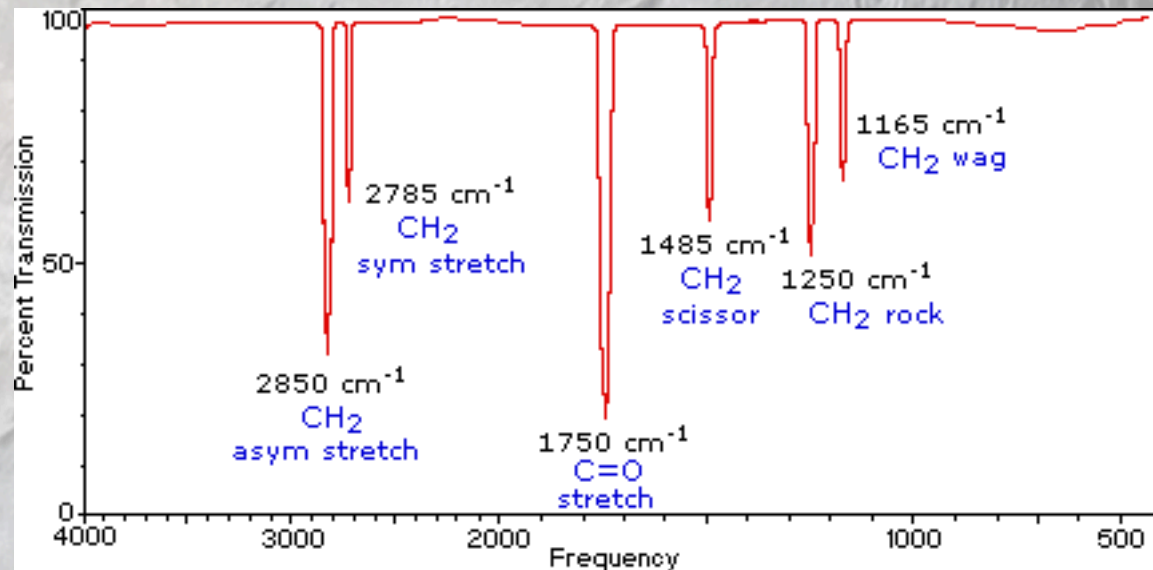★ **III.2 - Earth and planet observation**

Part I - Photon – matter interaction (basics)

Part I - Photon – matter interaction (basics)
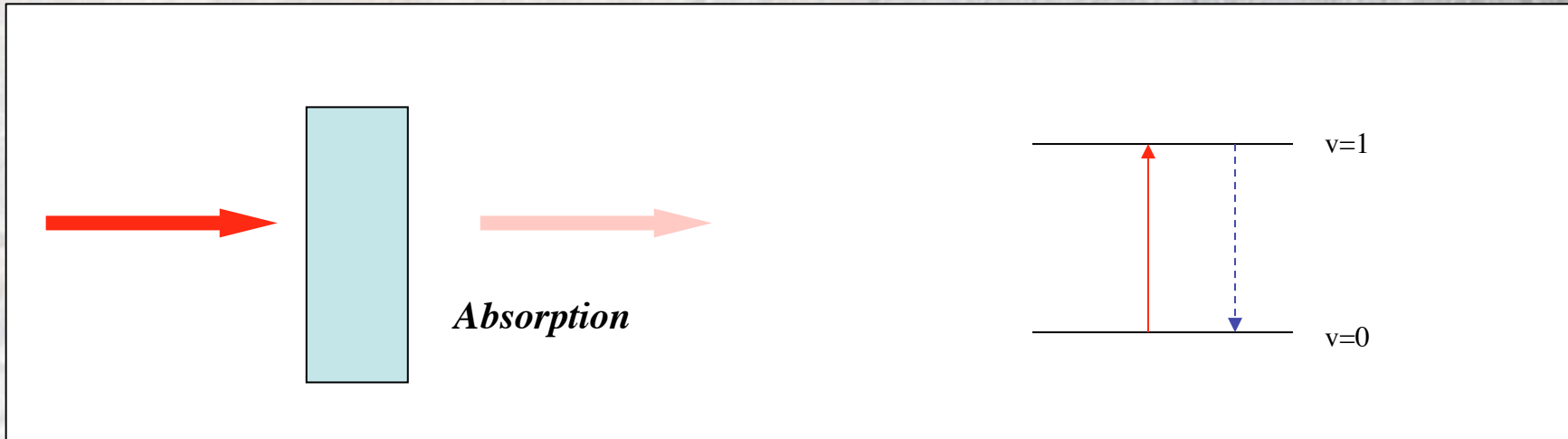
Transmitance : $T = \dfrac{I}{I_0}$

Absorbance : $A = -\log(\dfrac{I}{I_0})$

Optical constants also characterize optical properties of solids and liquids

- **Teledetection surface models**
- **Atmospheric models (radiative transfer)**

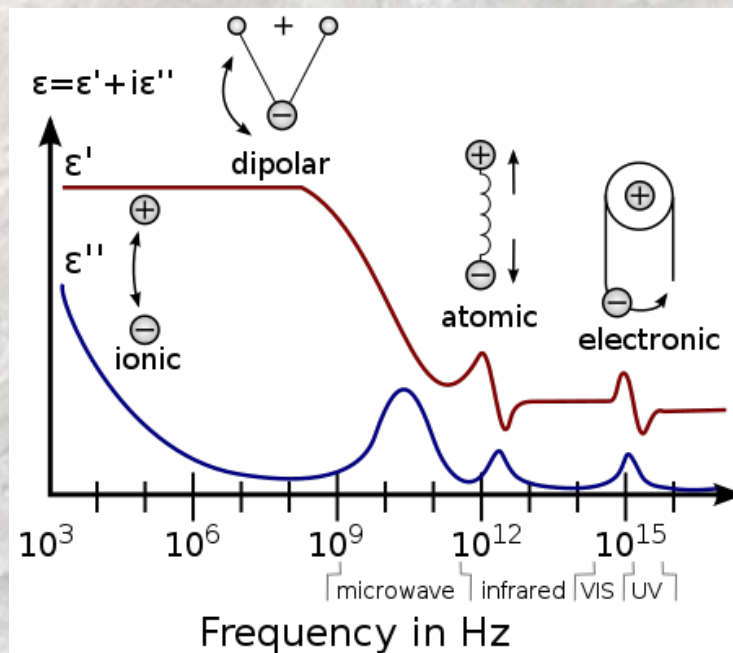$$\vec{P} = \epsilon_0 \chi_e \vec{E} \quad \vec{P} = \epsilon_0 \int_{-\infty}^{t} \chi(t - t')\vec{E}(t')dt'$$

$$\vec{P}(\omega) = \epsilon_0 \chi_e(\omega)\vec{E}(\omega)$$

$$\chi(\omega) = \chi_1(\omega) + i\chi_2(\omega)$$

$$\chi_1(\omega) = \frac{1}{\pi}\mathcal{P}\int_{-\infty}^{\infty} \frac{\chi_2(\omega')}{\omega' - \omega}\,d\omega'$$

and

$$\chi_2(\omega) = -\frac{1}{\pi}\mathcal{P}\int_{-\infty}^{\infty} \frac{\chi_1(\omega')}{\omega' - \omega}\,d\omega'$$

$$\vec{E} = \vec{E}_0 e^{i\left(\frac{2\pi}{\lambda}(\tilde{n})x - \omega t\right)}$$

$$\varepsilon_r = 1 + \sum_j \frac{Ne^2}{\varepsilon_0 m\left[\left(\omega_j^2 - \omega^2\right) - i\gamma\omega\right]} = \varepsilon' + i\varepsilon''$$

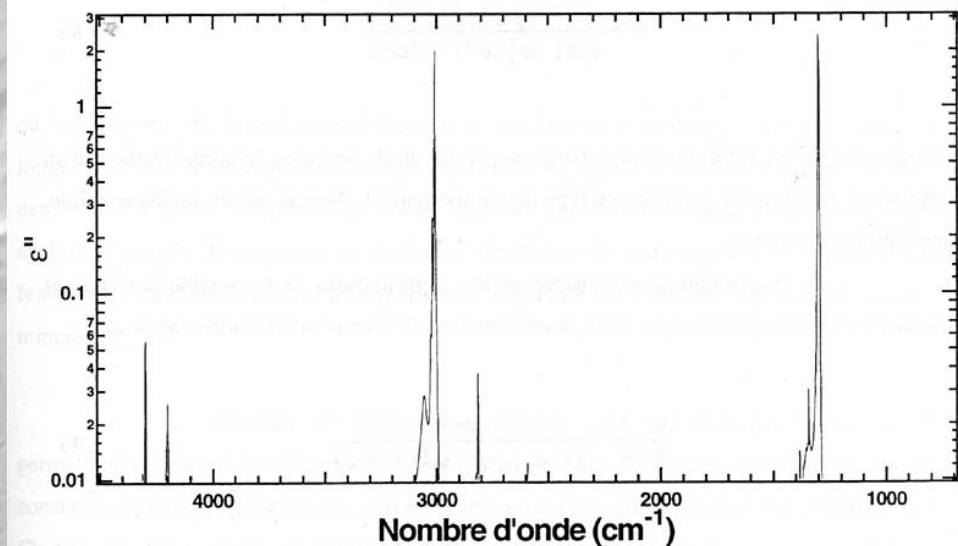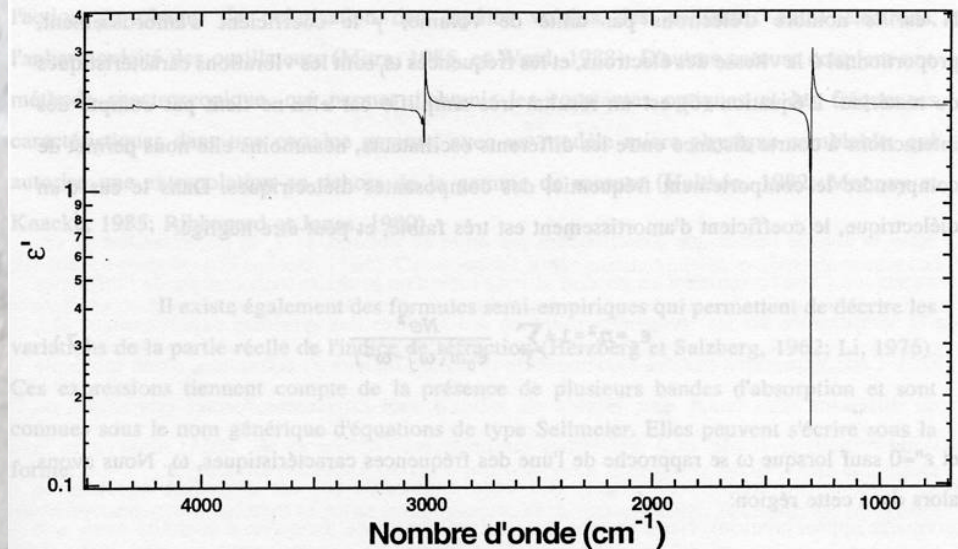$$\tilde{n} = n + ik \qquad \alpha = \frac{4\pi k}{\lambda}$$
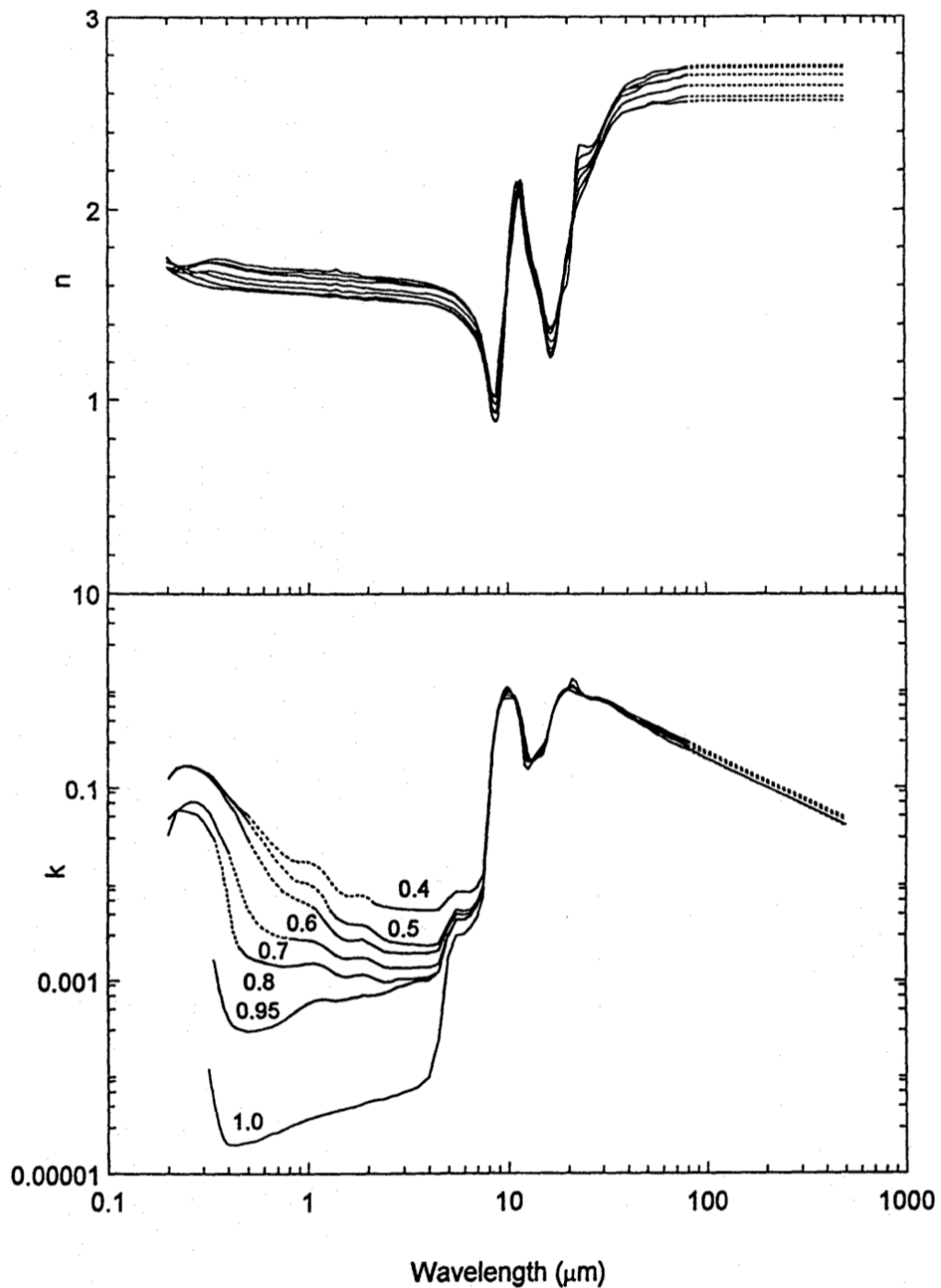
$$\tilde{n}^2 = 1 + \chi(\omega) = \epsilon_r$$

$$\vec{D} = \epsilon_r \epsilon_0 \vec{E} = (\epsilon' + i\epsilon'')\vec{E}$$

Relations de Kramers-Krönig :

$$n(\nu) = 1 + \frac{2}{\pi} P \int_0^\infty \frac{\nu' k(\nu')}{\nu'^2 - \nu^2} d\nu'$$

$$k(\nu) = \frac{2\nu}{\pi} P \int_0^\infty \frac{n(\nu')}{\nu^2 - \nu'^2} d\nu'$$

ε' — Nombre d'onde (cm^{-1})

ε'' — Nombre d'onde (cm^{-1})

Fig. 4. Optical constants n (top) and k (bottom) of the pyroxene glasses of the compositions $Mg_xFe_{1-x}SiO_3$ for x=0.4, 0.5, 0.6, 0.7, 0.8, 0.95 and 1.00. Both in the UV/VIS/NIR and in the FIR beyond the vibrational bands, the n curves clearly fan out according to the iron content of the samples (increasing n values with growing iron content). Note the huge fanning out of the k curves (logarithmic scale!). For the sake of clearness, in the lower graph, the curves are labelled by the index x of the formula. In both graphs, dotted lines indicate regions of interpolation and/or extrapolation

Loi de Beer-Lambert

$$dI = -I\alpha\,dx$$

✓Établie pour l'étude des solutions diluées
✓Milieu latéralement homogène
✓Faisceau rigoureusement collimaté
✓Extrapolation aux phases condensées
✓Conditions spécifiques

I_0 → □ → I
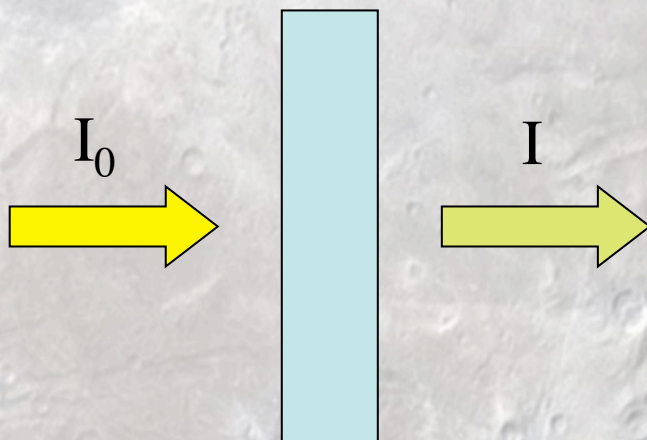
Transmitance : $T = \dfrac{I}{I_0}$

Absorbance : $A = -\log(\dfrac{I}{I_0})$

α : coefficient d'extinction cm^{-1}
e : épaisseur
N : mol.cm^{-3}
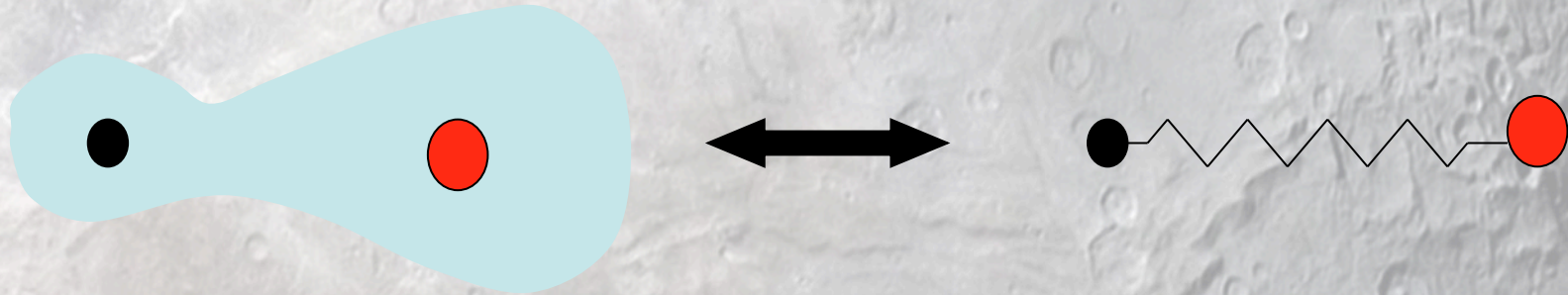σ : section efficace d'absorption cm^2/mol

$$I = I_0 \exp(-\alpha e)$$

$$I = I_0 \exp(-Ne\sigma)$$

$$A = \dfrac{\alpha e}{\ln 10}$$

Born-Oppenheimer approximation

Decoupling of electronic, vibrationnal and rotational motions
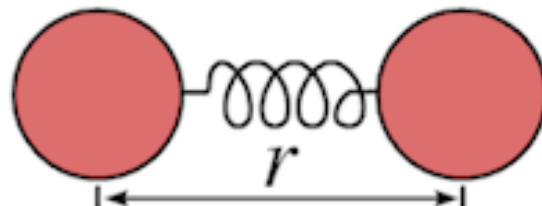
$$H = T_N + T_e + V_{ee} + V_{NN} + V_{eN}$$
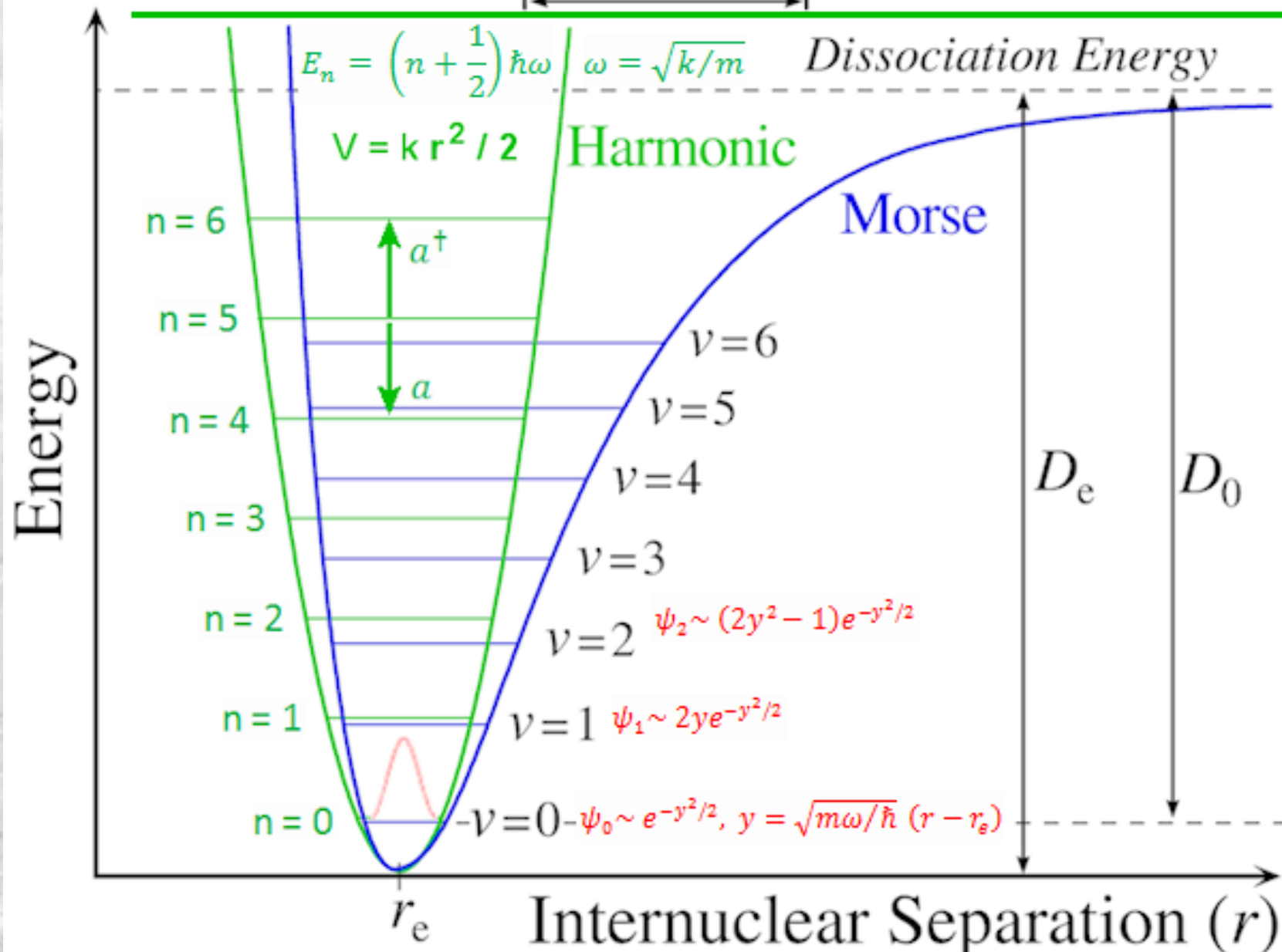
$$m\ddot{x} = -kx$$

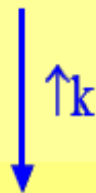$$\ddot{x} + \omega^2 x = 0$$

$$x(t) = A.\cos(\omega t + \varphi)$$

$$\nu = \frac{1}{2\pi}\sqrt{\frac{k}{\mu}}$$

$$\mu = \frac{m_A m_B}{m_A + m_B}$$

- ν : frequency vibration
- μ : reduced mass
- k : bonding strength
- m_A et m_B : masses of atoms A and B

C-C	1200 cm^{-1}
C=C	1650 cm^{-1}
C≡C	2150 cm^{-1}

↑k

Liaison:	≡C-H	=C-H	-C-H
Fréquence:	~3300 cm^{-1}	~3100 cm^{-1}	~2900 cm^{-1}
k (N.m^{-1}):	593	523	458
Type de liaison:	sp-s	sp^2-s	sp^3-s
Longueur (Å):	1,08	1,10	1,12

$$\overline{\nu}\ [cm^{-1}] = \frac{1}{2\pi c} \sqrt{\frac{k}{\mu}}$$

μ dependency

Liaison	$\overline{\nu}$ (cm^{-1})	m_2 (g)	μ (g)
C-H	3000	1	0,923
C-C	1200	12	6,000
C-O	1100	16	6,857
C-Cl	800	35,5	8,968
C-Br	550	80	10,43
C-I	~500	127	10,96

$\uparrow \mu$
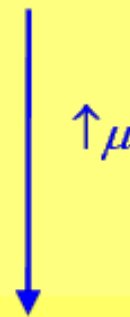
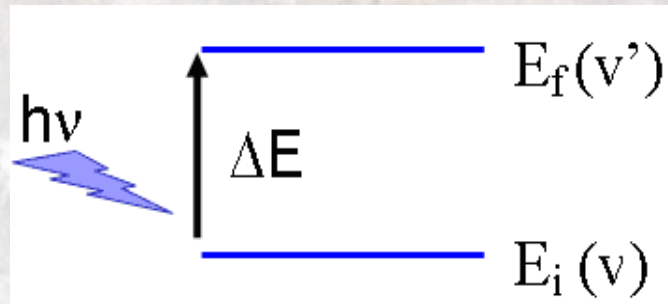# Oscillateur anharmonique

$$U_{kk}(R) = \frac{1}{2}k(R-R_e)^2 + k_3(R-R_e)^3 + \dots$$

$$G_v = \omega_e(v+\frac{1}{2}) - \omega_e x_e(v+\frac{1}{2})^2 + \omega_e x_e y_e(v+\frac{1}{2})^3 + \dots$$
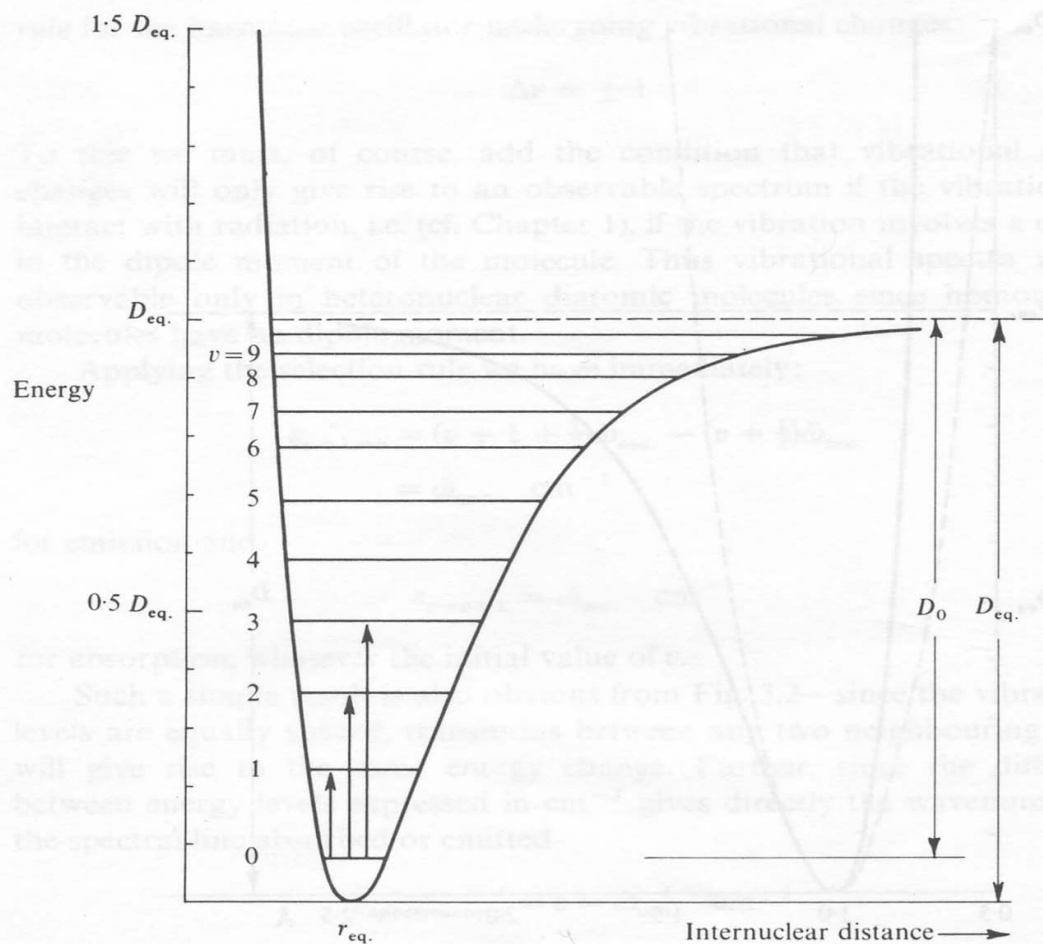
Absorption = Interaction of electric field with charges

$E_f(v')$

$h\nu$ ΔE

$E_i(v)$

$$W = \vec{\mu} . \vec{E}$$

Dipolar transition

$$\langle m|W|k \rangle = \langle m|e\phi|k \rangle - \boxed{\langle m|\boldsymbol{\mu} \cdot \mathbf{E}|k \rangle}$$

$$- \langle m|\frac{1}{2} e \sum_{ij} x_i x_j \frac{\partial E_j}{\partial x_i}|k \rangle + \cdots$$

$$= 0 - \mathbf{E} \cdot \langle m|\boldsymbol{\mu}|k \rangle - \frac{1}{2} \sum_{ij} e \frac{\partial E_j}{\partial x_i} \langle m|x_i x_j|k \rangle + \cdots$$

Electric anharmonicity

$$\langle v|\boldsymbol{\mu}(R)|v'\rangle = \boldsymbol{\mu}(R_e)\langle v|v'\rangle + \left(\frac{\partial \boldsymbol{\mu}}{\partial R}\right)_{R_e}\langle v|(R - R_e)|v'\rangle$$

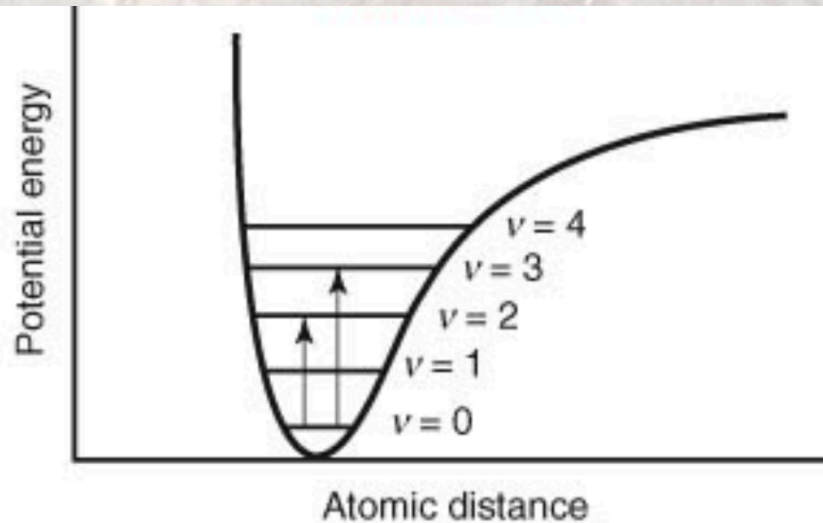$$+ \frac{1}{2}\left(\frac{\partial^2 \boldsymbol{\mu}}{\partial R^2}\right)_{R_c}\langle v|(R - R_e)^2|v'\rangle + \cdots$$

$$\langle v|(R - R_e)|v'\rangle = i\left(\frac{\hbar}{2\mu_N\omega}\right)^{1/2}[\sqrt{v+1}\,\delta_{v,v'-1} - \sqrt{v}\,\delta_{v,v'+1}] \quad \Delta v = \pm 1$$

$$\langle v|(R - R_e)^2|v'\rangle = -\frac{\hbar}{2\mu_N\omega}\langle v|aa - a^+a - aa^+ + a^+a^+|v'\rangle \quad \Delta v = \pm 2$$

$$\cdots$$

$$\Delta v = \pm n$$

Selection rules

$$\Delta v = \pm n$$

0-1 Fundamental
0-2 First overtone
0-3 Second overtone

Table 3.2 Vibrational constants of diatomic molecules, cm^{-1}

Molecule	ω_e	$\omega_e x_e$	$\omega_e y_e$
$^{40}Ar_2$	25.74		
$^{138}Ba^{16}O$	669.76	2.02	-0.003
$^{12}C^{16}O$	2169.81358	13.28831	0.010511
$^{1}H_2$	4401.21	121.33	0.812
$^{1}H^{35}Cl$	2990.946	52.8186	0.2243
$^{127}I_2$	214.50	0.614	
$^{127}I^{35}Cl$	384.29	1.501	
$^{23}Na^{35}Cl$	366.0	2.0	
$^{23}Na^{1}H$	1172.2	19.72	0.160
$^{23}Na_2$	159.12	0.7254	-0.00109
$^{14}N_2$	2358.57	14.32	-0.00226
$^{14}N^{16}O$	1904.20	14.075	0.011
$^{16}O_2$	1580.19	11.98	0.0474
$^{16}O^{1}H$	3737.76	84.881	0.540

Data taken from K. P. Huber and G. Herzberg, *Molecular and Molecular Structure: Constants of Diatomic Molecules*, Van Nostrand-Reinhold, New York, 1979.
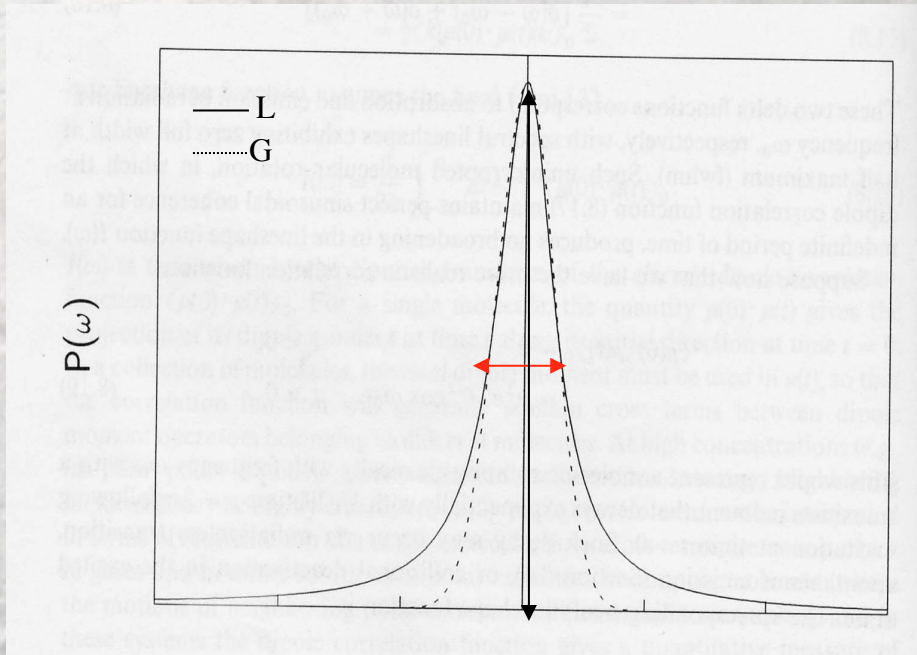
Line and Band

v=1

v=0
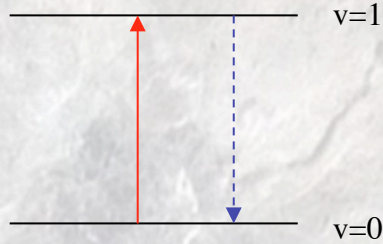
Transition between two levels: **Lorentziand profil**

$$L(\omega) = \frac{\gamma}{2\pi} \frac{1}{(\omega - \omega_0)^2 + \gamma^2/4}$$

$$\gamma = \gamma_{rad} + \gamma_{nonrad} + \gamma_{coll} + \dots$$

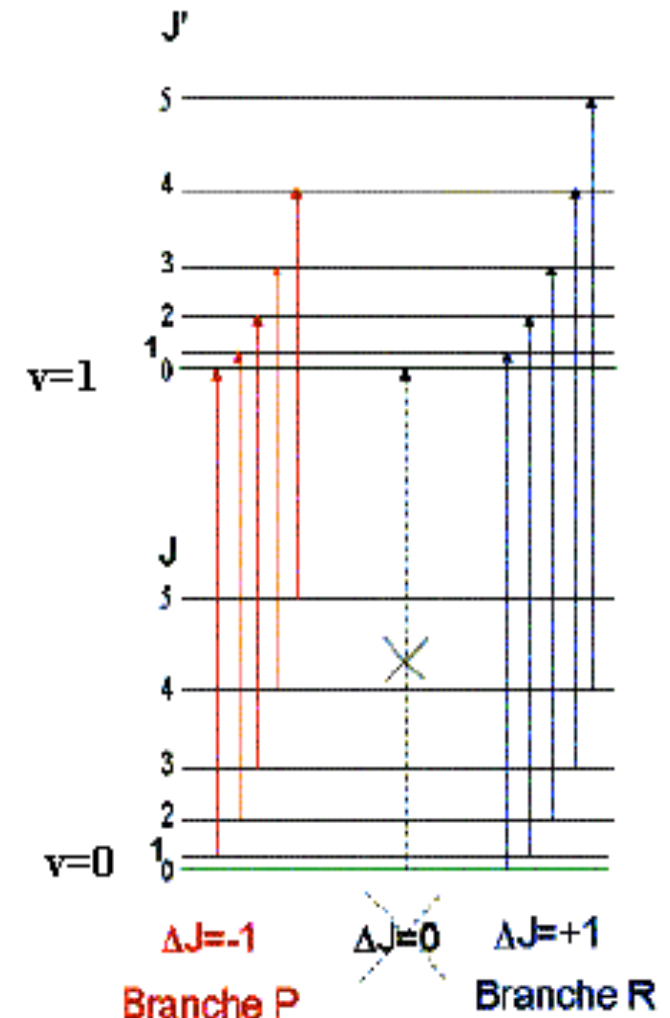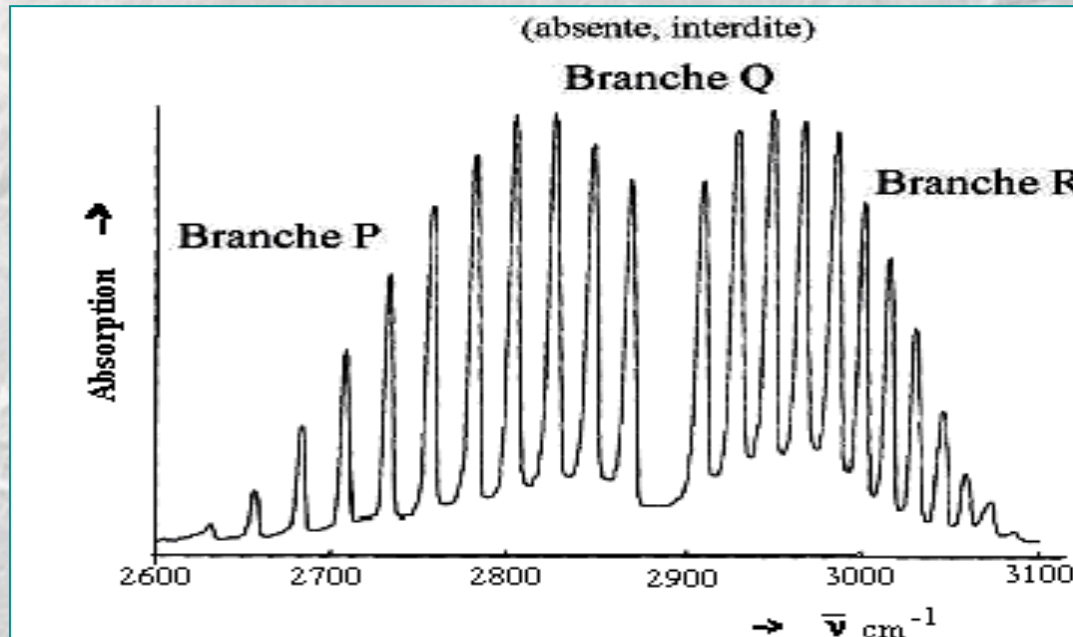Intensity = strength of coupling

$$FWHM \propto \frac{1}{\gamma}$$

Absorption band

✓Series of lines
✓Distribution discrète (low P gas)
✓Continuum (liquid/solid)

$$E = \frac{h^2}{8\pi^2 I} J(J + 1) + \frac{h}{2\pi} \sqrt{\frac{k}{\mu}} (v + \frac{1}{2})$$

ΔJ=±1

2 Series = Two branchs

Inhomogeneous broadening

$$P_V(\omega) = \int_{-\infty}^{\infty} P_G(\omega - \omega')P_L(\omega')d\omega'$$

Gas (Maxwellian distribution)

Heterogeneity in the solid
- Impurities
- defects
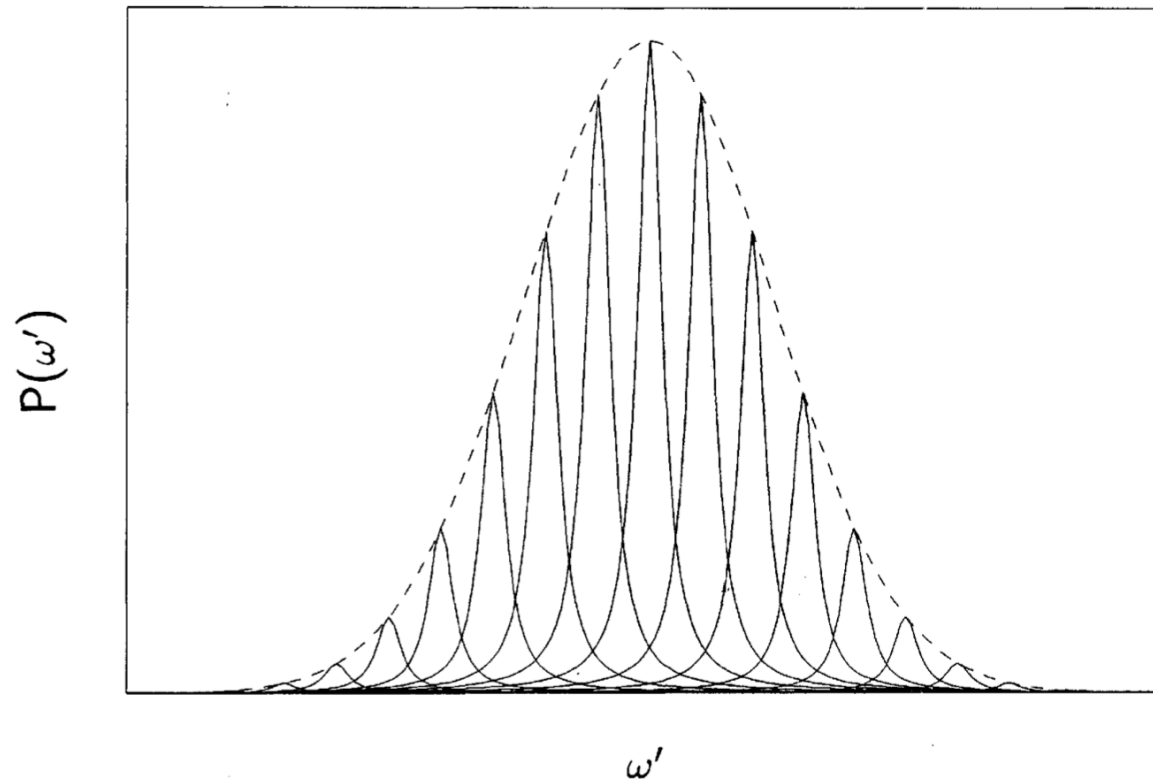
Figure 8.2 The Voigt profile, formed by the convolution (8.29) of the Gaussian profile with the Lorentzian profile, effectively sums Lorentian profiles (solid curves) centered at all frequencies ω', weighted by the value of the Gaussian profile (dashed curve) at those frequencies.

Polyatomic molecules

N atoms : 3N-6 or 3N-5 (linear) vibrations

Harmonic assumption:
* 3N-6 (5) independant oscillators
* Normal coordinates = lin. Comb. of atomic coordinates

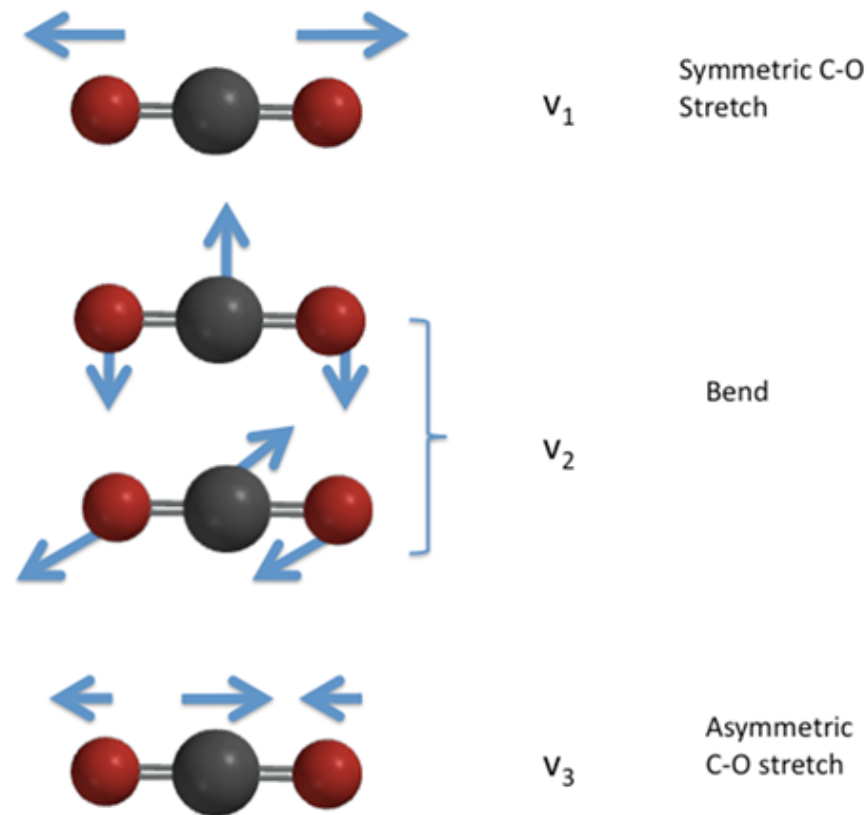$$\eta_i = \xi_i \sqrt{m_i}$$

$$\frac{d}{dt}(\dot{\eta}_i) + \sum_j b_{ij}\eta_j = 0$$

$$\eta_i = \sum_j^{3N} M_{ij}q_j$$

$$T = \frac{1}{2}\sum_i^{3N} \dot{\eta}_i^2$$

$$H = T + V = \sum_i^{3N-6}(\dot{Q}_1^2 + \lambda_i Q_i^2)$$

$$|\psi_{vib}(Q_1, \ldots, Q_{3N-6})\rangle = \prod_i^{3N-6} N_{v_i}H_{v_i}(\zeta_i)\exp(-\zeta_i^2/2)$$

$$\ddot{Q}_i + \lambda_i Q_i = 0 \qquad i = 1, \ldots, 3N$$

$$Q_i = Q_i^0 \sin(t\sqrt{\lambda_i} + \delta)$$

$$E_{vib} = \sum_i^{3N-6} h\nu_i(v_i + \tfrac{1}{2})$$

Polyatomic molecules

N atoms : 3N-6 or 3N-5 (linear) vibrations

Harmonic assumption:
* 3N-6 (5) independant oscillators
* Normal coordinates = lin. Comb. of atomic coordinates

Fig. 1 Vibrational modes of CO_2

CH$_4$: ponctual group T$_d$

Mode	Fréquence (cm^{-1})	Symétrie	
ν_1	2914.2	A$_1$	
ν_2	1526.0	E	
ν_3	3020.3	F$_2$	IR
ν_4	1306.2	F$_2$	IR
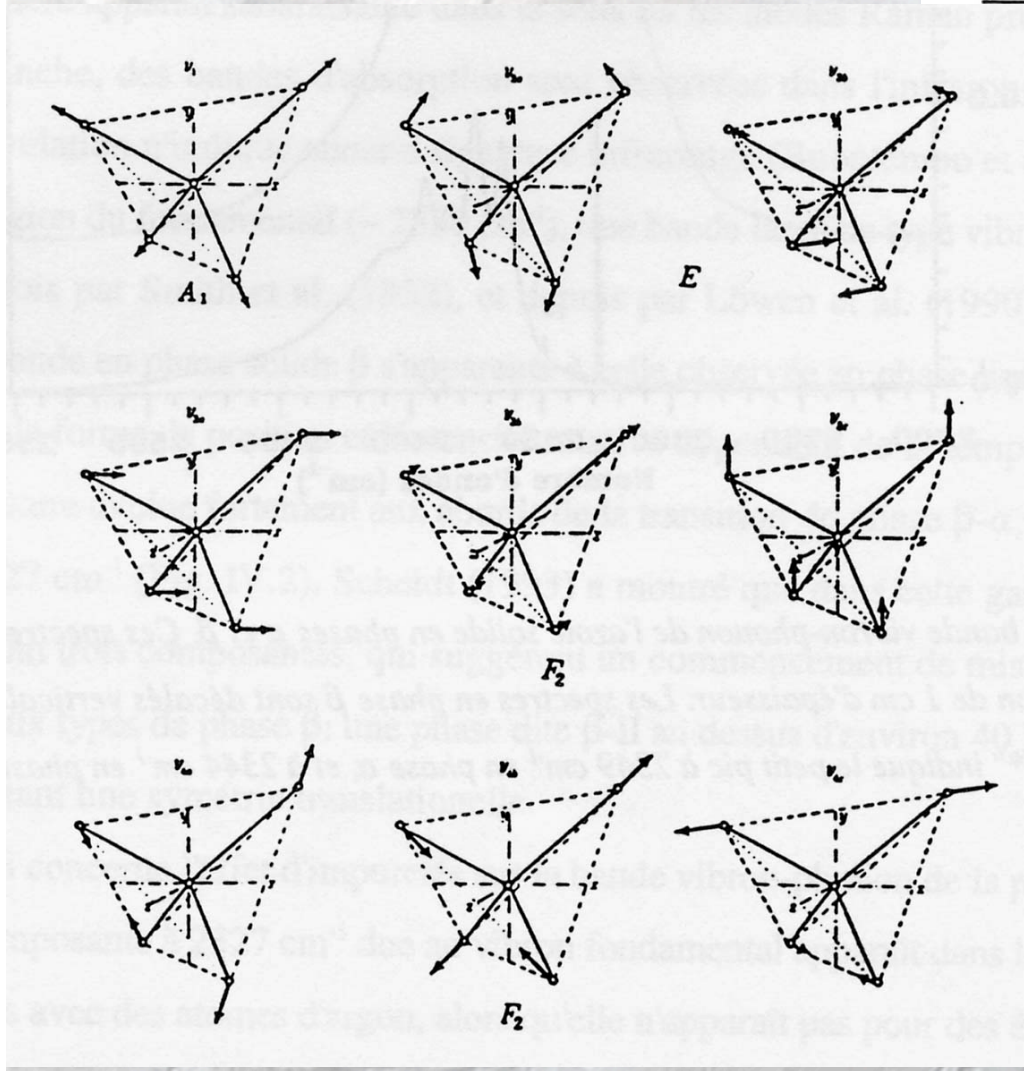
Degeneracy:
- Two modes same energy

IR activity:
- Role of symetry

C_{2v}	E	$C_2(z)$	σ_v	σ'_v		
A_1	1	1	1	1	z	x^2, y^2, z^2
A_2	1	1	-1	-1	R_z	xy
B_1	1	-1	1	-1	x, R_y	xz
B_2	1	-1	-1	1	y, R_x	yz

A₁ **A₁** **B₂**

v_1 3652cm⁻¹ v_2 1595cm⁻¹ v_3 3756cm⁻¹
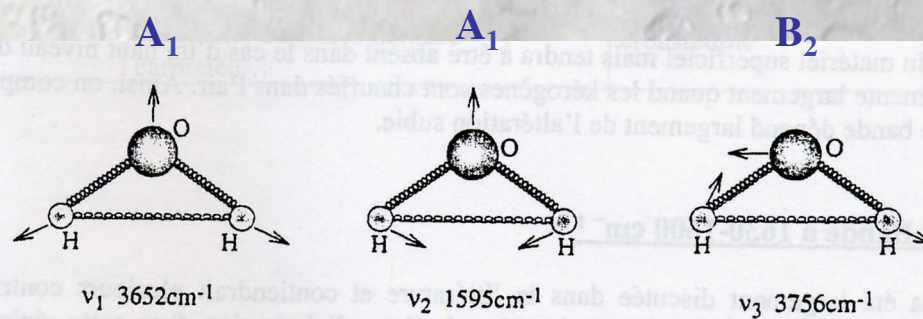
schéma des différents modes de vibration de la molécule d'eau

   v_1 : stretching symétrique
   v_2 : stretching asymétrique
   v_3 : bending

Overtones and combination modes
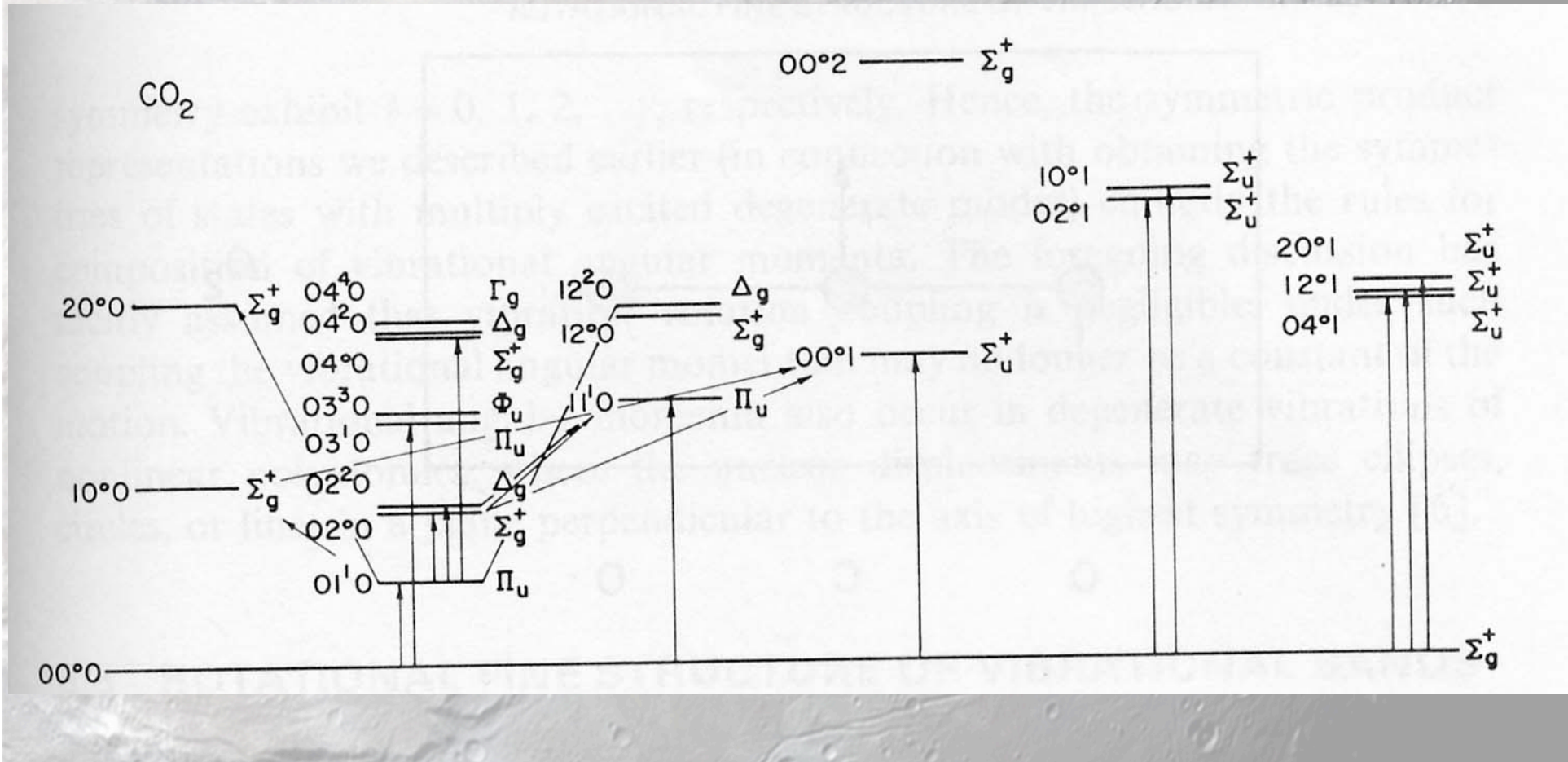
Molecular motion types

Methylene : $-CH_2$

Vibrations de *déformation*
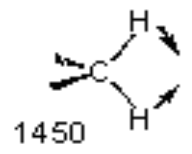
Cisaillement (scissoring) δ	Rotation (rocking) r	Balancement (wagging) ω	Torsion (twisting) t ou τ
1450	750	1300	1200
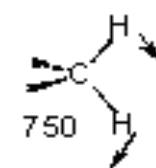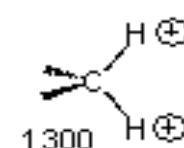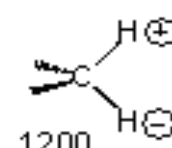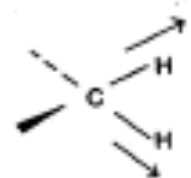
symétrique (~2853 cm⁻¹)
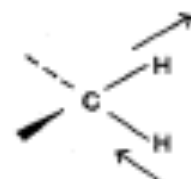
asymétrique (~2926 cm⁻¹)

élongation
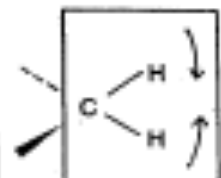
scissoring (~1450 cm⁻¹)
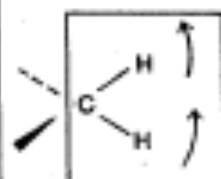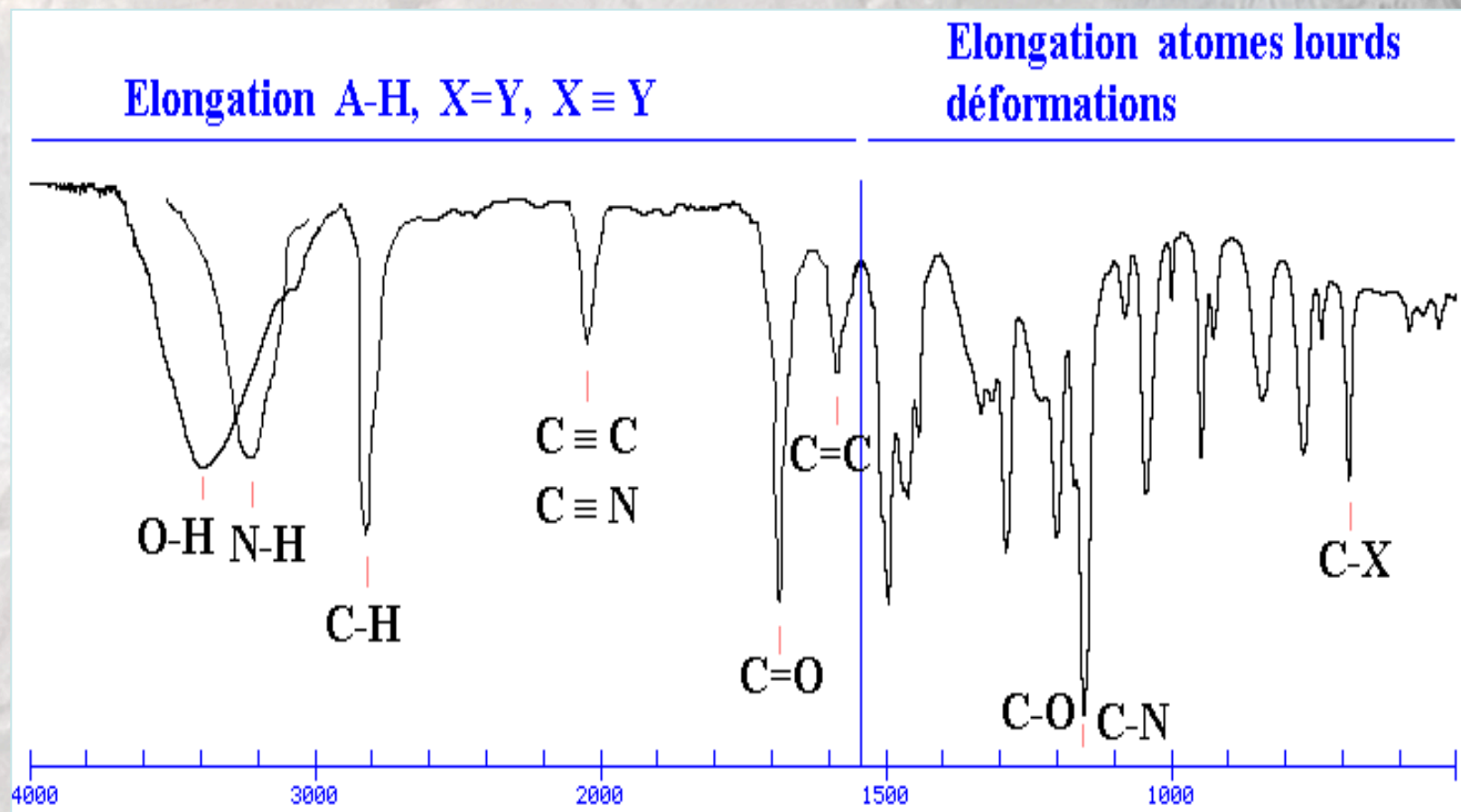
rocking (~720 cm⁻¹)

dans le plan
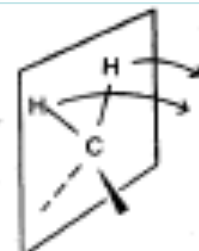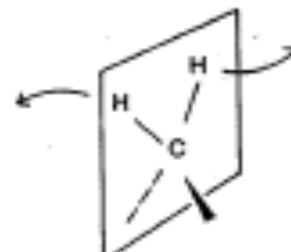
wagging (~1250 cm⁻¹)

twisting (~1250 cm⁻¹)

hors plan

déformation
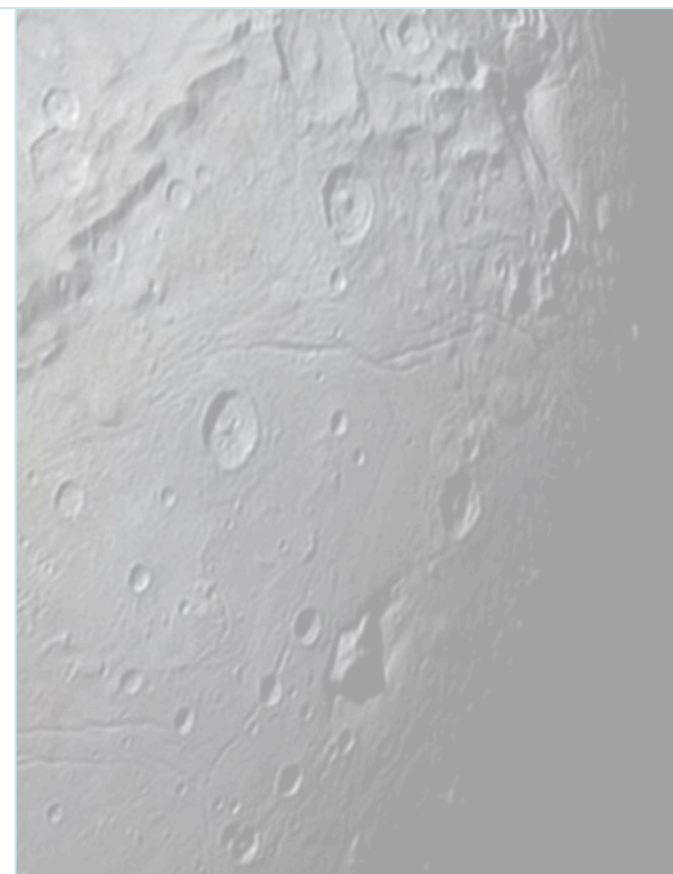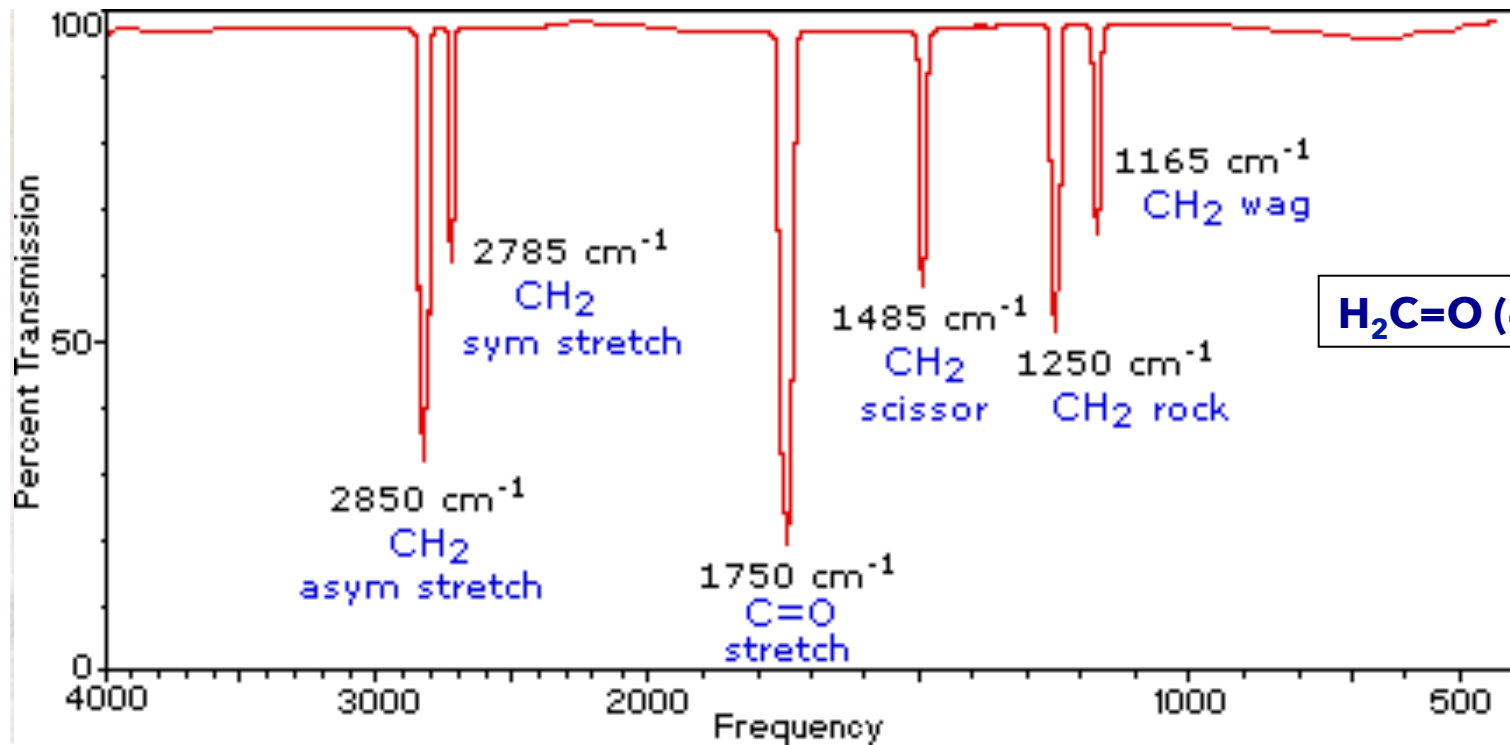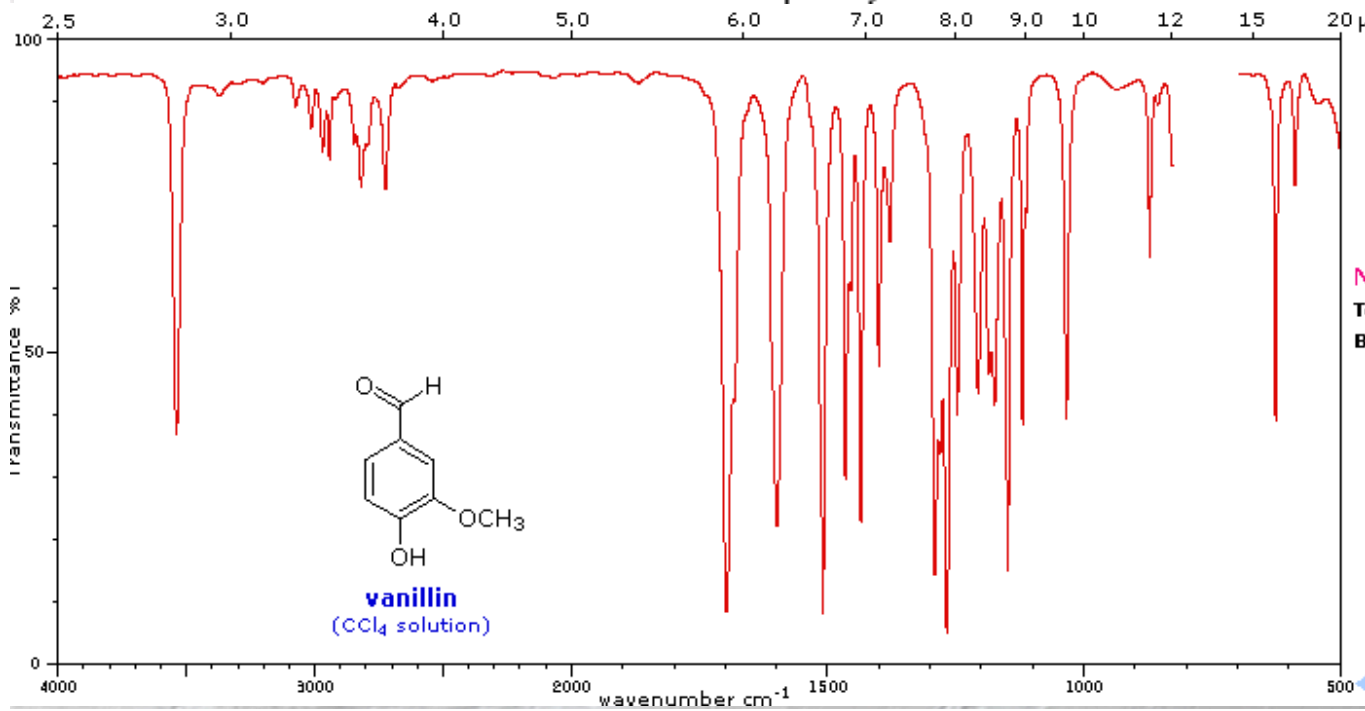
Group vibrations and fingerprint region

Tables compute band position, intensity and IR/Raman activity

H₂C=O (4 atoms - 6 modes)

Upper spectrum labels:
- 2785 cm⁻¹ CH₂ sym stretch
- 2850 cm⁻¹ CH₂ asym stretch
- 1750 cm⁻¹ C=O stretch
- 1485 cm⁻¹ CH₂ scissor
- 1250 cm⁻¹ CH₂ rock
- 1165 cm⁻¹ CH₂ wag

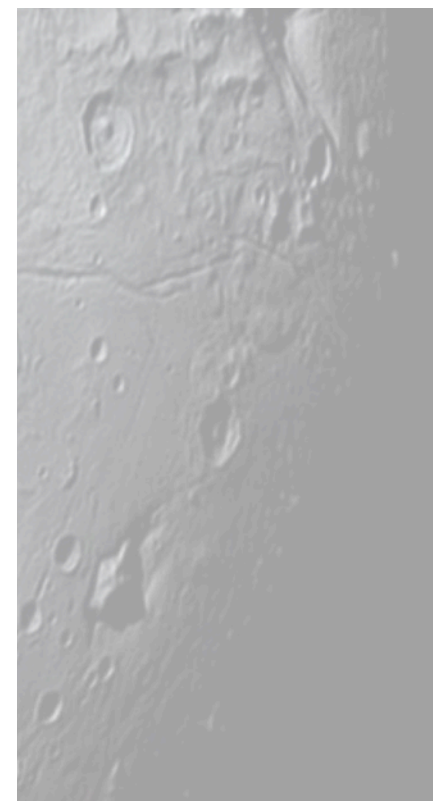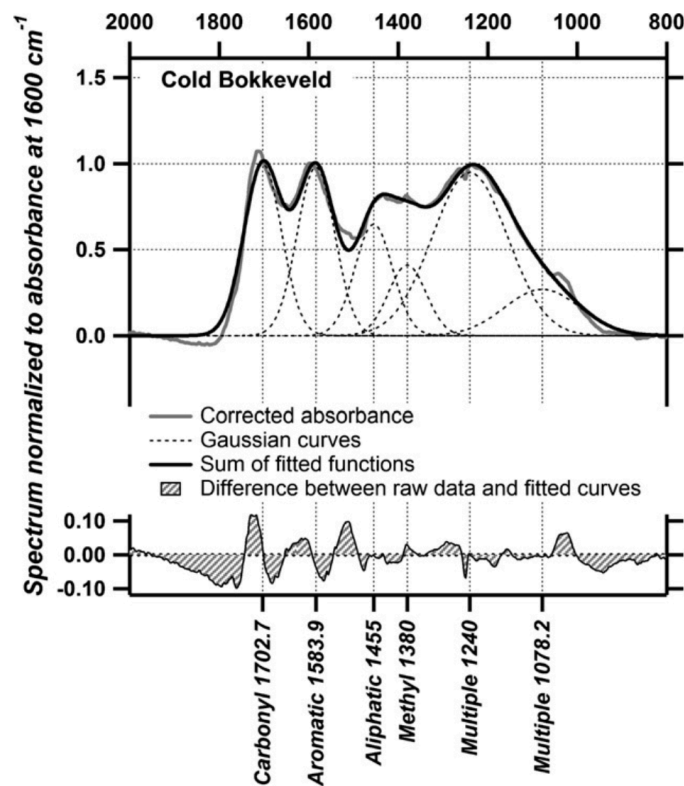Lower spectrum labels:
- Wavelength μ = 10⁻⁶ meter
- Note inverted peaks — Top: 100% transmission, Bottom: No transmission
- 19 atoms...
- vanillin (CCl₄ solution)
- Frequency cm⁻¹ = Hz/c
- OCH₃, OH
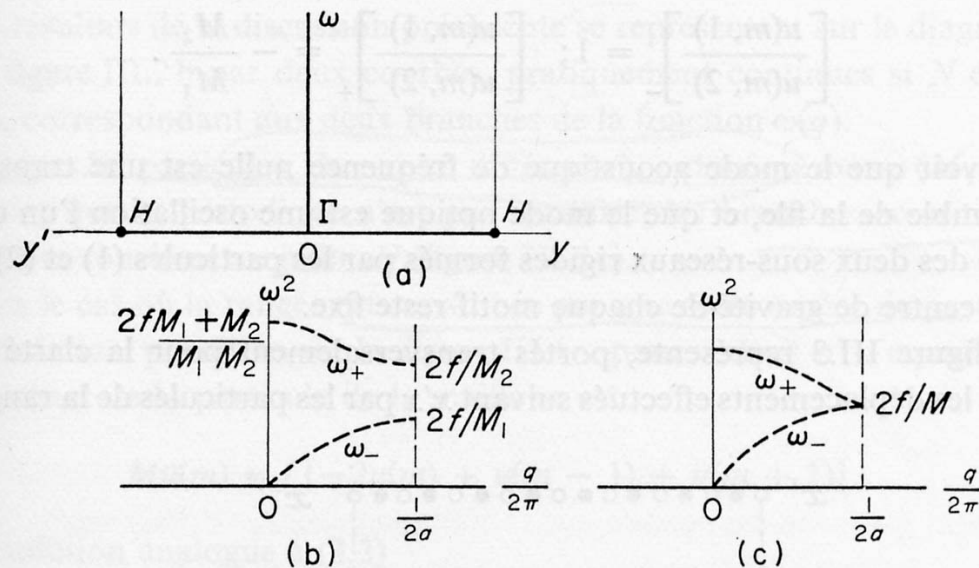
Chondritic kerogen
Orthous-Daunay et al. 2013
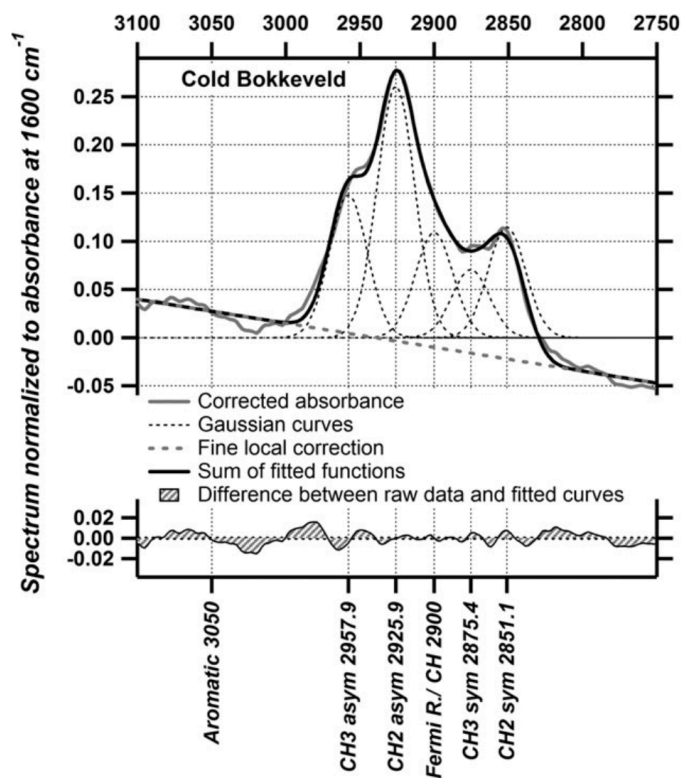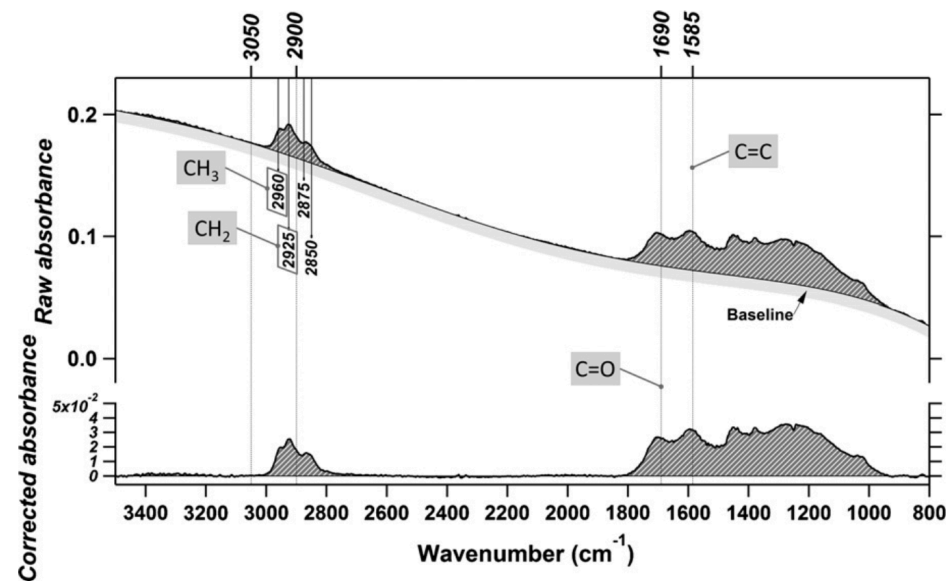
Vibrational modes in solids

Solid = Giant molecule of ~6 10^{23} atoms
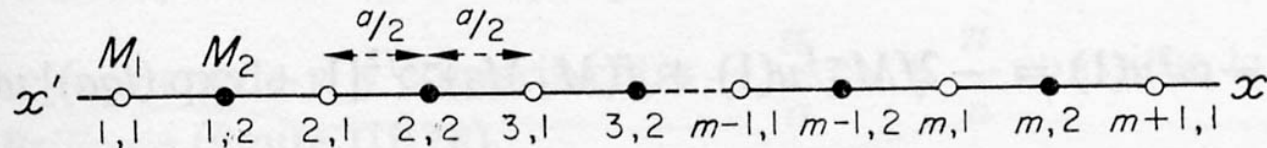
Fig. III.2 Vibrations du réseau de la figure III.1 :
a) zone de Brillouin; b) branches optique et acoustique; c) cas où
$M_1 = M_2 = M$.

$$q = 2\pi \frac{n}{Na}$$

$$\exp(-iqNa) = 1$$

$$u_{2n} = A\exp(-\omega(q)t - q.2n.a)$$

$$\omega_{\pm}^{2} = f(M_1 M_2)^{-1}\left[(M_1 + M_2) \pm \sqrt{M_1^2 + M_2^2 + 2M_1 M_2 \cos qa}\right]$$

Tableau XI.4

Molécule:	HCl	HCN	CO_2	NH_3	$HgCl_2$	C_6H_6
Vapeur:	2886	2089	2349	3336	355	993
Cristal:	2725	2097	2344	3223	314	990
	161	-8	+5	113	41	3
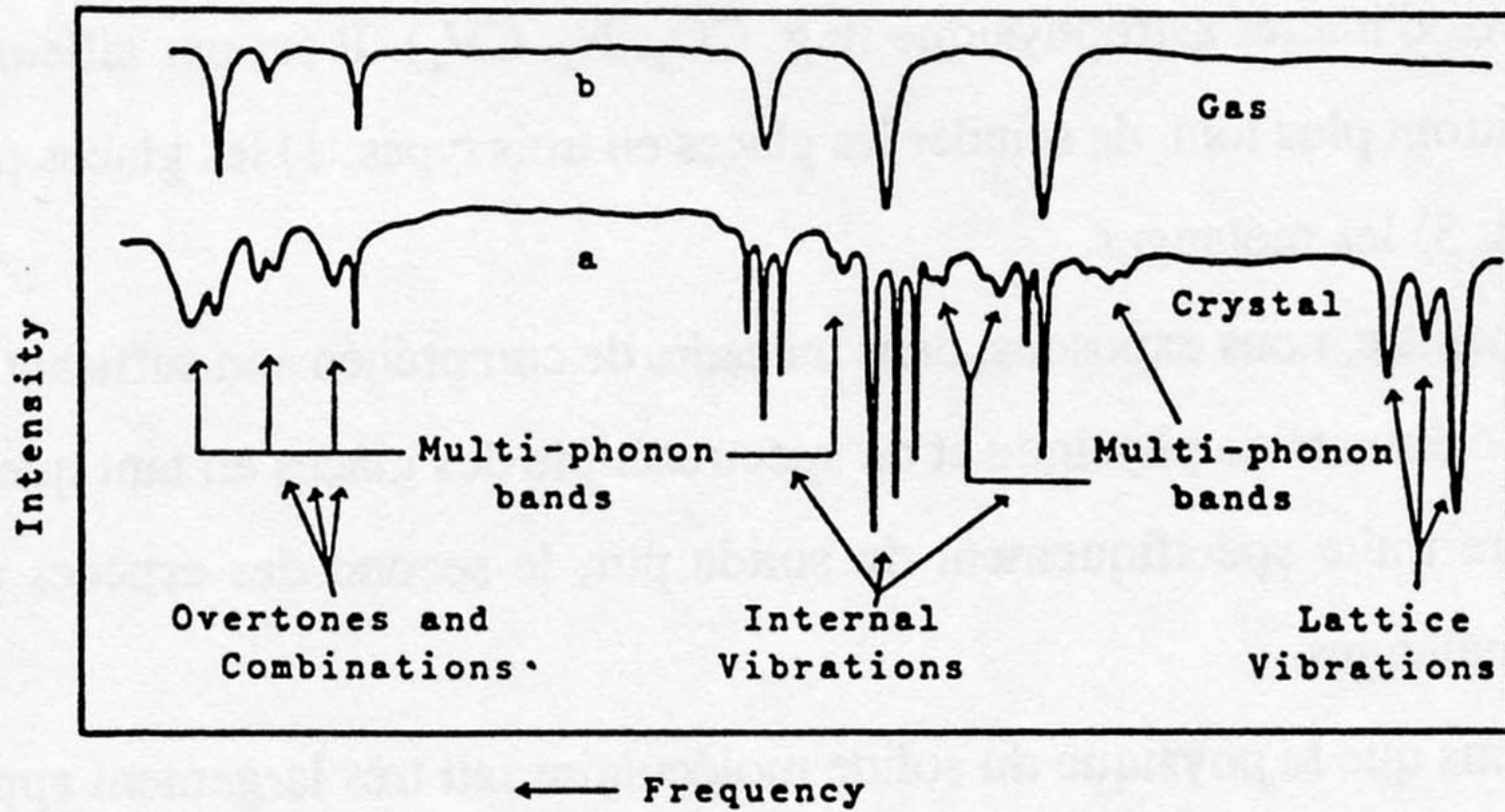
Vibration propagation : vibron

Translation : phonon

Hindered rotation : libration

internal vibrations $[(3N-6)\sigma]$

lattice vibrations $(6\sigma - 3)$

optical branches $(3\sigma N - 3)$

acoustical branches (3)
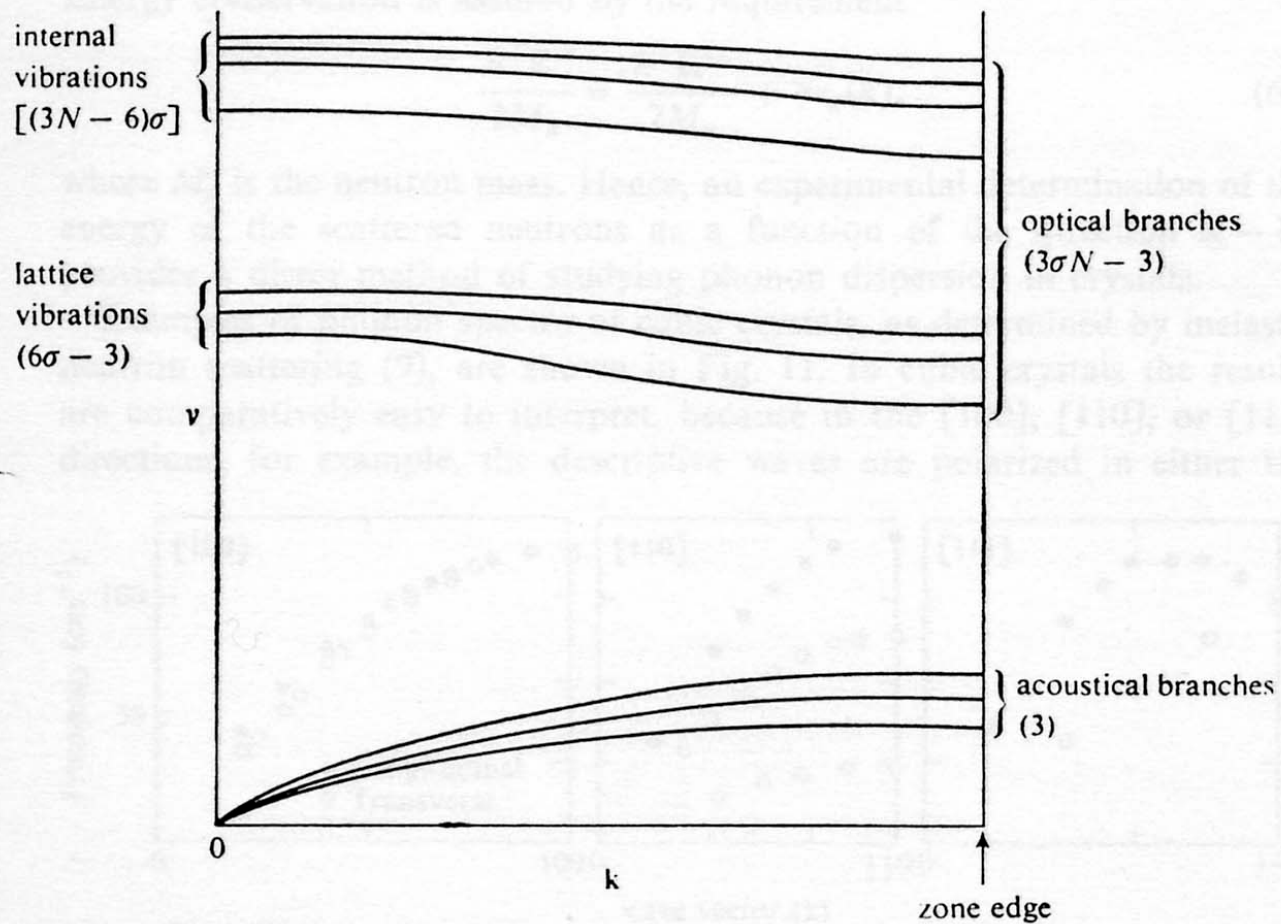
v

0

k

zone edge

FIG. 10. General form of dispersion curves for a molecular crystal.
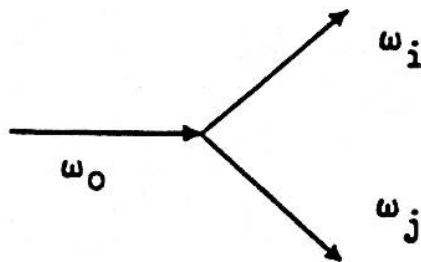
Photon-phonon coupling

Momentum conservation
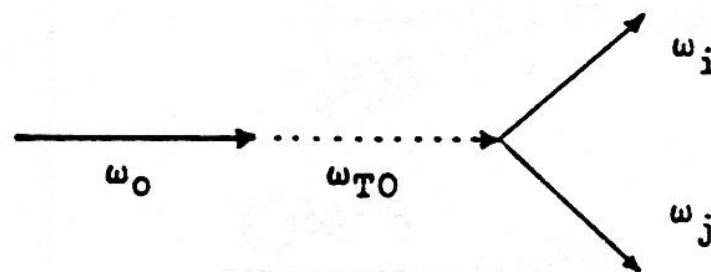
Overtones and combinations modes reflect VDOS

$$\vec{k} = \vec{q} = \frac{2\pi}{\lambda}\vec{n} \sim 0$$

$$\nu(\vec{k} = \vec{0})$$

$$\nu_i(\vec{k}) + \nu_j(-\vec{k})$$

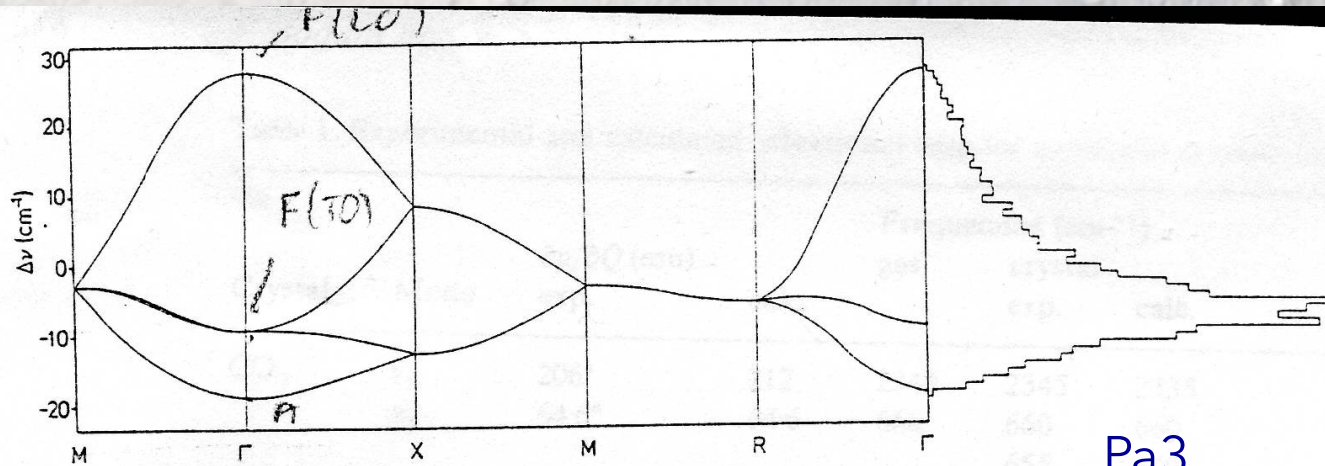a) direct mechanism   b) indirect mechanism

CO$_2$: dispersion curves and VDOS
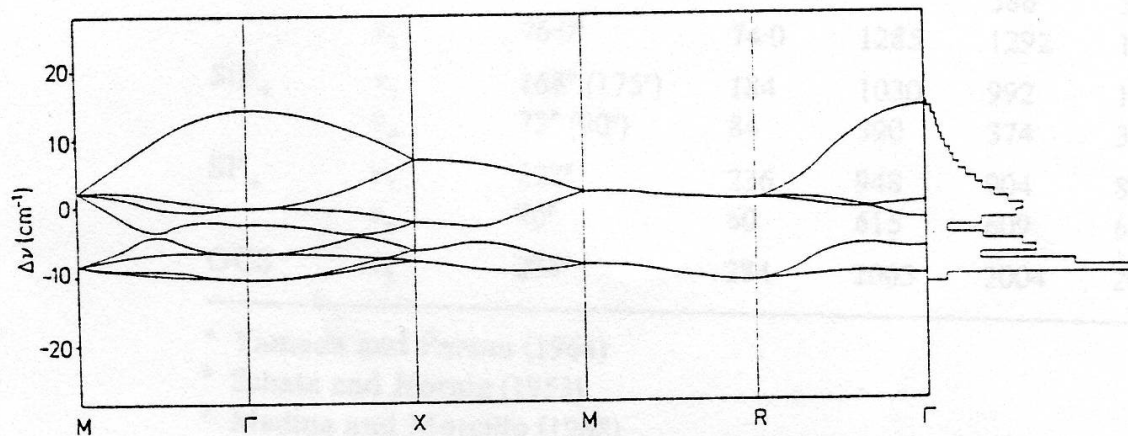
ν_3

ν_2

Pa3

Figure 1. Dispersion curves and densities of states for the antisymmetric (upper curve) and bending (lower curve) modes in crystalline CO$_2$.
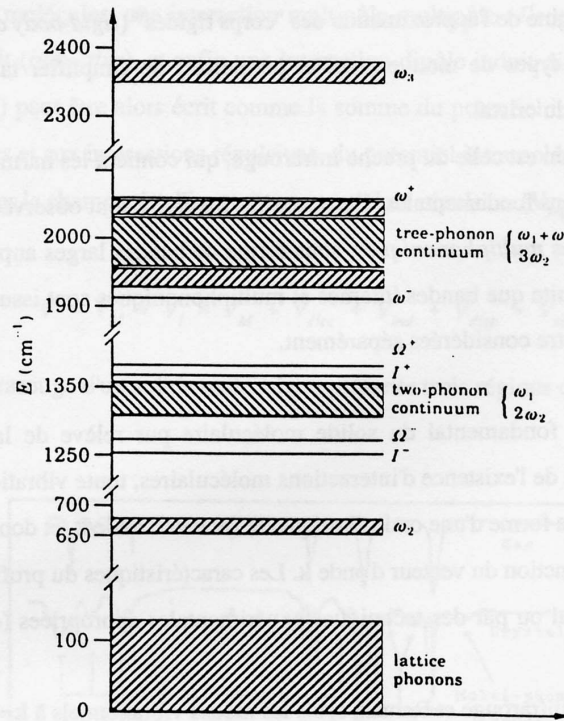
Figure III.2: *Le diagramme des niveaux d'énergie du cristal de CO_2, montrant les modes externes et fondamentaux internes avec leurs dispersions respectives par rapport au vecteur d'onde. Les termes Ω^+, Ω^-, I^+, I^-, ω^+ et ω^- ont trait à des **bound states** (voir § III.1.5). D'après Foggi et Schettino (1992).*

Static and dynamic effects

- STATIC=Symmetry of the molecule in the crystal is lower than in gas

- DYNAMIC=Phase and out-of-phase interactions of neighbouring vibrators
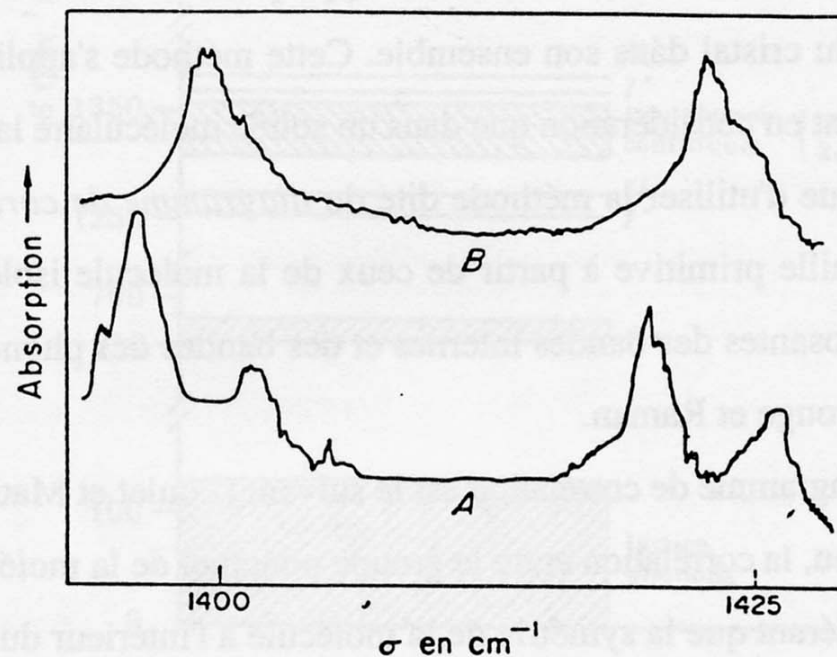
Figure III.3: *Illustration des effets dits **statique** et **dynamique**. A) la bande v_5 d'un cristal de CH_3I; B) la même bande pour des molécules de CH_3I diluées à 10 % dans un cristal de CD_3I (d'après Poulet et Mathieu 1970).*

Fundamental modes SO$_2$

Splitting LO-TO

	Molecule	Site	Factor group
ν_1, ν_2, z xx, yy, zz	C_{2v} A_1	C_2 A_1	C_{2v} A_1 $\left\{ \begin{array}{l} c, aa \\ bb, cc \end{array} \right.$
		A	
xy	A_2	A_2	a, b
ν_3, x, xz	B_1	B_1	a, ac
		B	
y, yz	B_2	B_2	b, bc

a) Within the molecule, the orthogonal axes x and z lie in the molecular plane with the latter coincident with the molecular C_2 axis, y is normal to both.

Tableau III.1: *Le diagramme de corrélation du cristal de SO$_2$.*
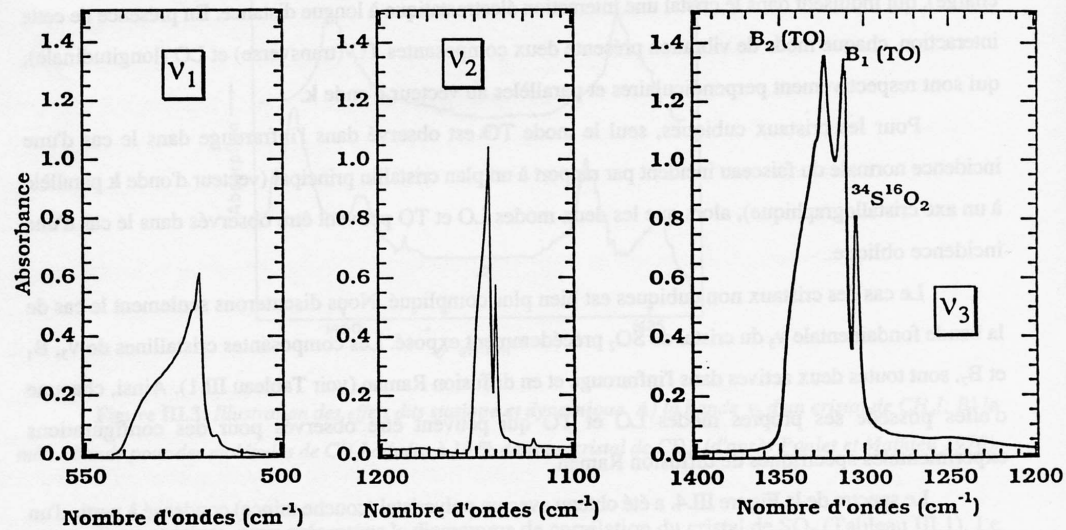

Figure III.4: *Les bandes fondamentales ν_1 (a), ν_2 (b) et ν_3 (c). Ces spectres ont été effectués avec un échantillon polycristallin (couche mince) à une température d'environ 112 K. Pour les 3 modes, la composante de droite est due à l'isotope $^{34}S^{16}O$. Le profil des bandes est dû au dédoublement LO-TO.*

Overtone and combination modes in solid SO$_2$

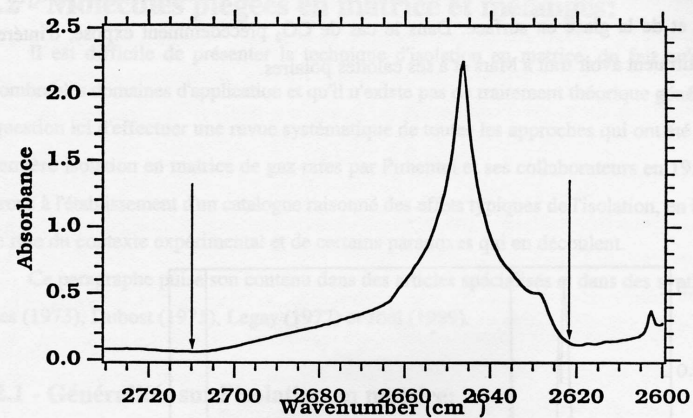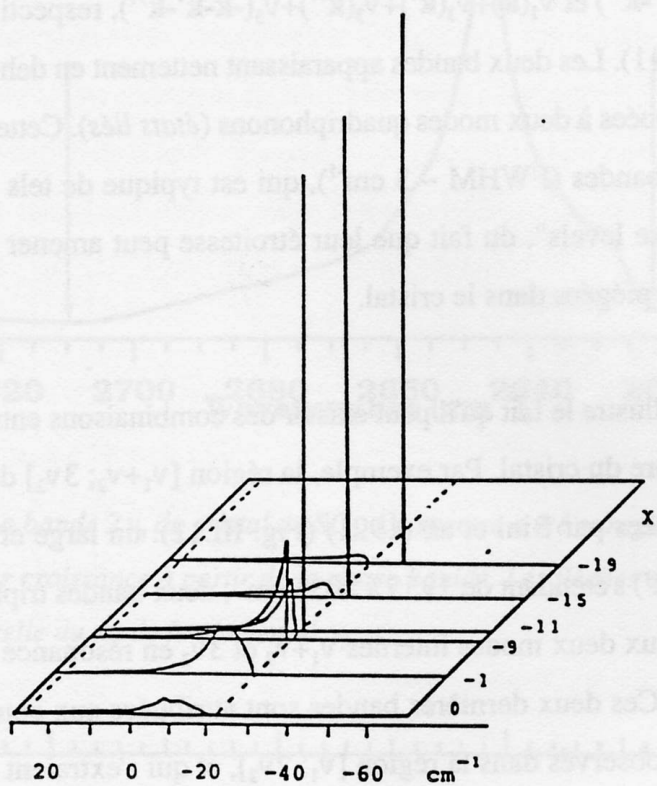
Figure III.10: *La bande 2 v_3 du cristal de SO$_2$. Ce spectre a été enregistré à partir d'un échantillon de 1 cm d'épaisseur obtenu par croissance à partir de la phase liquide. Les flèches délimitent la gamme de dispersion du mode 2 v_3 déduite de celle du mode fondamental v_3.*
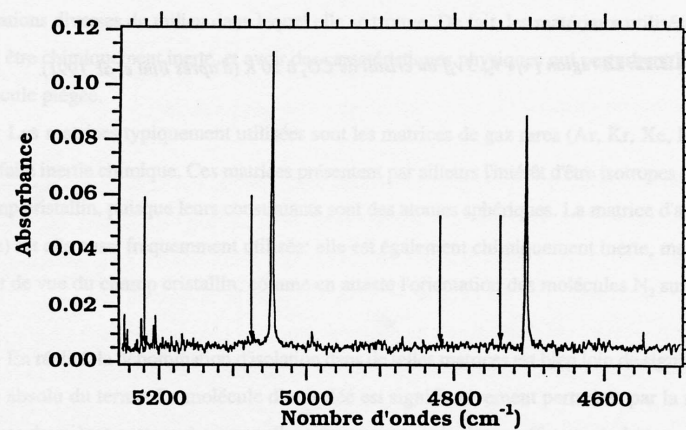

Figure III.11: *Les bandes v_1+3 v_3 et 3 v_1+ v_3 d'un cristal de SO$_2$. Ce spectre a été enregistré à partir d'un échantillon de 1 cm d'épaisseur obtenu par croissance à partir de la phase liquide. Les flèches délimitent la gamme de dispersion des modes v_1+3 v_3 et 3 v_1+ v_3 déduites de celles des modes fondamentaux v_1 et v_3. Le continuum à quatre phonons n'est pas observé ici, du fait de sa très faible intensité.*

Crystalline CO$_2$

$\Omega^+ \approx 1384.4$

$\Omega^- \approx 1276.1$

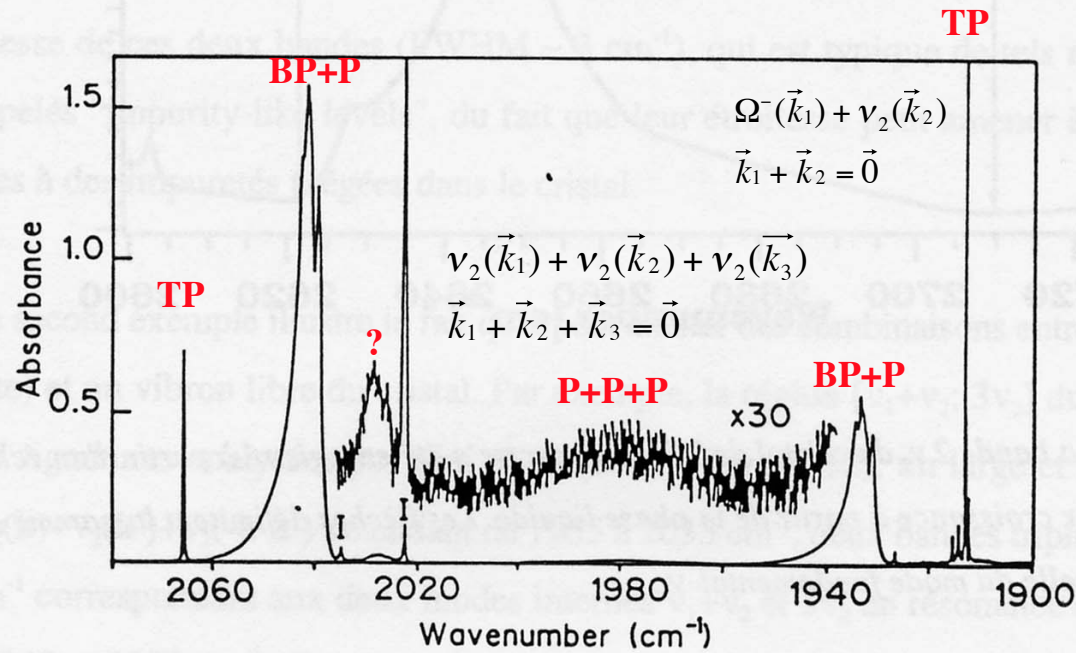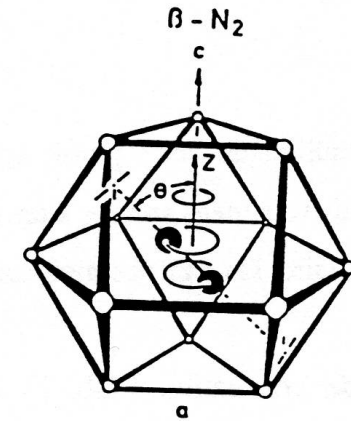$\Omega^+(\vec{k}_1) + \nu_2(\vec{k}_2)$

$\vec{k}_1 + \vec{k}_2 = \vec{0}$

TP

BP+P

$\Omega^-(\vec{k}_1) + \nu_2(\vec{k}_2)$

$\vec{k}_1 + \vec{k}_2 = \vec{0}$

TP

$\nu_2(\vec{k}_1) + \nu_2(\vec{k}_2) + \nu_2(\vec{k}_3)$
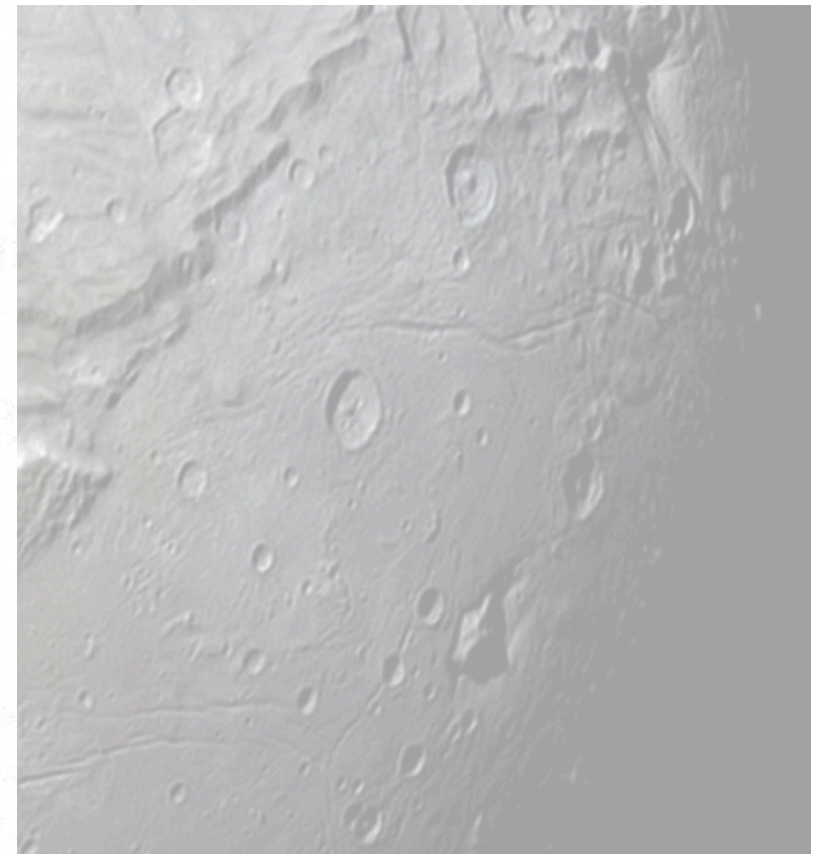
$\vec{k}_1 + \vec{k}_2 + \vec{k}_3 = \vec{0}$

?

P+P+P

BP+P

x30

Figure III.12: *La région [$\nu_1 + \nu_2$; 3 ν_2] du cristal de CO$_2$ à 20 K (d'après Bini et al. 1991).*
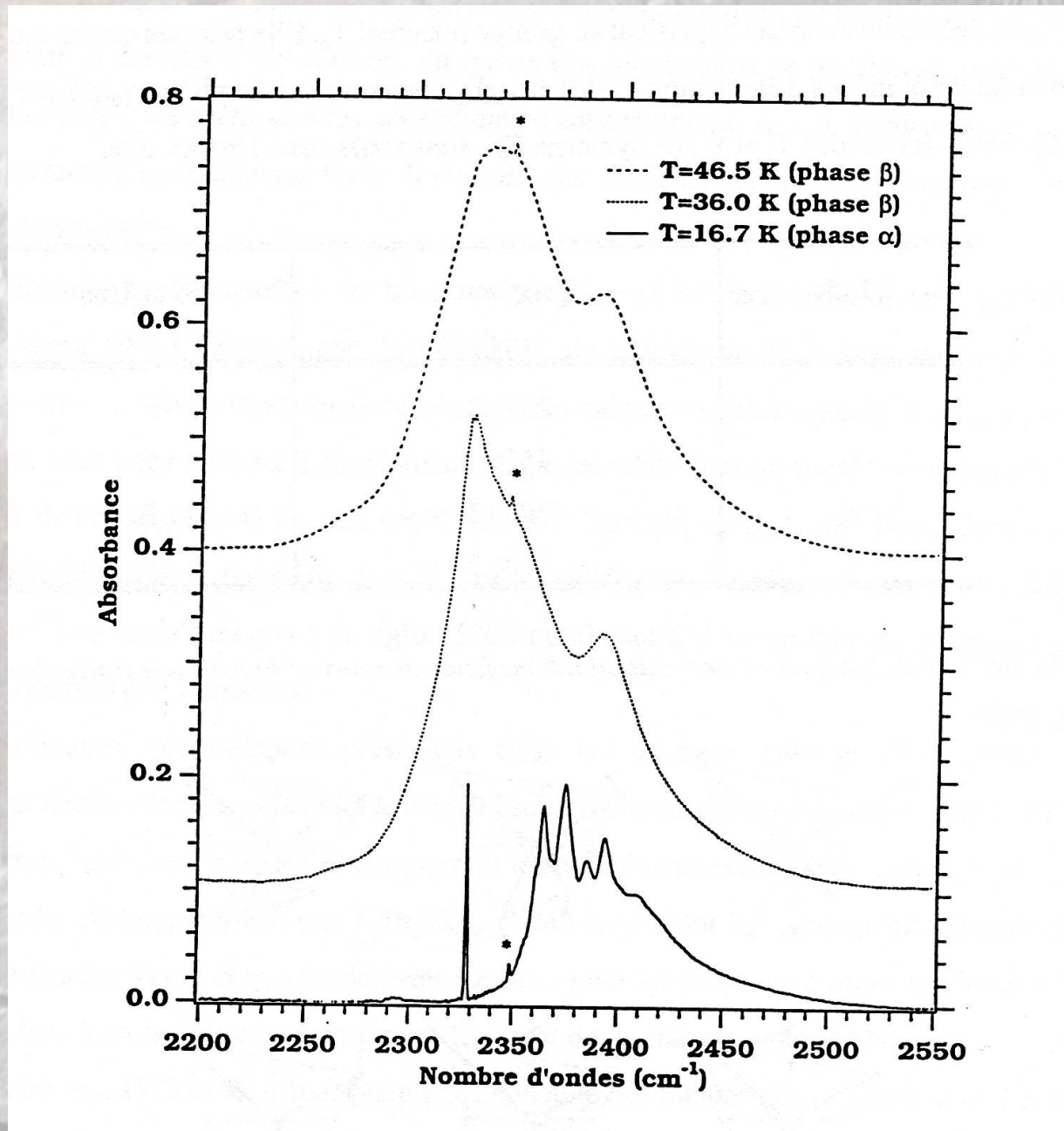
Solid nitrogen

α - N₂

β - N₂
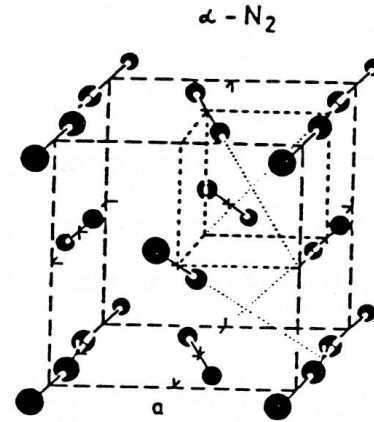
Mode	Molecular symmetry	Site symmetry	Factor group symmetry	Activity
	$D_{\infty h}$	S_6	T_h	
α-N₂				
ν_0	Σ_g^+	A_g	A_g	Raman
			E_g	Raman
R_x, R_y	Π_g	E_g	T_g	Raman
T_z	Σ_u^+	A_u	A_u	-
			E_u	-
T_x, T_y	Π_u	E_u	T_u	Infrared
	$D_{\infty h}$	D_{3h}	D_{6h}	
β-N₂				
ν_0	Σ_g^+	A_1'	A_{1g}	Raman
			B_{1u}	-
R_x, R_y	Π_g	E''	E_{1g}	Raman
			E_{2u}	Acoustic
T_z	Σ_u^+	A_2''	B_{2g}	-
			A_{2u}	Acoustic
T_x, T_y	Π_u	E'	E_{2g}	Raman
			E_{1u}	-

Quadripolar transitions in solid N2

Carbonates

Ionocovalent solids :
- vibrations of anions
- external modes of cations

Aragonite

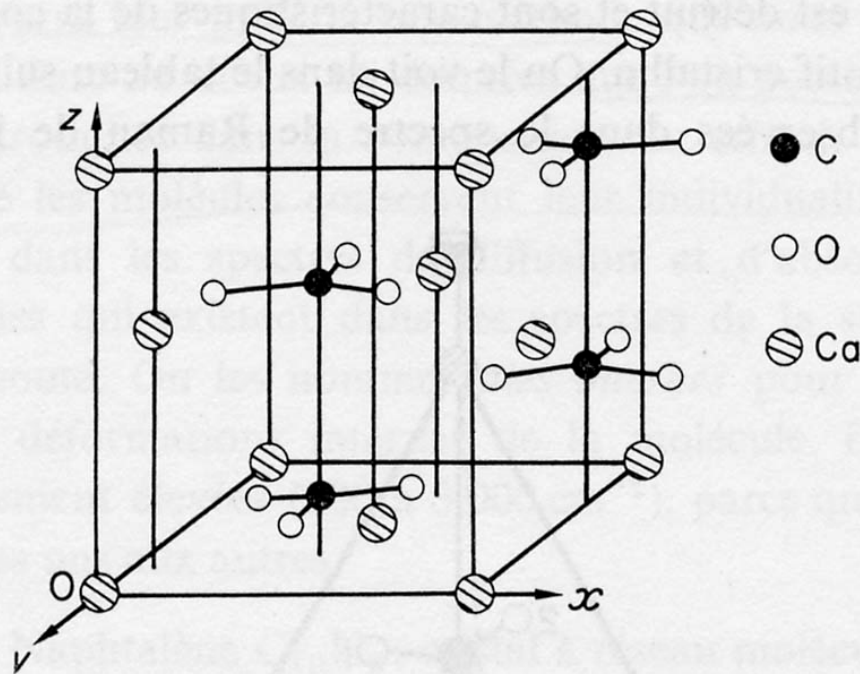Fig. V.2 Maille de l'aragonite $CaCO_3$.

4 formular units:
4 anions CO_3^{2-}
4 cations Ca_2^+
57 Vib/Lib + 3 T

σ_h

C_3

$C_2 \mid \sigma_v$

$\mathcal{D}_{3h}$
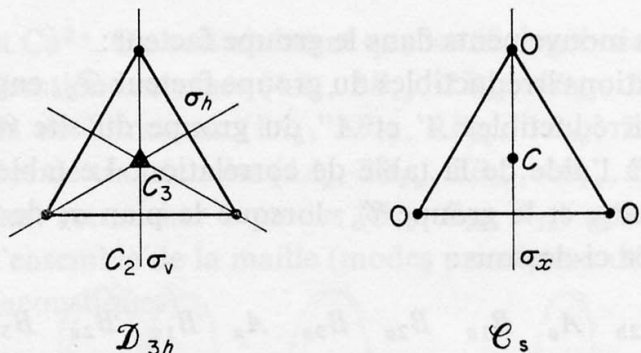
O

C

O ———— O

σ_x

$\mathcal{C}_s$

Fig. V.6 Symétrie de l'ion CO_3^{2-} libre et dans l'aragonite.

A_1' A_2'' E' E'

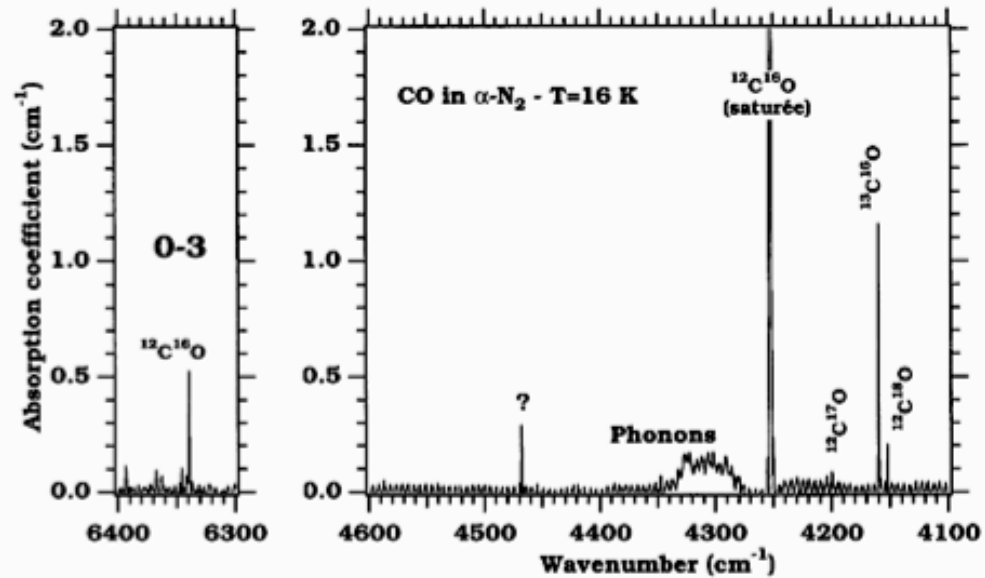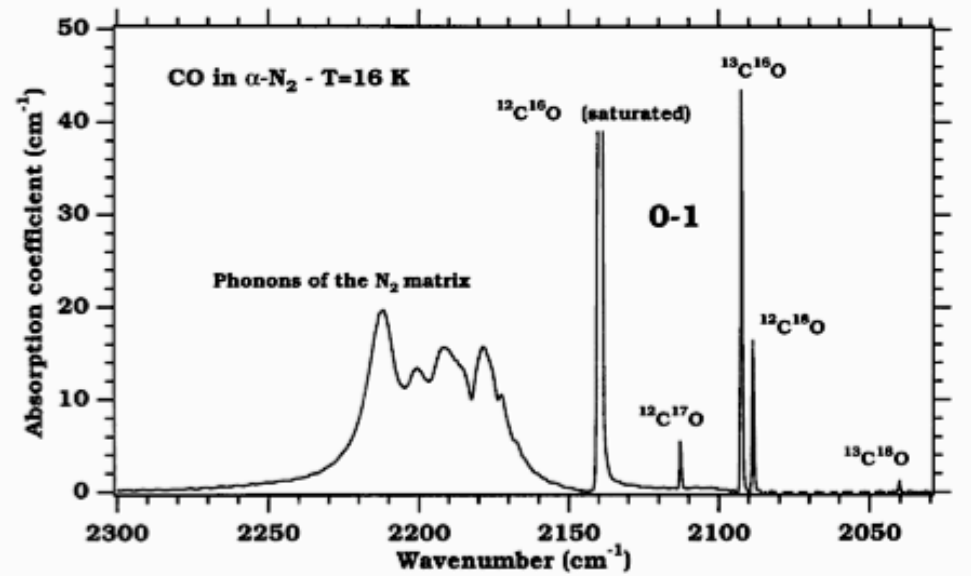$A_2''(T_z)$ $E'(T_x, T_y)$ $A_2'(R_z)$
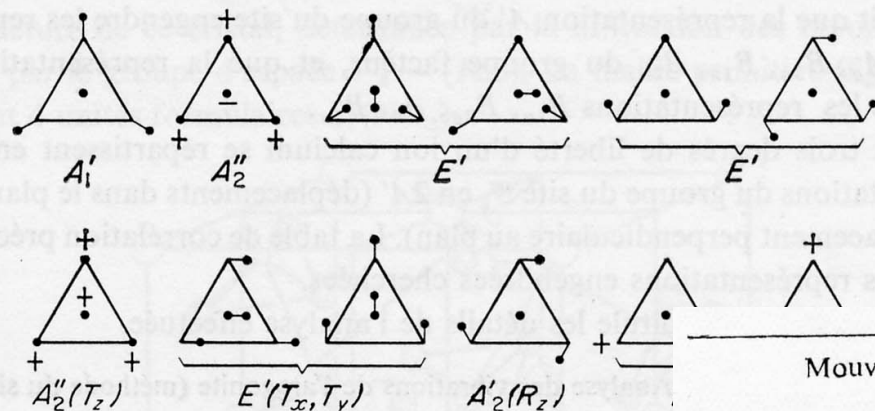
Fig. V.7 Vibrations de l'ion CO_3^{2-} lib[re]

| Mouvements d'un ion			$\mathcal{G}_M \to \mathcal{G}_S \to \mathcal{G}_F$		
Transl.	Libr.	Internes	D_{3h}	C_s	D_{2h}
CO_3^{--}		1	A_1'		A_g
					B_{1g}
			A_2'		B_{2g}
	1		A_2''	A'	B_{3g}
1					
		2	E'	A''	A_u
1					B_{1u}
			E''		B_{2u}
	1				B_{3u}
Ca^{++}					
2 (T_x, T_y)				A'	
1 T_z				A''	

Solid CO

| Mode vibrationnel	Fréquence (cm^{-1})	Attribution vibrationnelle principale (%)	Principal niveau perturbateur (%)
$3\nu_4$: $A_1+F_1+2F_2$	3870.49	$3\nu_4$ (83 %)	$\nu_1+\nu_4$ (15 %)
	3930.92	$3\nu_4$ (97 %)	$\nu_3+\nu_4$ (2 %)
$\nu_2+2\nu_4$: $A_1+A_2+2E+F_1+F_2$	4142.86	$\nu_2+2\nu_4$ (93 %)	$\nu_3+\nu_4$ (2 %)
$\nu_1+\nu_4$: F_2	4223.46	$\nu_1+\nu_4$ (83 %)	$3\nu_3$ (15 %)
$\nu_3+\nu_4$: F_2	4319.21	$\nu_3+\nu_4$ (92 %)	$3\nu_3$ (3 %)
$2\nu_2+\nu_4$: F_1+2F_2	4348.77	$2\nu_2+\nu_4$ (85 %)	$\nu_3+\nu_4$ (12 %)
	4379.10	$2\nu_2+\nu_4$ (100 %)	$3\nu_3$ (0 %)
$\nu_2+\nu_3$: F_1+F_2	4543.76	$\nu_3+\nu_4$ (85 %)	$2\nu_2+\nu_4$ (14 %)
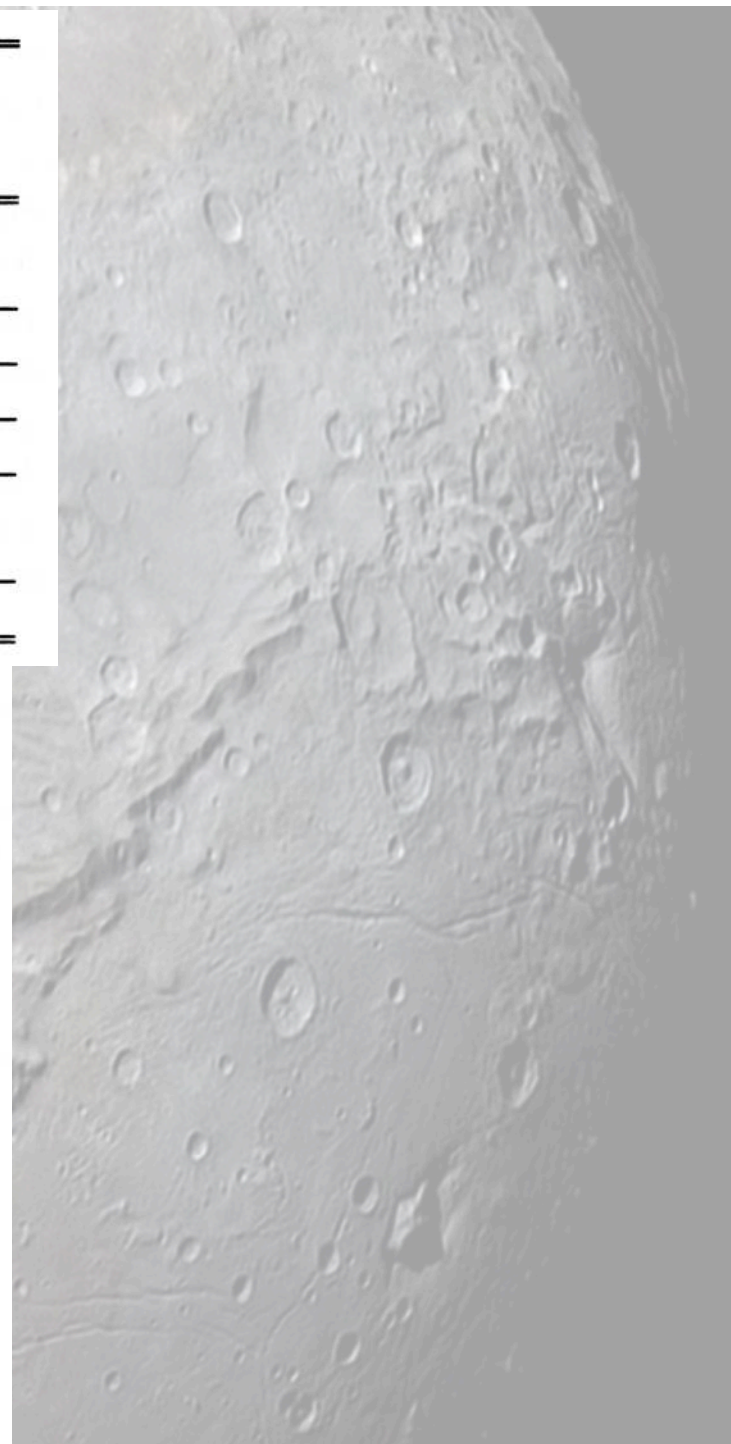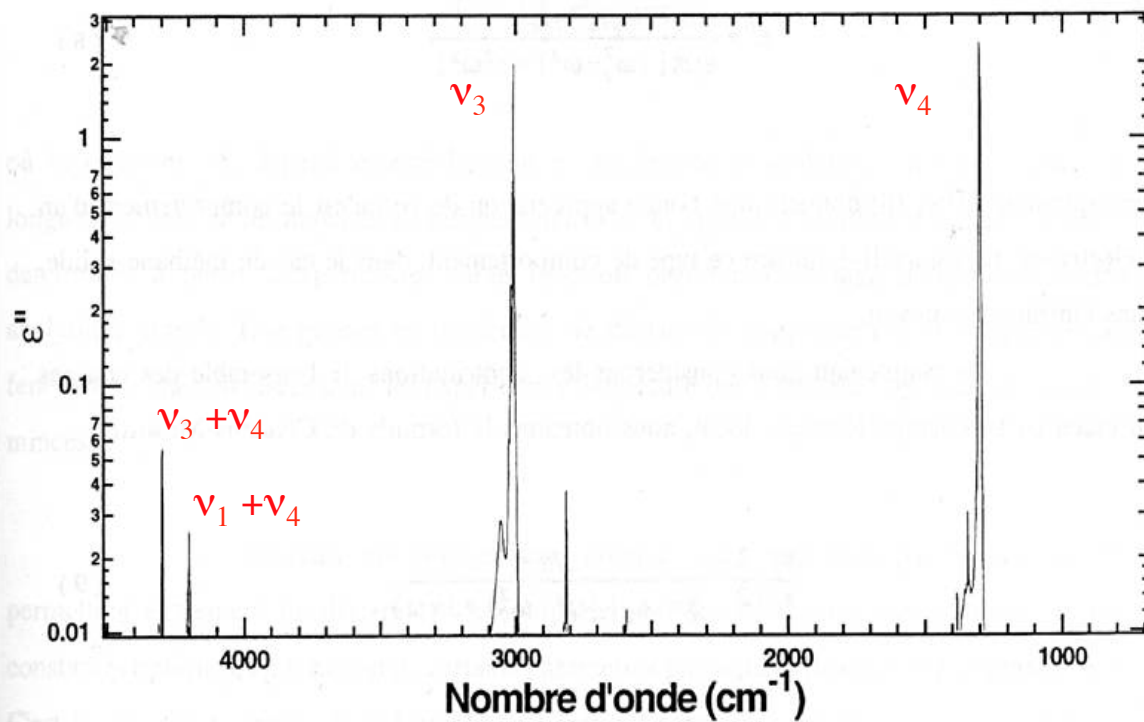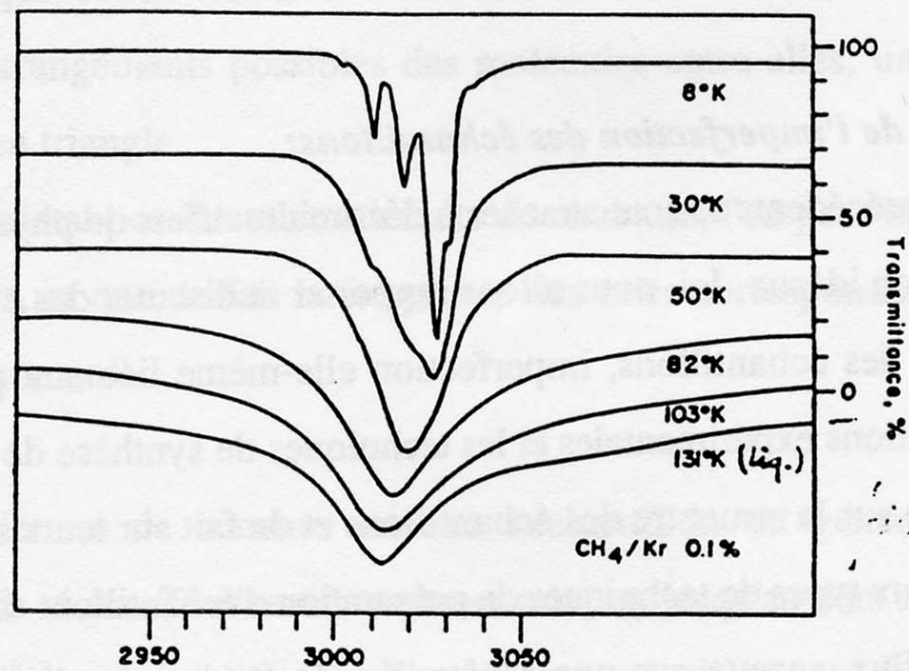
Figure III.19: *Effet de la température sur le structure fine de la bande v₃ de CH₄ piégée en matrice de Krypton (d'après Chamberland et al. 1973).*
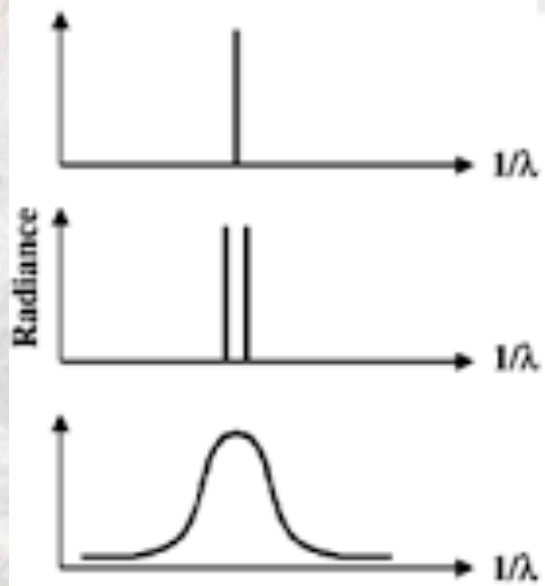
Part II - Instrumentation and practical issues

FTIR spectroscopy
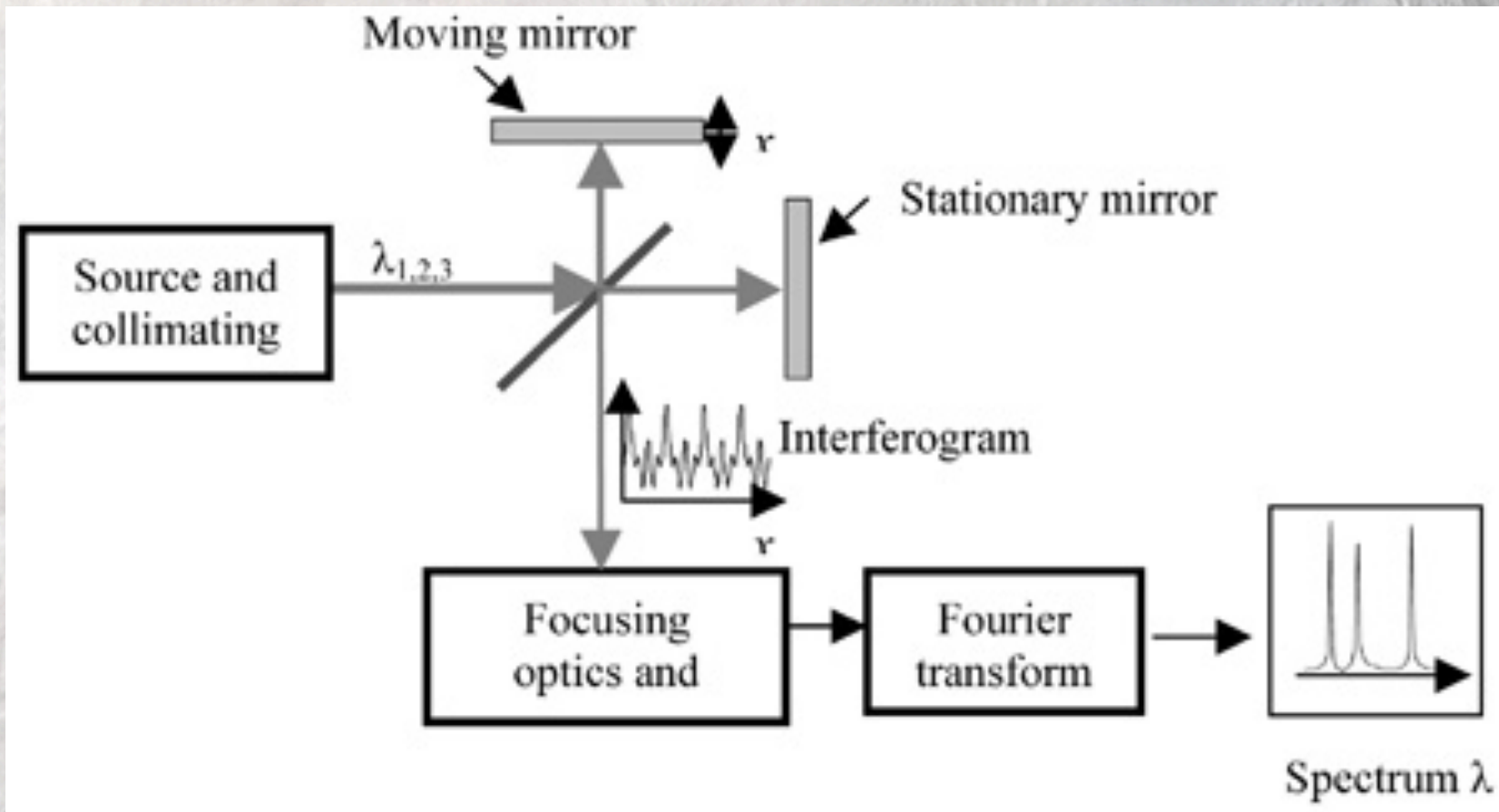
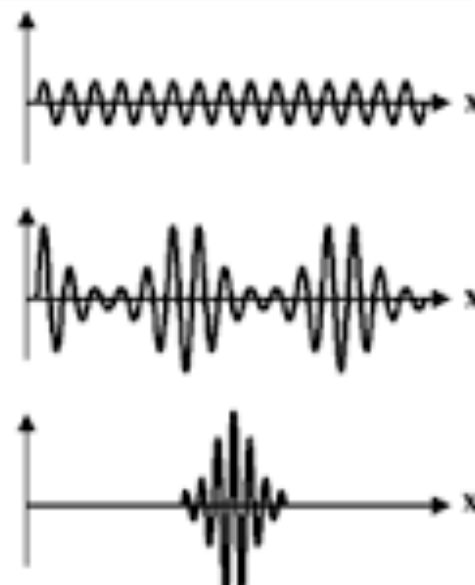

$$\tilde{I}(\delta) = \int_0^\infty I(\bar{\nu})cos^2(\pi\delta\bar{\nu})d\bar{\nu} = \frac{1}{2}\int_0^\infty I(\bar{\nu})(1 + cos(2\pi\delta\bar{\nu}))d\bar{\nu}$$
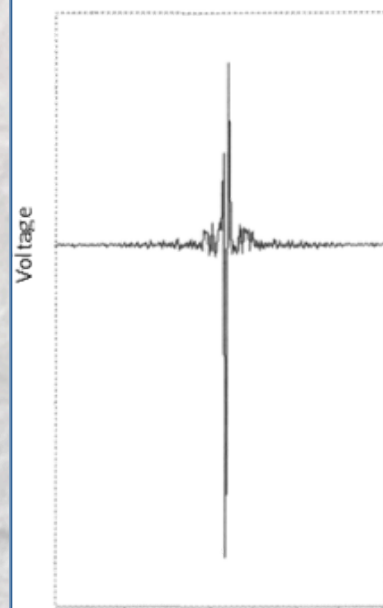
Spectral radiance distribution of incident radiation

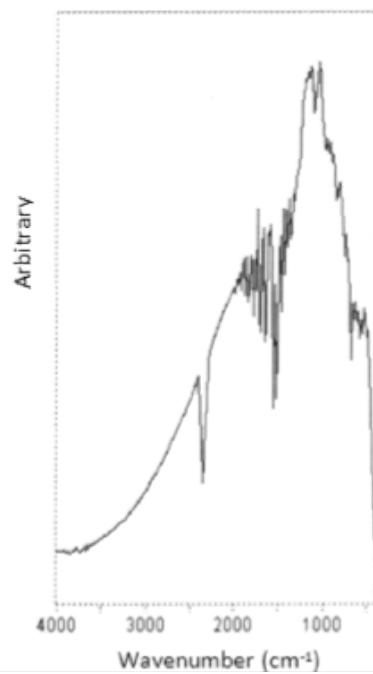Detector signal dependent on the optical path difference x within the interferogram
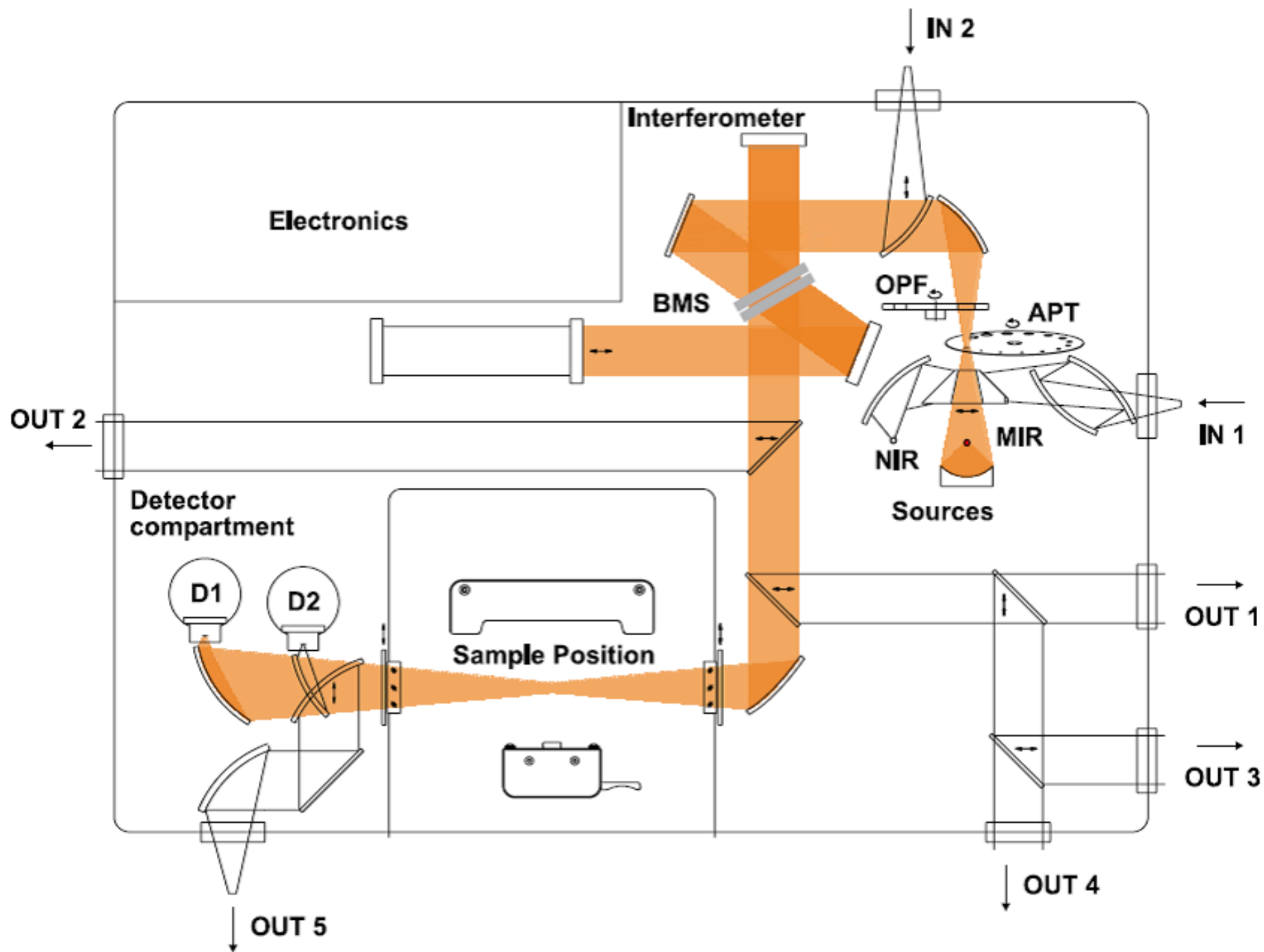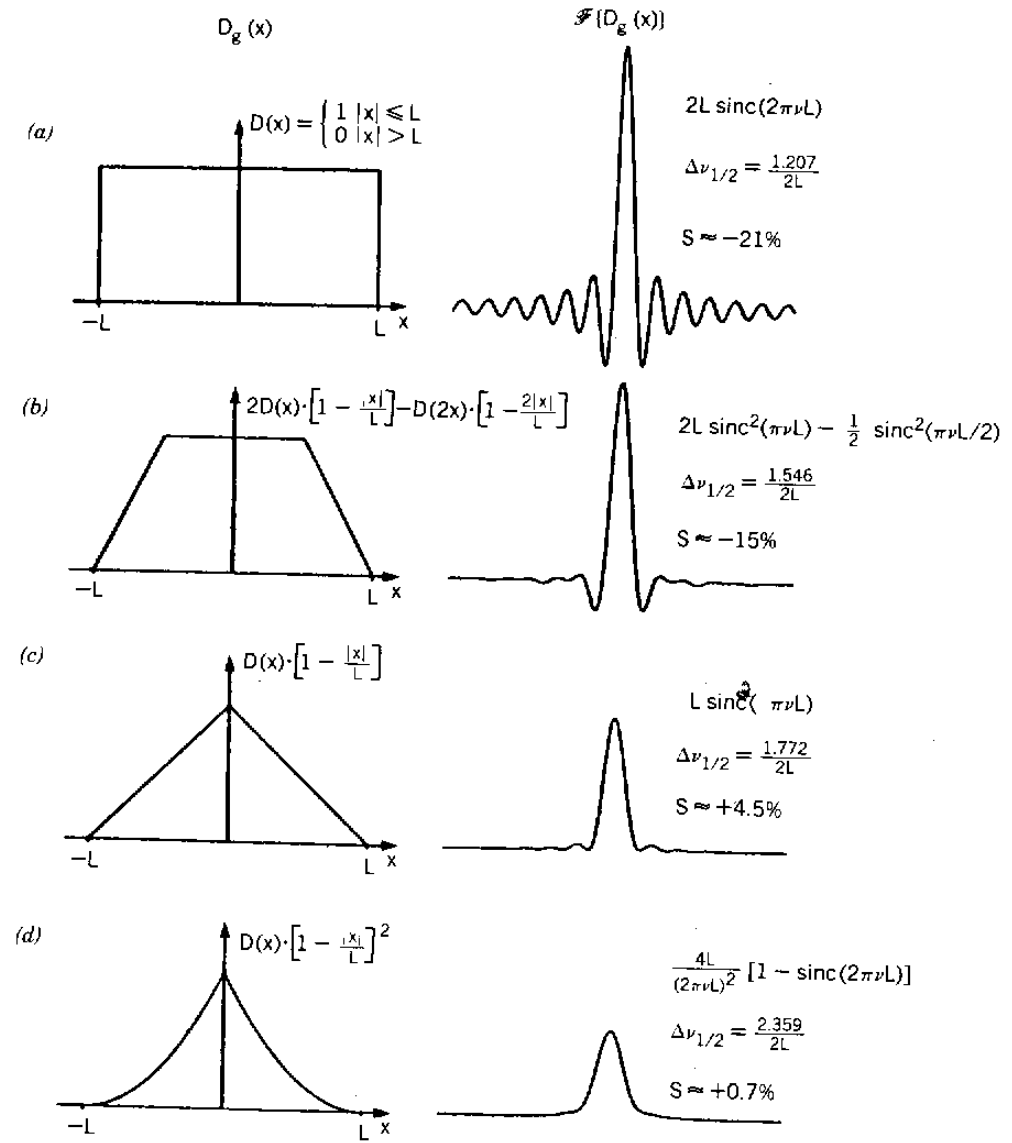
Interferogram → Fourier transform → Single beam spectrum

IN 2

Interferometer

Electronics

BMS

OPF

APT

OUT 2

NIR

MIR

IN 1

Sources

Detector compartment

D1

D2

Sample Position

OUT 1

OUT 3

OUT 4

OUT 5

$D_g(x)$ $\mathscr{F}\{D_g(x)\}$

(a) $D(x) = \begin{cases} 1 & |x| \leqslant L \\ 0 & |x| > L \end{cases}$ $2L\,\mathrm{sinc}(2\pi\nu L)$

$\Delta\nu_{1/2} = \dfrac{1.207}{2L}$

$S \approx -21\%$

(b) $2D(x)\cdot\left[1 - \frac{|x|}{L}\right] - D(2x)\cdot\left[1 - \frac{2|x|}{L}\right]$ $2L\,\mathrm{sinc}^2(\pi\nu L) - \frac{1}{2}\,\mathrm{sinc}^2(\pi\nu L/2)$

$\Delta\nu_{1/2} = \dfrac{1.546}{2L}$

$S \approx -15\%$

(c) $D(x)\cdot\left[1 - \frac{|x|}{L}\right]$ $L\,\mathrm{sinc}^2(\pi\nu L)$

$\Delta\nu_{1/2} = \dfrac{1.772}{2L}$

$S \approx +4.5\%$

(d) $D(x)\cdot\left[1 - \frac{|x|}{L}\right]^2$ $\dfrac{4L}{(2\pi\nu L)^2}\,[1 - \mathrm{sinc}(2\pi\nu L)]$

$\Delta\nu_{1/2} = \dfrac{2.359}{2L}$

$S \approx +0.7\%$

Fig. 1.8 Series of apodization functions and their corresponding instrument line shape functions; in each case the equations representing the shapes of the apodization and ILS functions are given, together with the full width at half-height, $\Delta\nu_{1/2}$, and the amplitude of the largest side lobe, S, as a percentage of the maximum excursion. (a) Boxcar truncation; (b) trapezoidal; (c) triangular; (d) triangular squared; (e) Bessel; (f) cosine; (g) sinc²; (h) Gaussian apodization. (Reproduced from [5], by permission of the Optical Society of America; copyright © 1981.)

Mono and FPA detectors for fast imaging
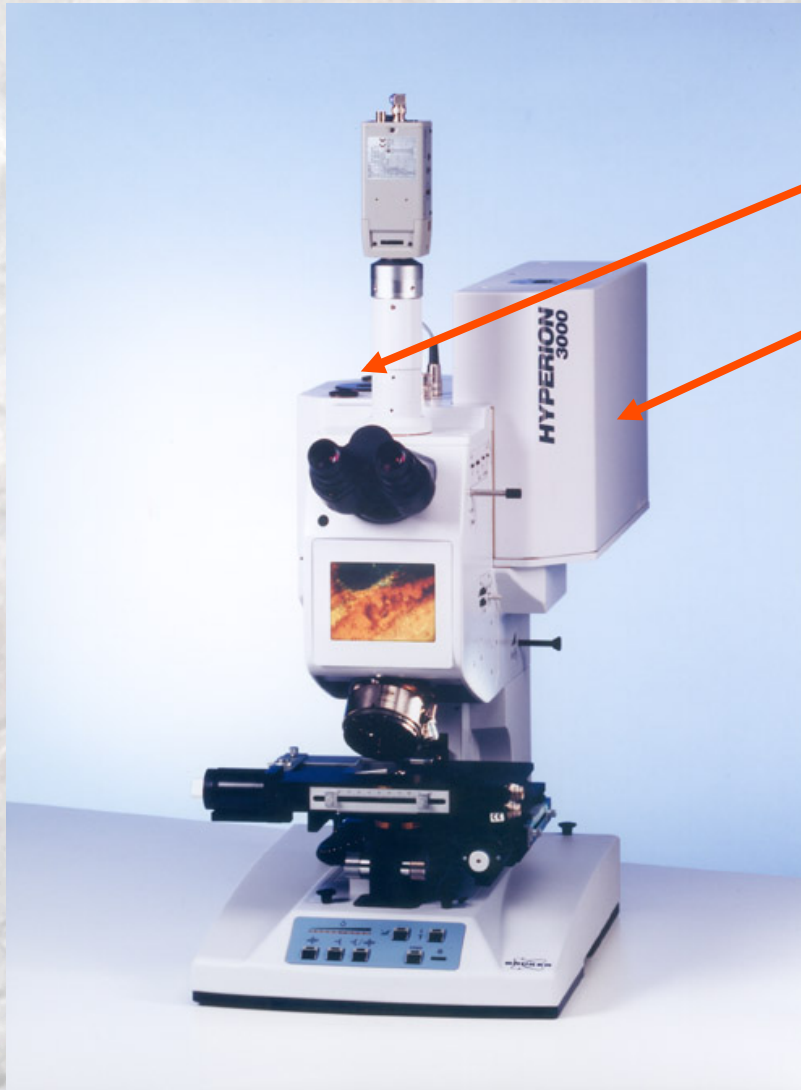
Focal Plane Array (FPA)-Detector

There are two separate optics within the microscope to optimize the homogeneity of the infrared and the visual light
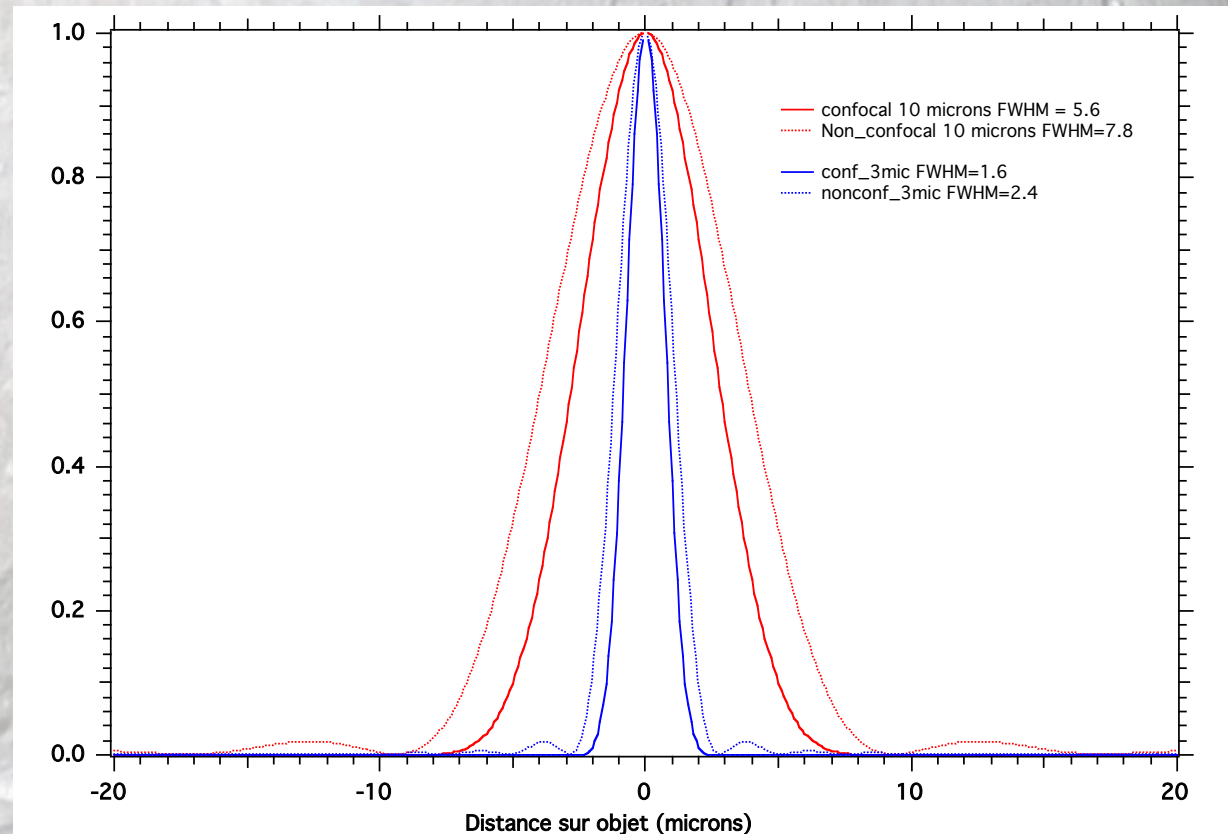
The size of the FPA-Detector element is 2.56 x 256mm
Using the 15x objective total measurement area corresponds to 2.56mm\15=177μm

The size of each pixel is 177μm\64 (number of pixels) =2.6μm (depending on the wavelenght)

HYPERION 3000
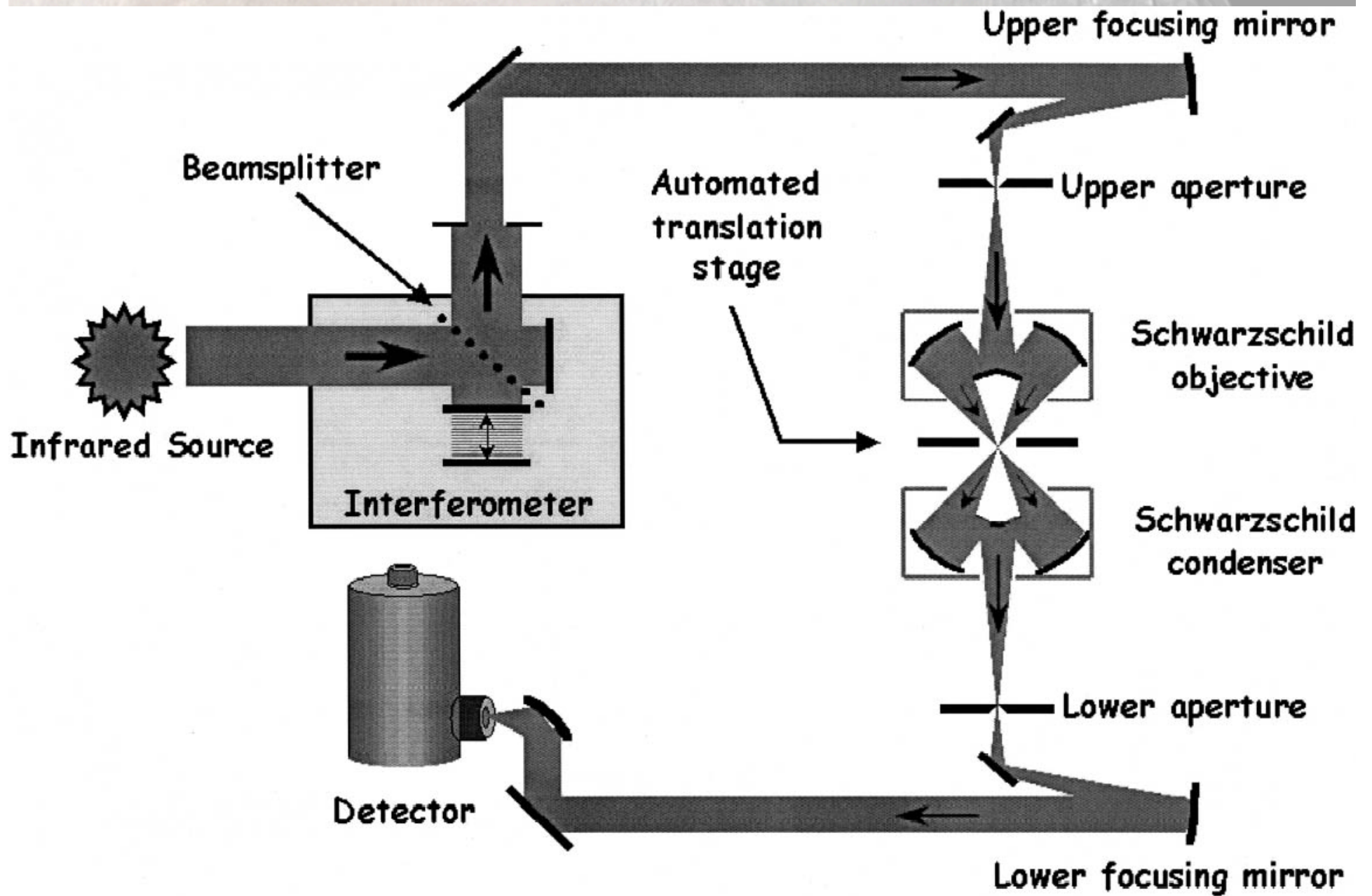
Improve spatial resolution and signal-to-noise ratio

+ source luminance (CsI Globar, synchrotron, tunable laser)
+ objective diffraction

confocal 10 microns FWHM = 5.6
Non_confocal 10 microns FWHM=7.8

conf_3mic FWHM=1.6
nonconf_3mic FWHM=2.4

Distance sur objet (microns)

Theoretical spatial resolution is almost never reached for complex heterogeneous natural samples
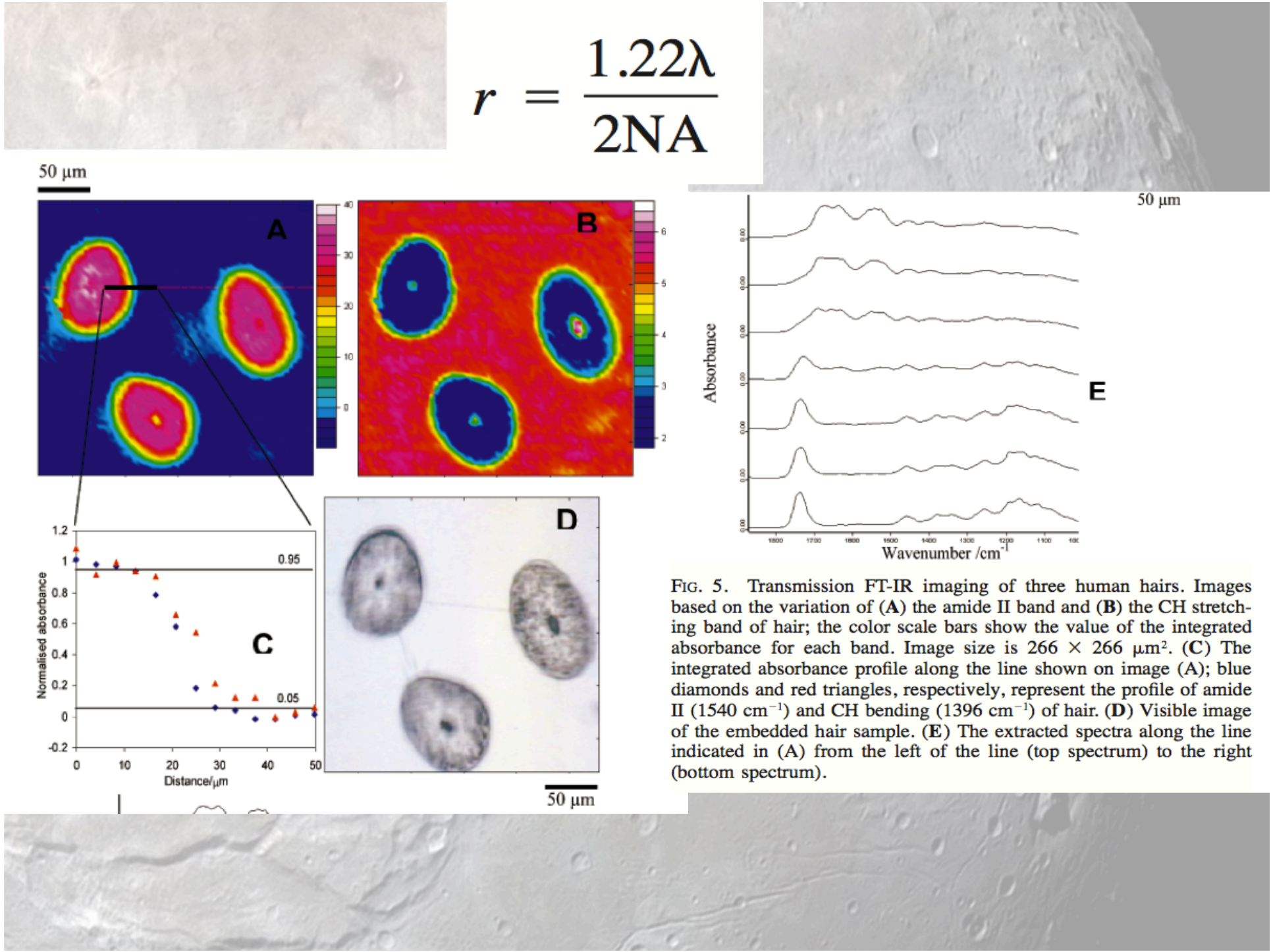
$$r = \frac{1.22\lambda}{2NA}$$

FIG. 5. Transmission FT-IR imaging of three human hairs. Images based on the variation of (**A**) the amide II band and (**B**) the CH stretching band of hair; the color scale bars show the value of the integrated absorbance for each band. Image size is 266×266 μm^2. (**C**) The integrated absorbance profile along the line shown on image (**A**); blue diamonds and red triangles, respectively, represent the profile of amide II (1540 cm^{-1}) and CH bending (1396 cm^{-1}) of hair. (**D**) Visible image of the embedded hair sample. (**E**) The extracted spectra along the line indicated in (**A**) from the left of the line (top spectrum) to the right (bottom spectrum).

ATR = Attenuated Total Reflectance spectroscopy
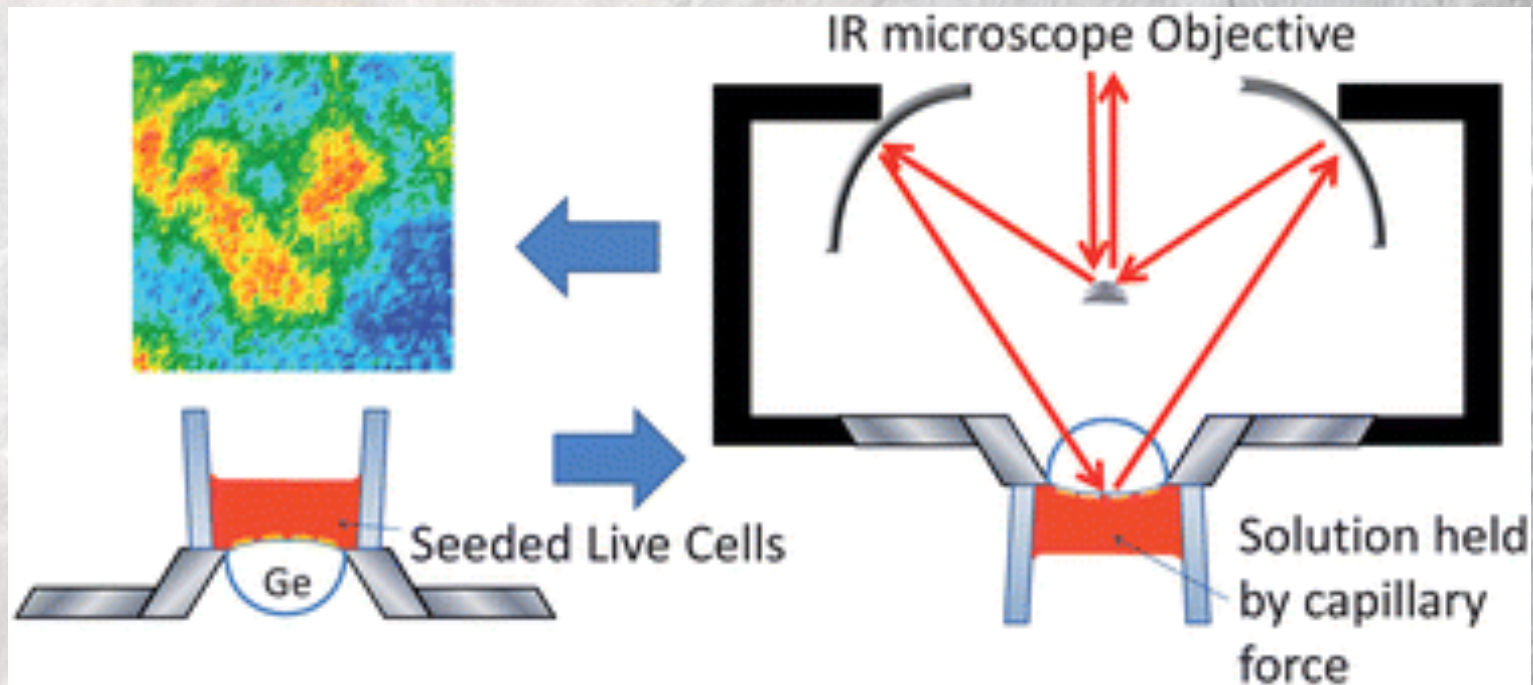
- Improve spatial resolution (factor 2-4)
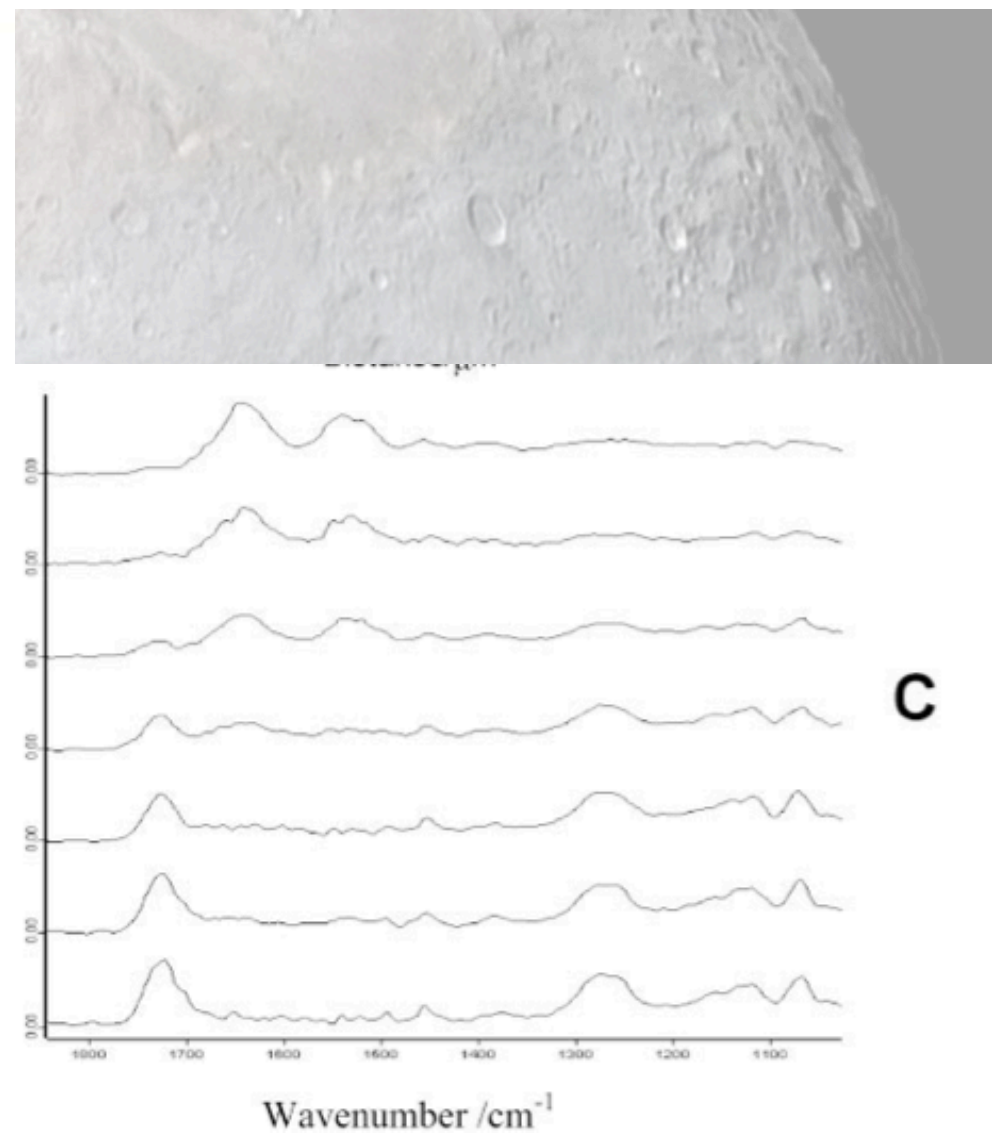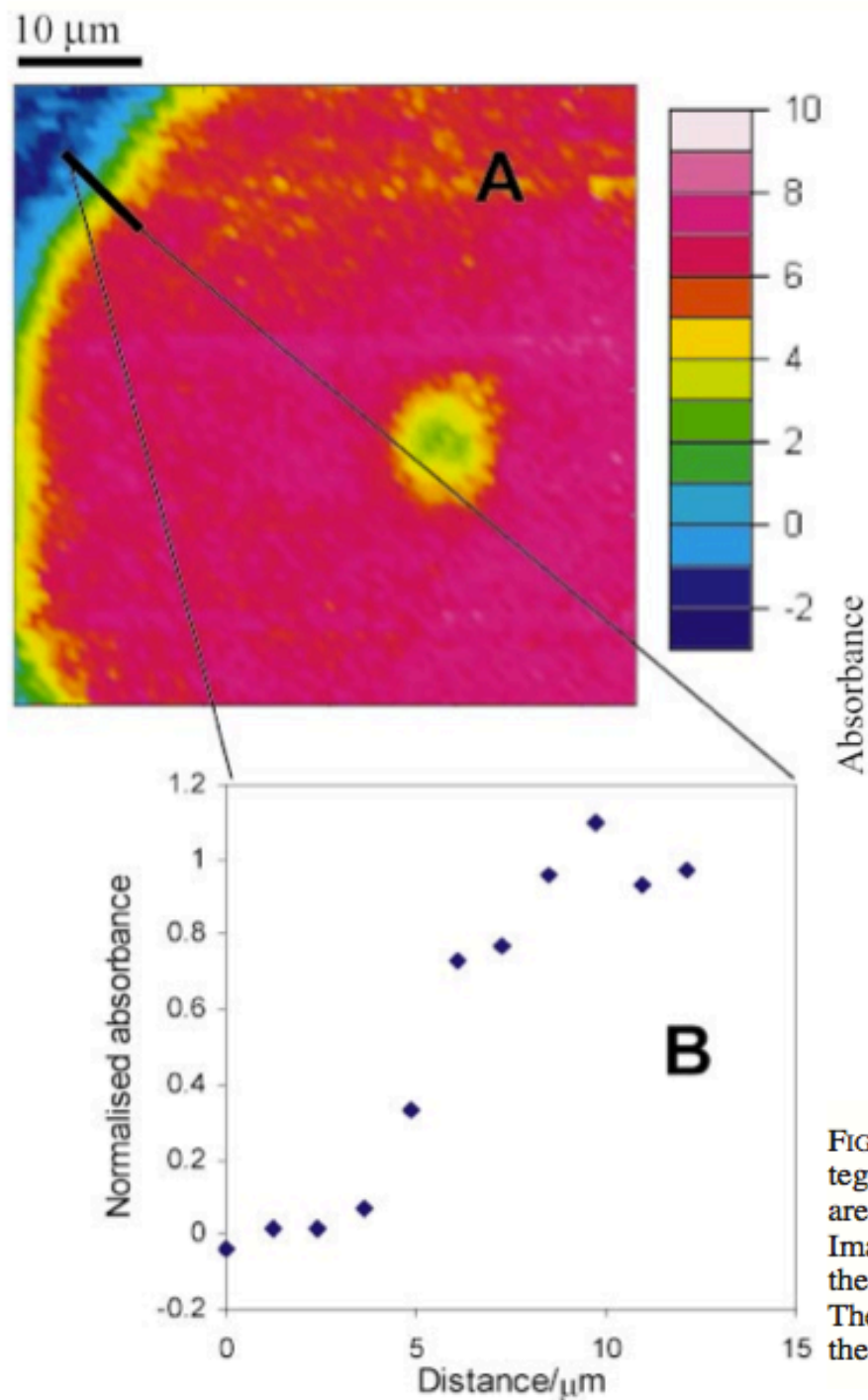- Spectra not strictly similar to transmission spectra

FIG. 2. (A) Chemical image of the hair generated by plotting the integrated absorbance of the amide I band at 1645 cm^{-1} over the imaged area; the color scale bar shows the value of the integrated absorbance. Image size is 50×50 μm^2. (B) The integrated absorbance profile of the amide II band at 1540 cm^{-1} along the line shown on the image. (C) The extracted spectra along the line indicated in (A) from the left of the line (bottom spectrum) to the right (top spectrum).

AFMIR = combined FTIR + AFM

- A new generation of instrument operating at ultra highspatial resolution (~40 nm)
- Real potential still to be tested
- Not easy to implement: developments in sample preparation
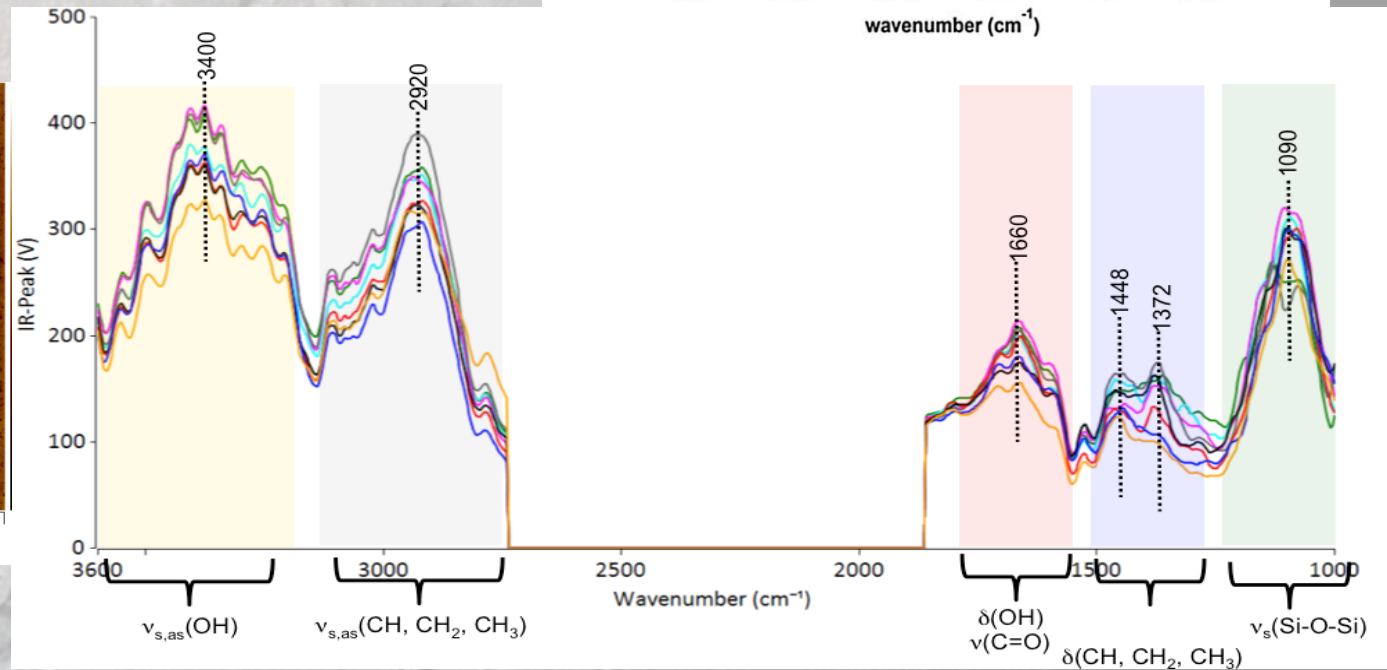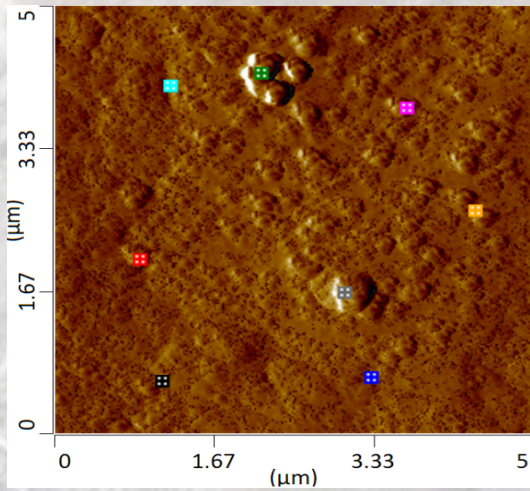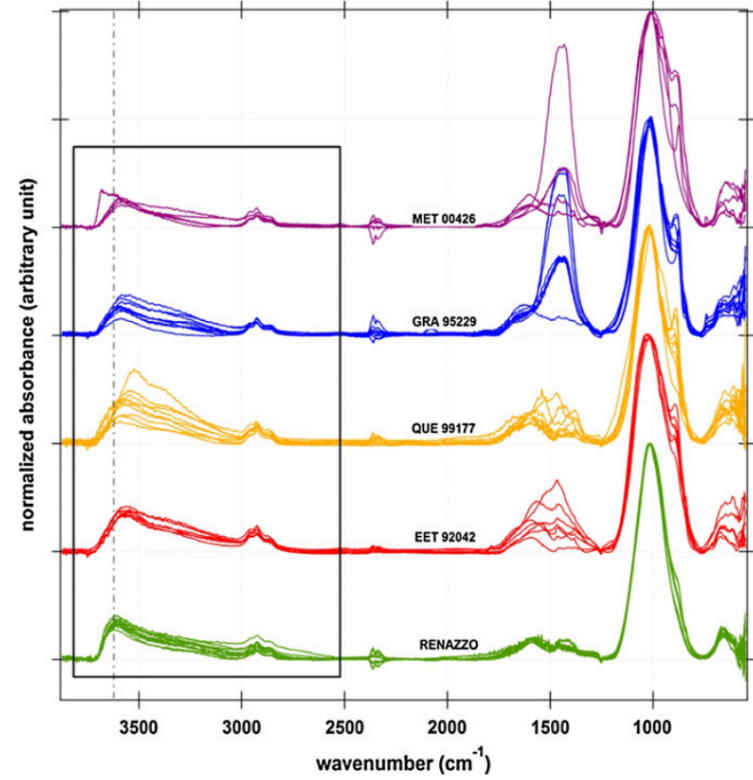- Will be continously improved thanks to laser development
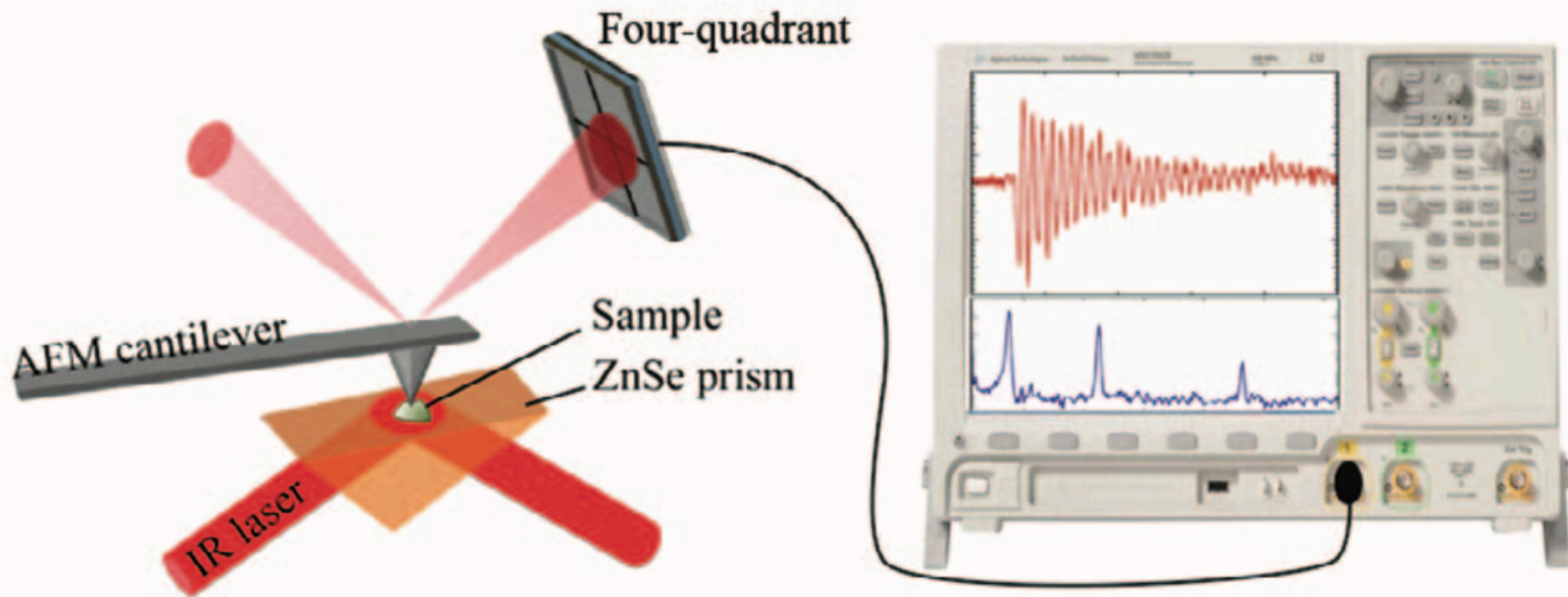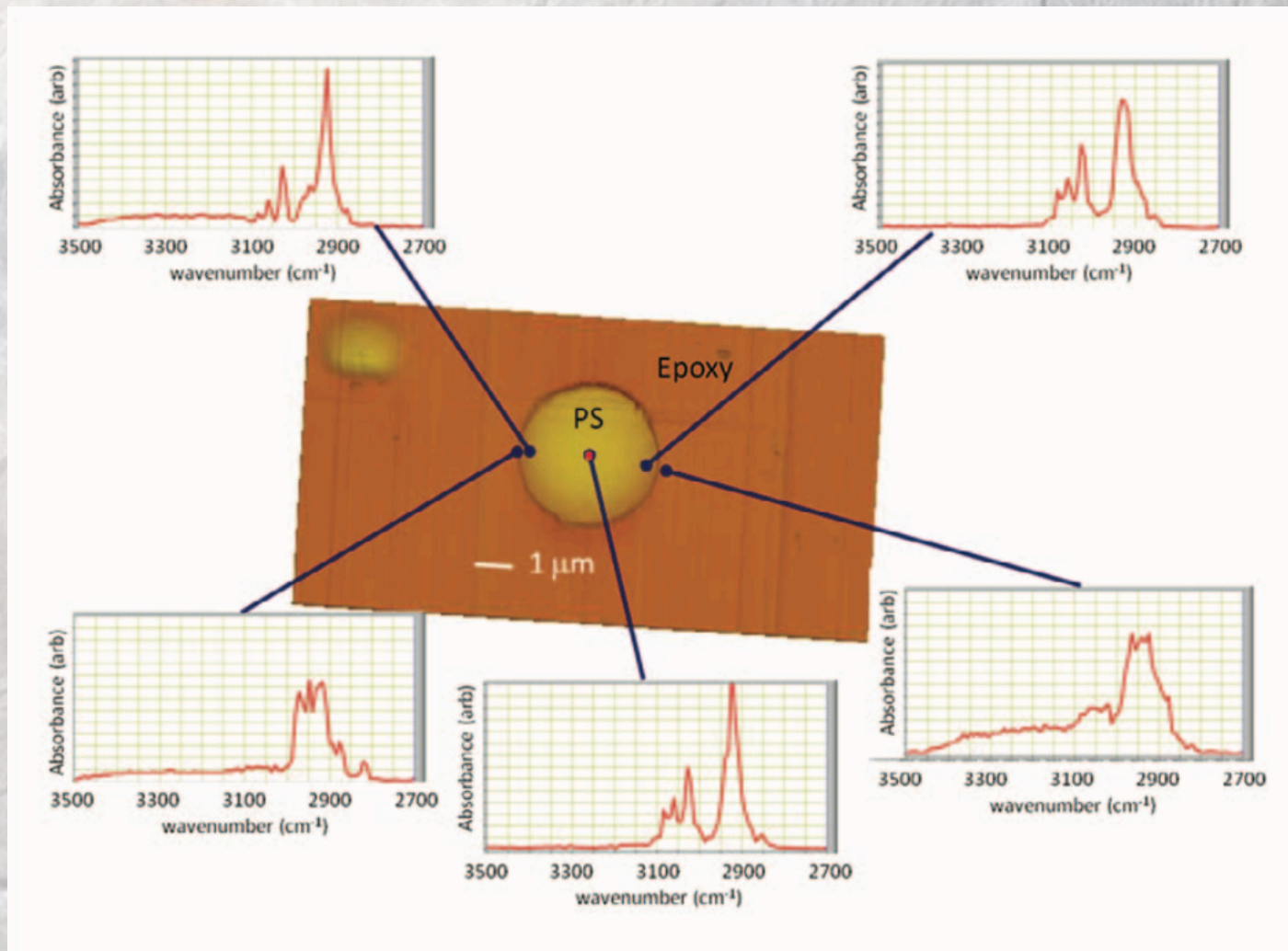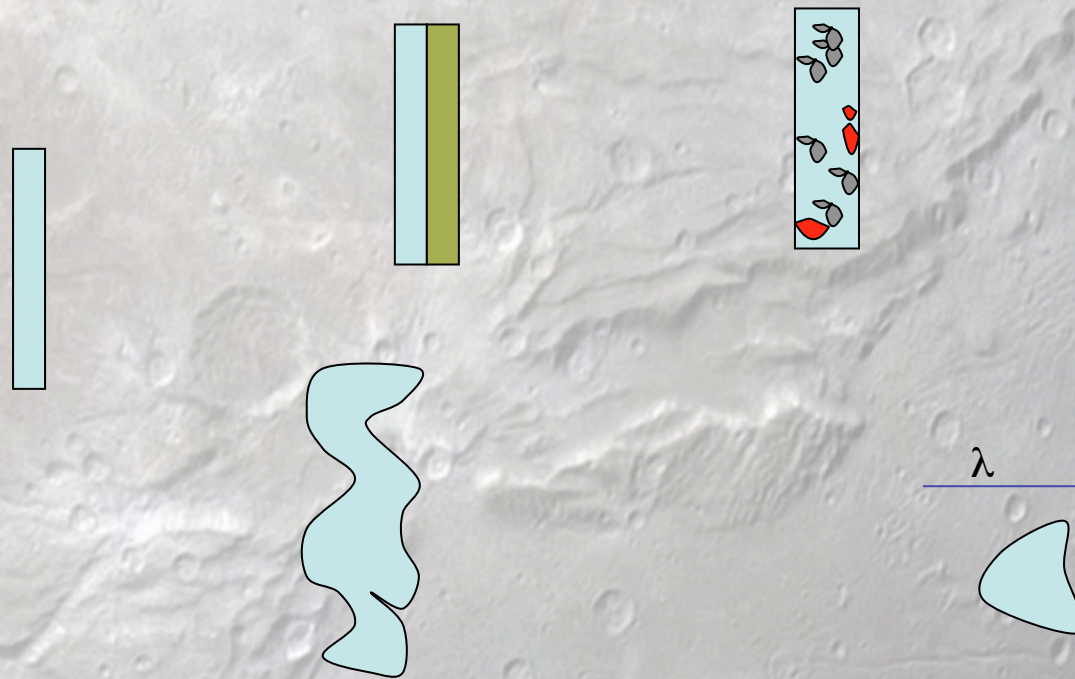
Dazzi et al. (2012) Applied Spectroscopy
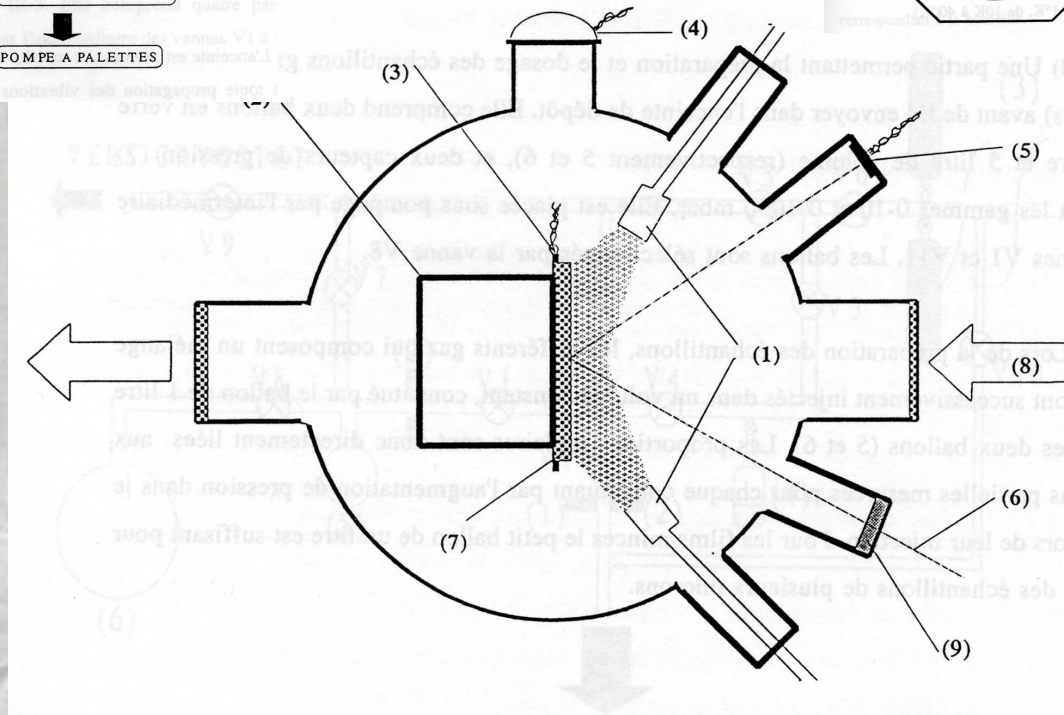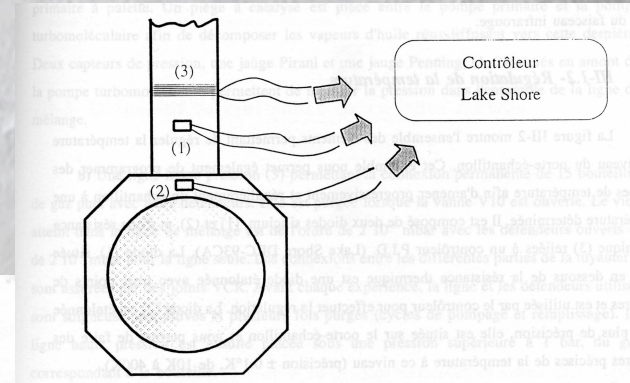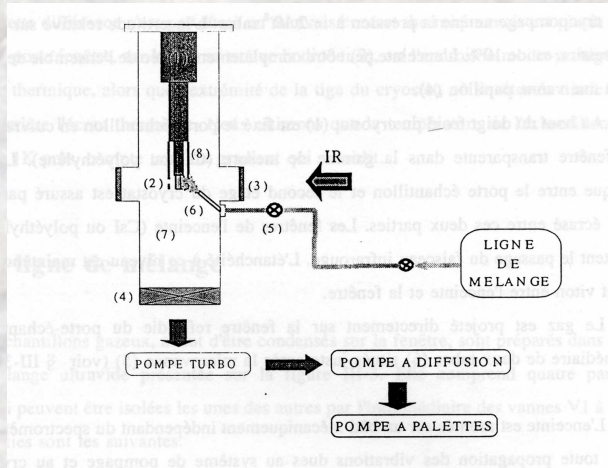
Test on a natural sample : CR matrix

Bonal et al. (2013)

Sample preparation: a critical issue

☑ Quantification
☑ Spectral quality
☑ Band saturation and signal-to-noise ratio

λ

Formation of thin films from the gas
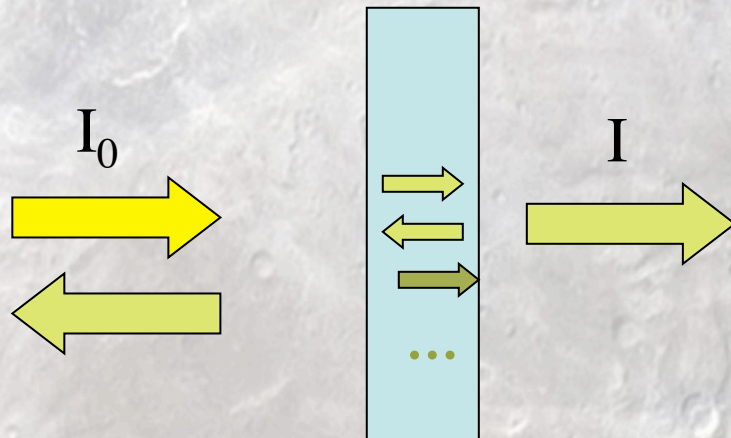
Absorption and radiative transfert

- Solid sample must be thin enough (< tens of micrometers)
- Reflection/transmission at each dioptre => interferences

I_0 I

...

✓Spectrum = f(n,k)
✓Optical modeling required

- Control thickness and planeity/rugosity by interfgerometry (de 10-100 nm à ~ 100 µm)
- Controlled conditions of deposition and annealing (substrate, température, deposition rate)
- Monocrostalline or polycrystalline samples.
- Contamination (eau, CO2…).
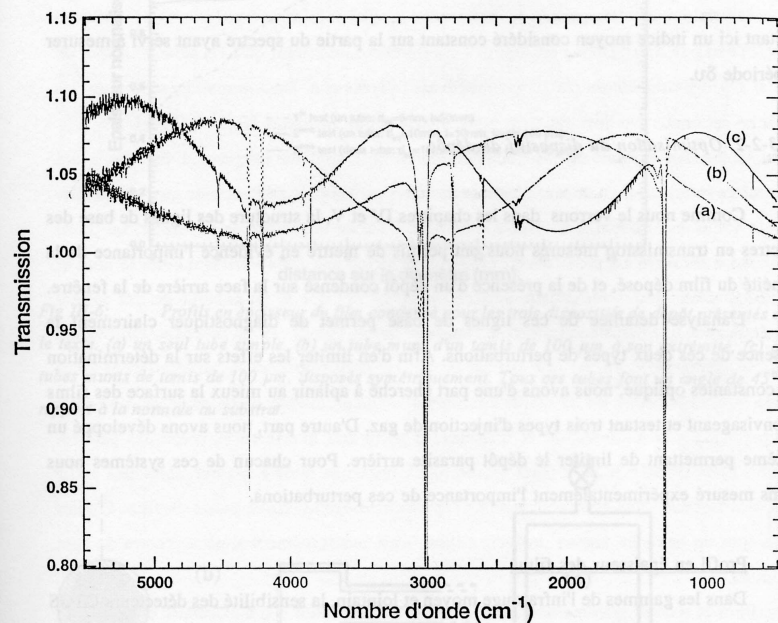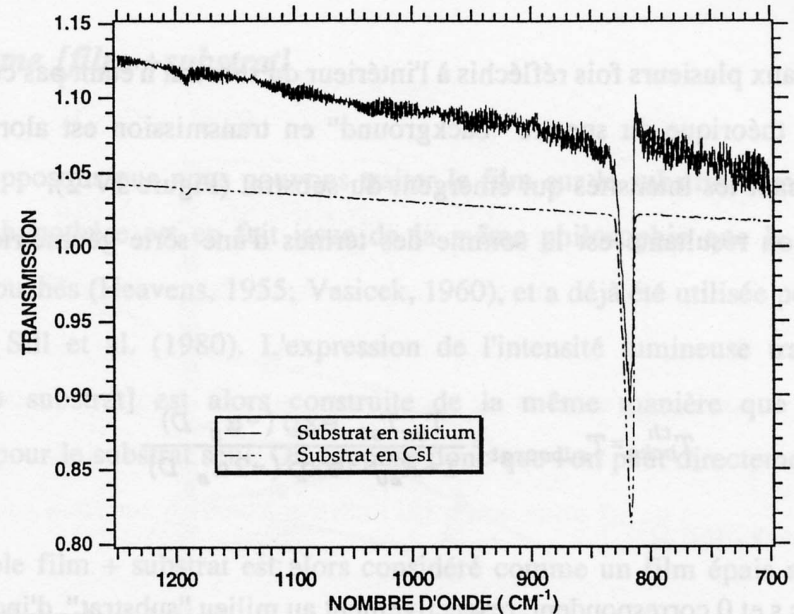- Index gradient possible for the first monolayers.

Fig III-5:   *Spectres du méthane obtenus pour différentes épaisseurs. Les interférences dans la ligne de base correspondent respectivement à 0.9 µm (a), 1.25µm (b) et 1.8µm (c).*
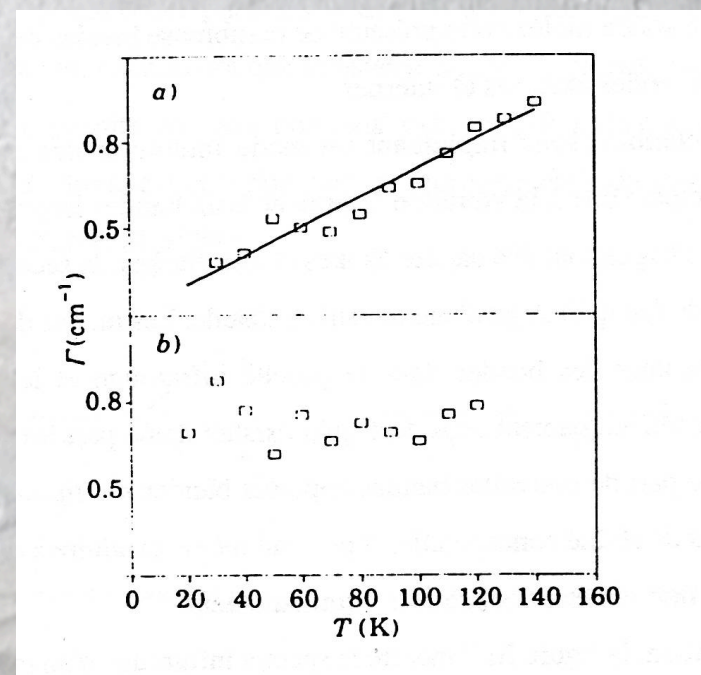

C2H6 ice films on CsI and Si substrates. Planeity and refractive index control the continuum and n-artifact in the absorption band.

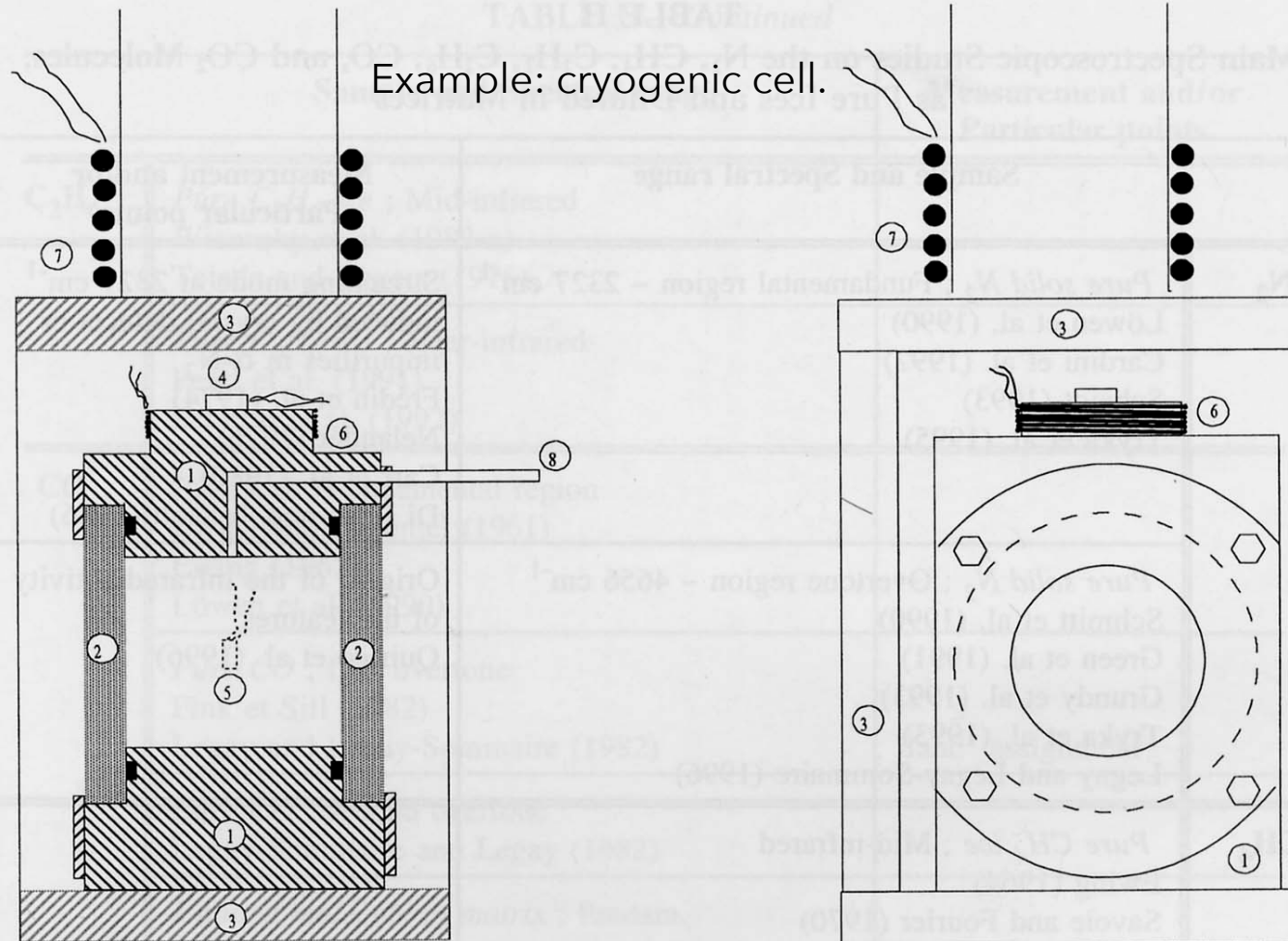# Spectroscopic criterion of crystal quality: vibrational relaxation
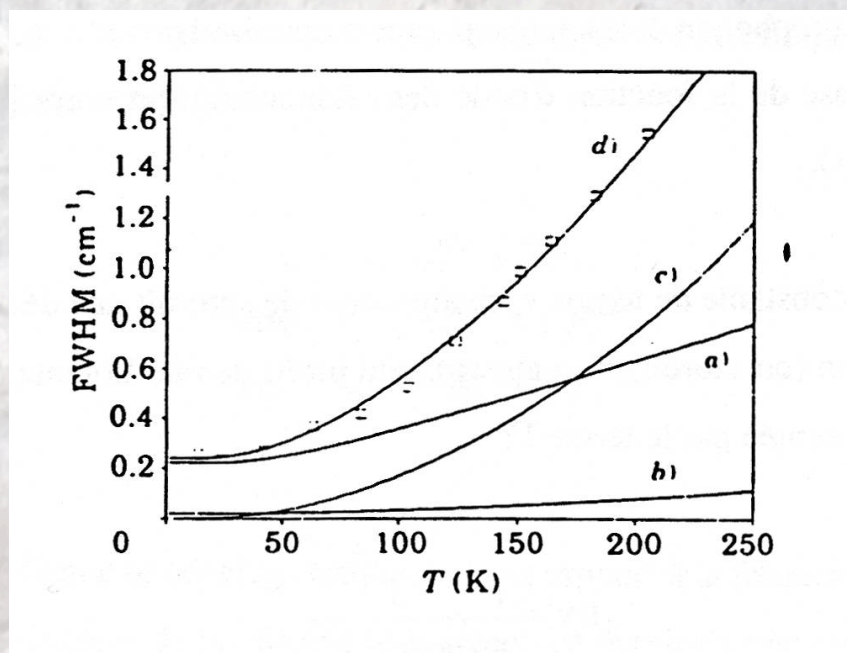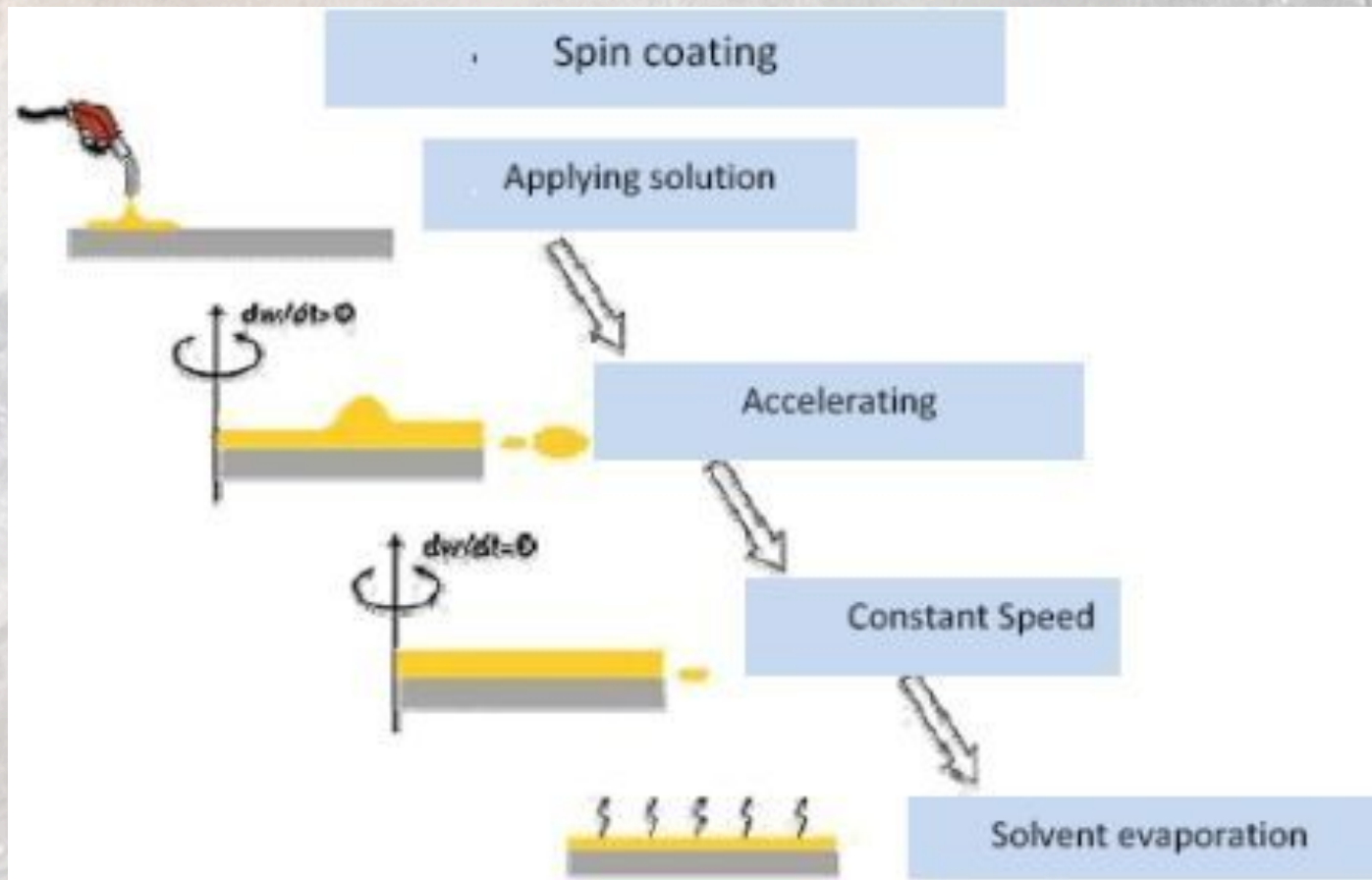

Naphtalene of breathing mode at 1362 cm-1 contrôled by temperature, for a monocrystal with excellent quality.
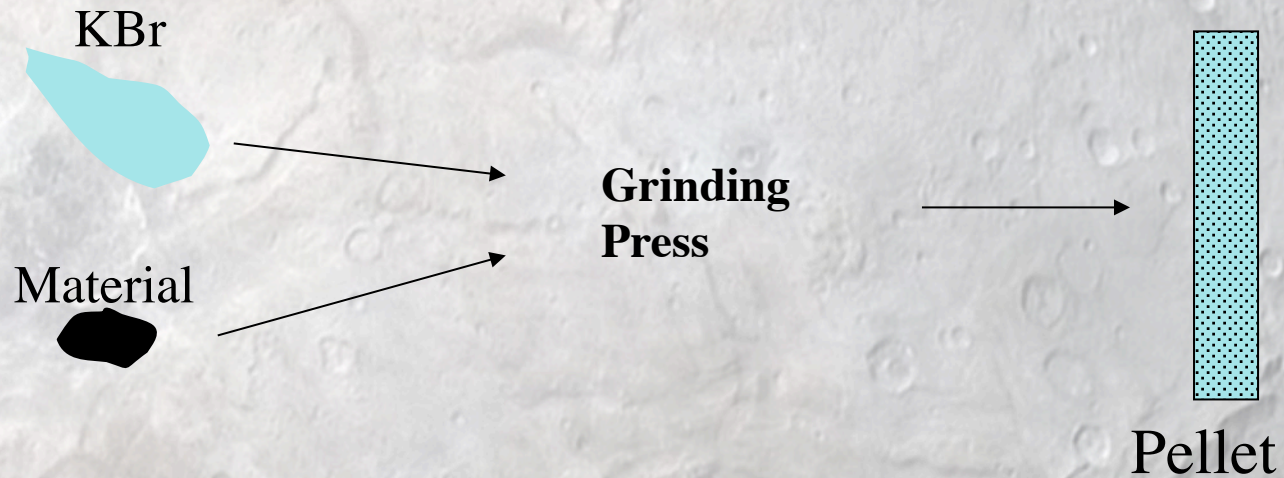
CS2 - n_1+n_3. Relaxation by cristallographic defects in a polycristal (bottom) phonon interaction in a monocristal (top).

Cristal growth from the liquid phase

Example: cryogenic cell.

Spin coating

Applying solution

Accelerating

Constant Speed
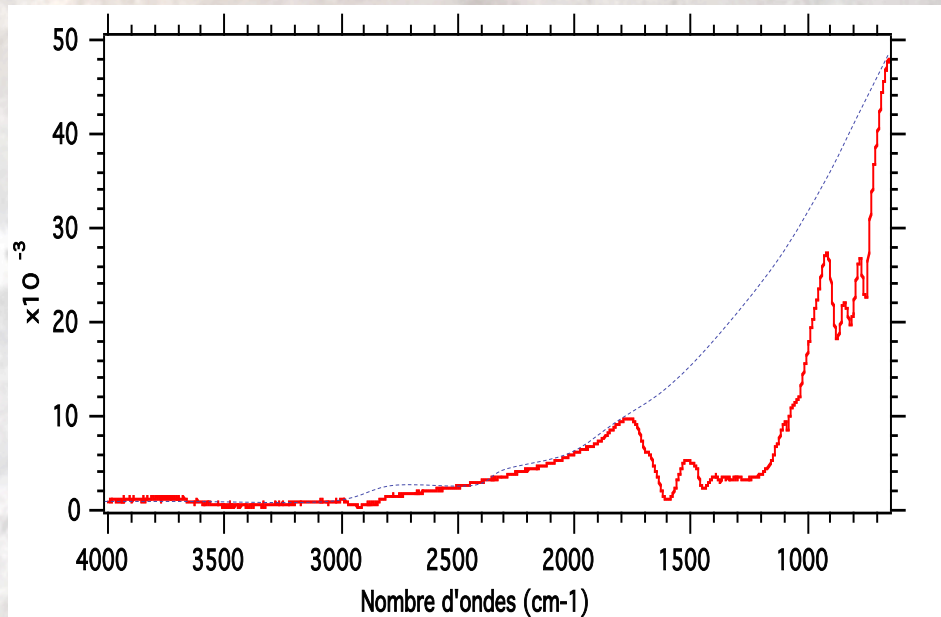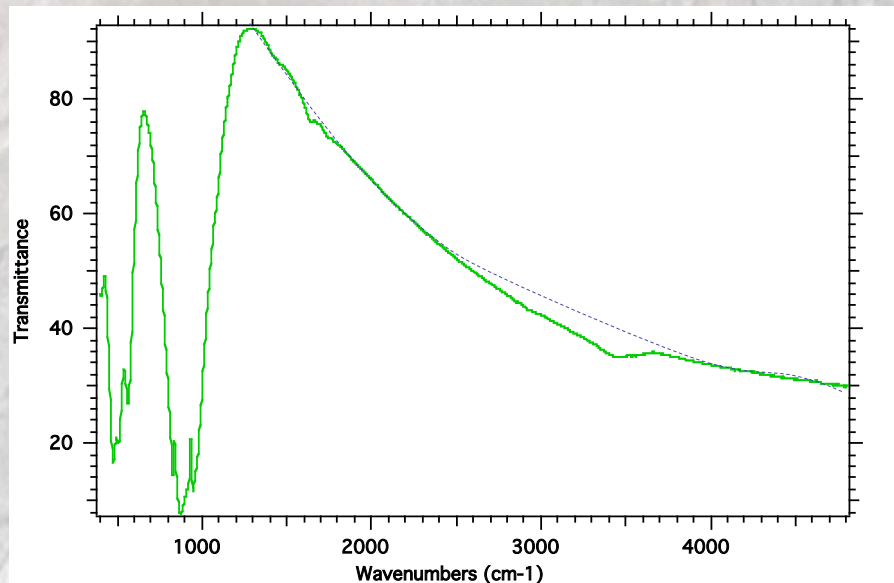
Solvent evaporation

Measurements on pellets

KBr

Material

Grinding Press

Pellet

✓ Robust material (resistant to grinding)
✓ Scattering and water contamination
✓Quantification difficult: require radiative transfert and scattering modeling
✓No control on crystal orientation

coal

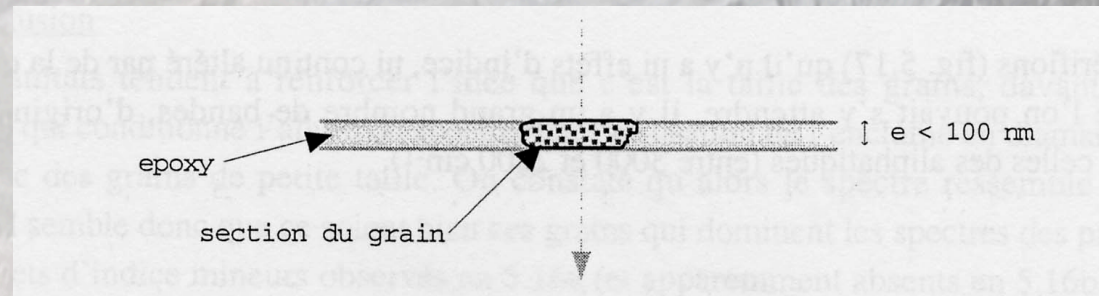Olivine San Carlos

Ultramicrotomy

Standard thin section (30 μm): limited to NIR in transmission, epoxy contamination.

Double-polishing : suitable for faint feature in NIR (e.g. structural OH)

- ✓ thins (~ 1 μm)
- ✓ ultra-thin (20-200 nm)

epoxy

section du grain

$e < 100$ nm

✓Epoxy vs Organic matter
✓Hard material = difficult

Pressing (soft samples)

- ISO 7 clean room, under an ISO 5 laminar hood.
- Micromanipulation by hand

4 mm
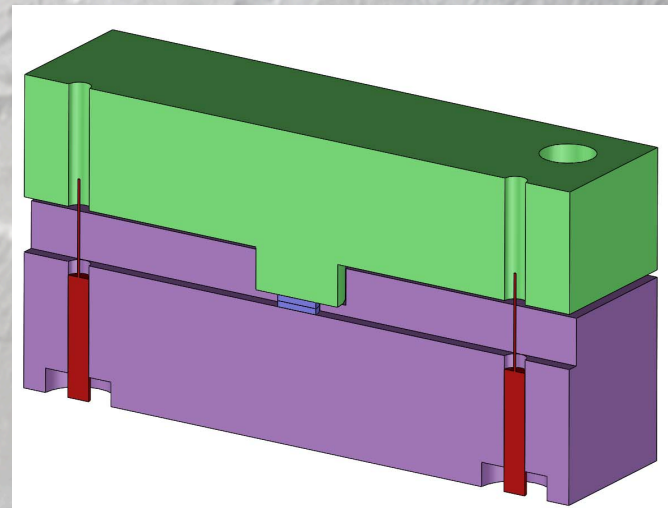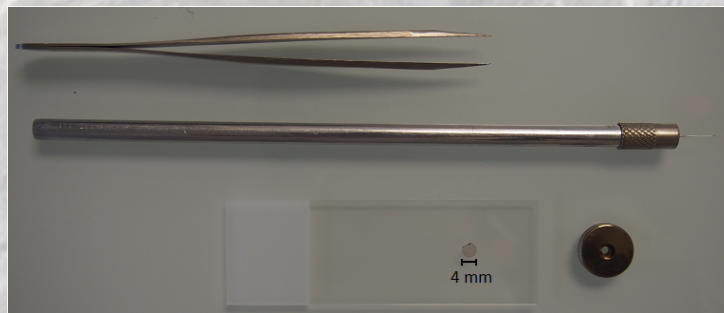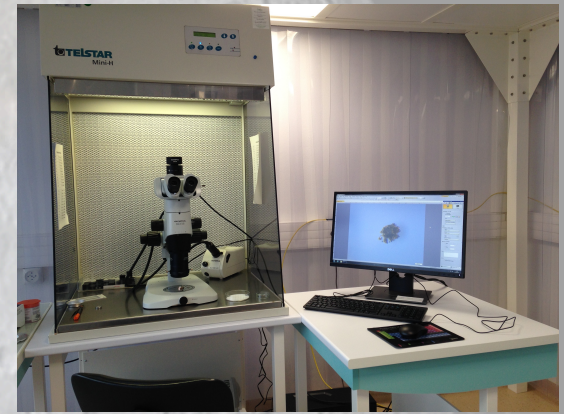
MEB images (SE2)
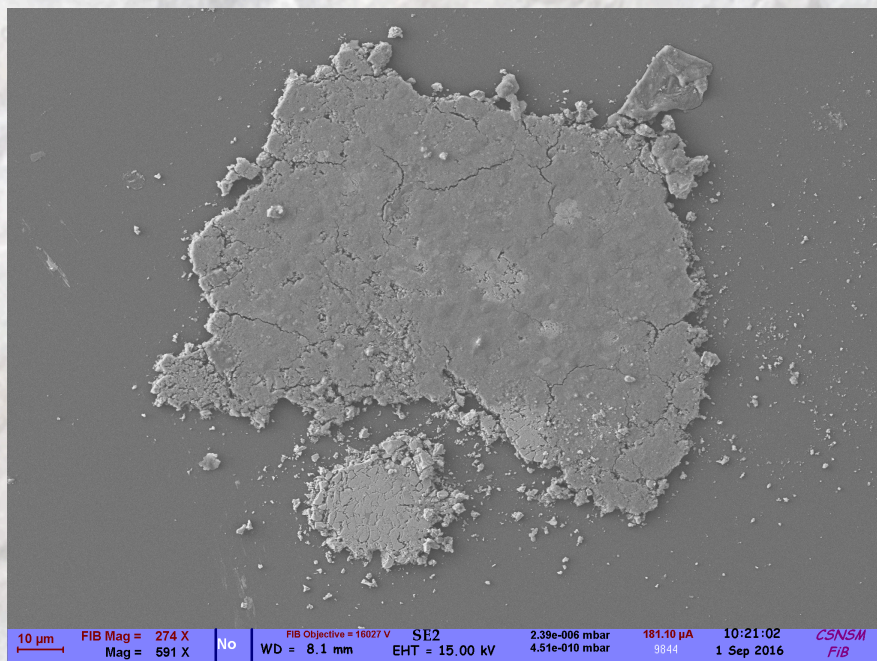
Crushed on diamond window
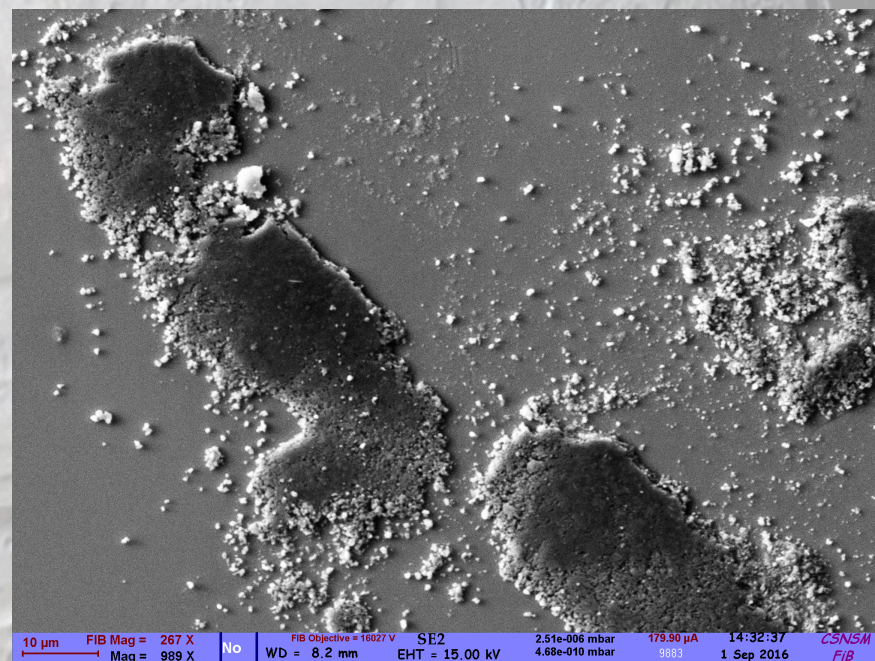
Crushed on Germanium window

Figure 5.8c axis: Absorbance — nombre d'onde (cm⁻¹)

grain 4 - 20x25 µm (D1=70 µm; 256 scans, 4 cm⁻¹)

standard /8
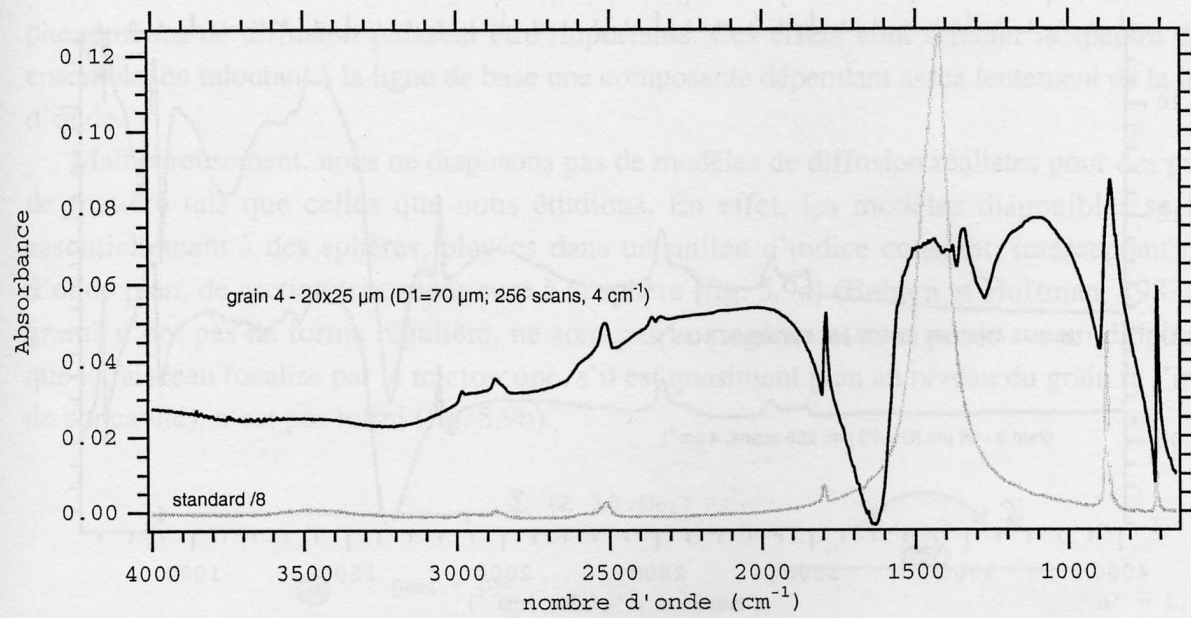
Figure 5.8c: Calcite, grain 4 + référence

Figure 5.8d axis: Absorbance — nombre d'onde (cm⁻¹)

grain 6 - 6 µm (D1=24x24 µm; 512 scans, 4 cm⁻¹)

standard /16 -0,06
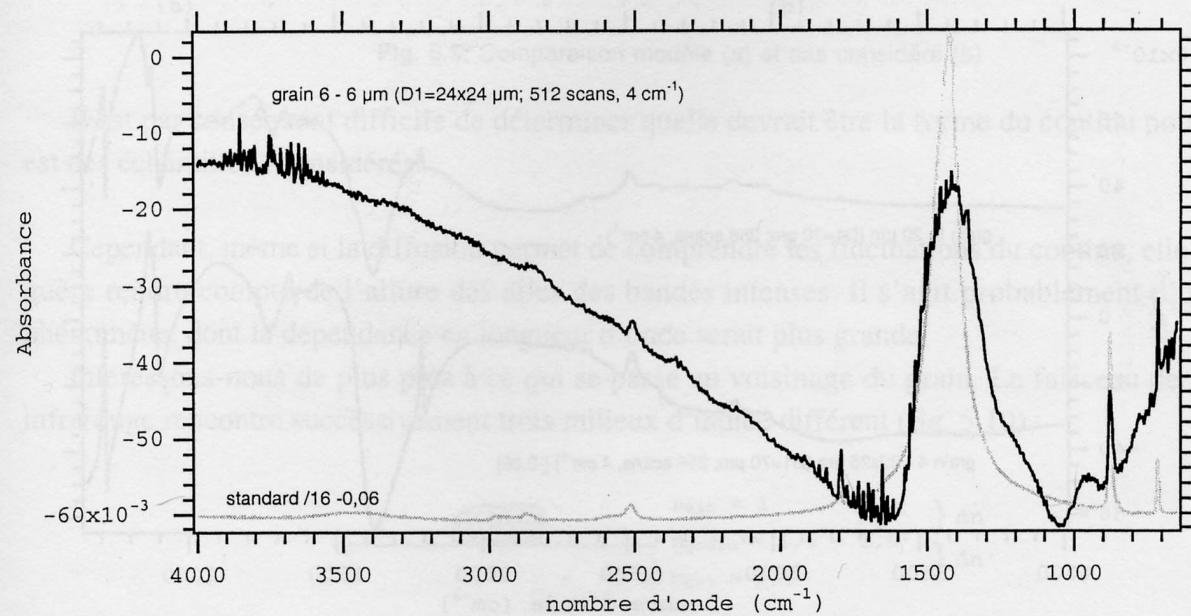
Figure 5.8d: Calcite, grain 6 + référence

Part III - Applications

III.1 - Geomaterials in the laboratory
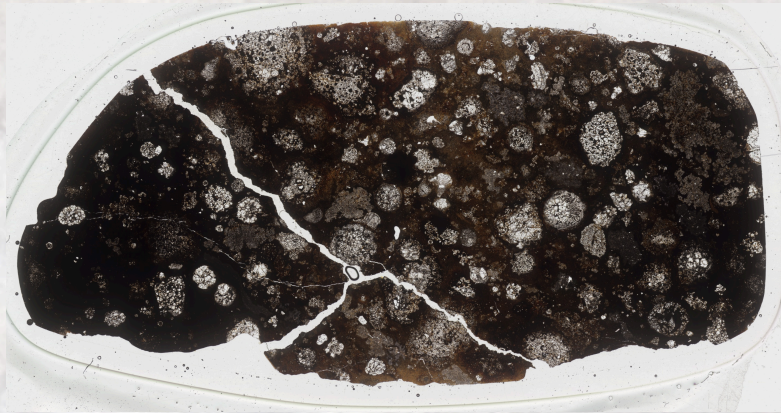
Minerals
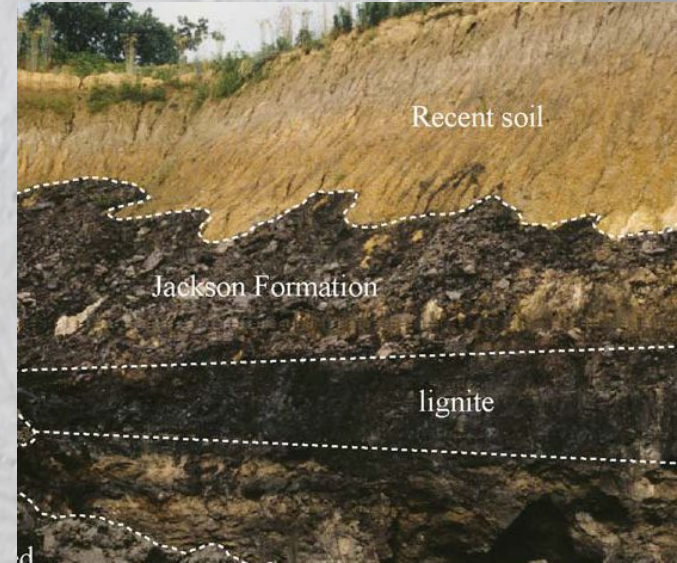
Water + fluids

Organic matter

Usual minerals

Silicates	Tectosilicates	Si polymorphs, Feldspaths, …
	Inosilicates	Amphiboles, pyroxens, …
	Nesosilicates	Olivines, Garnets, …
	Phyllosilicates	Micas, Chlorites, serpentine, …

Carbonates

Sulfates

Sulfides

Phosphates

Oxides/Hydroxides

Mineralogy of cometary grains

Merouane et al. 2014 A&A
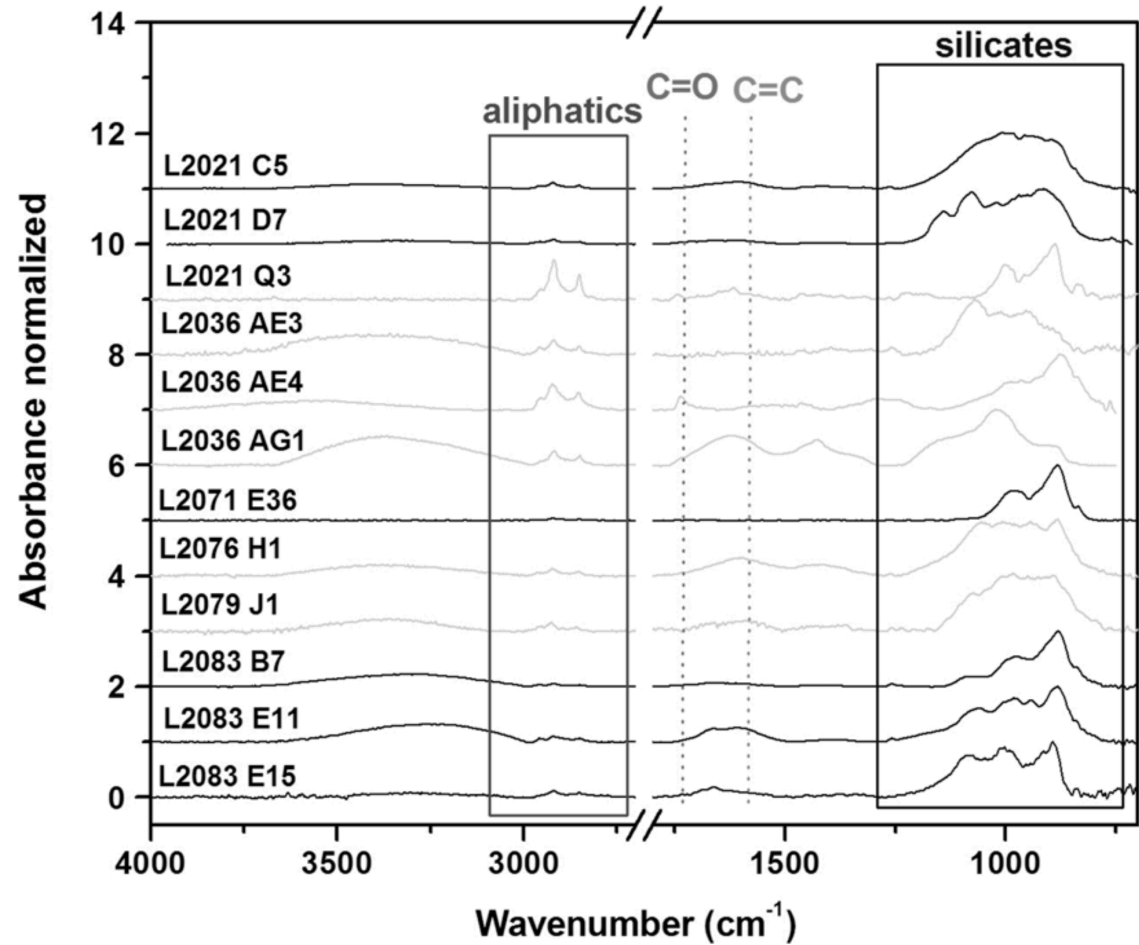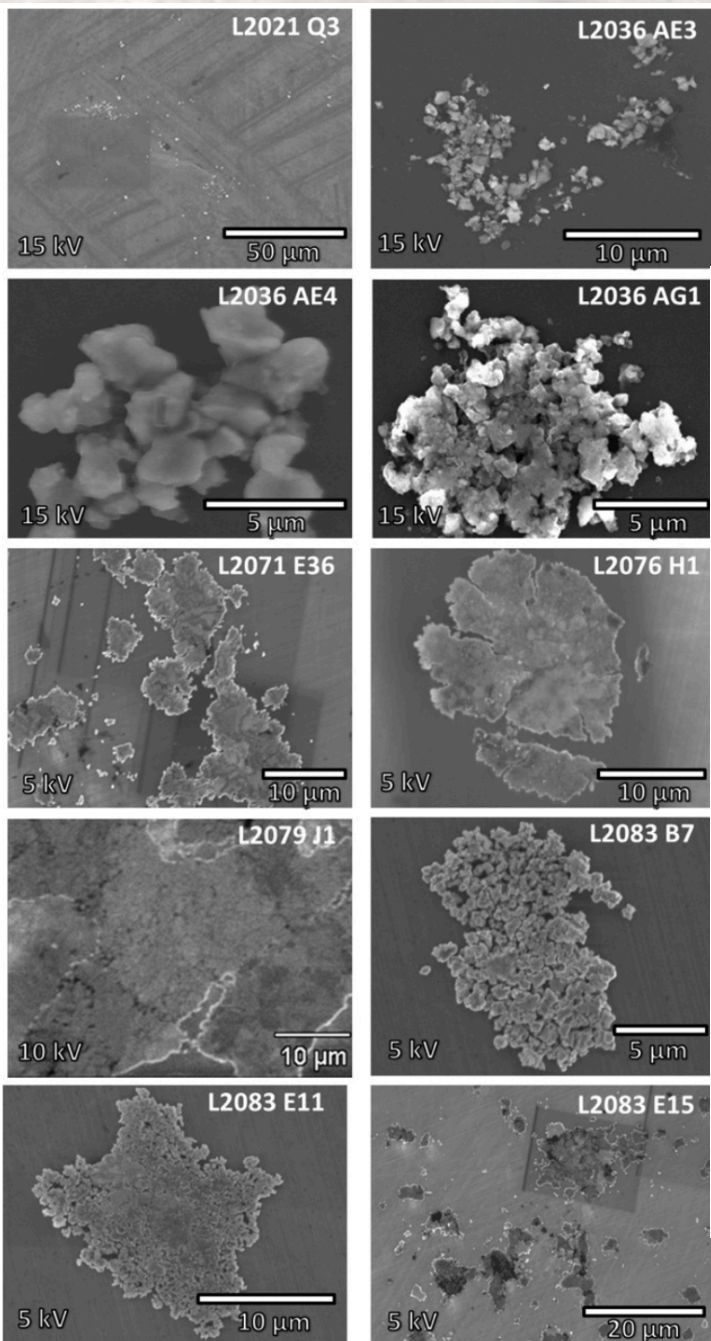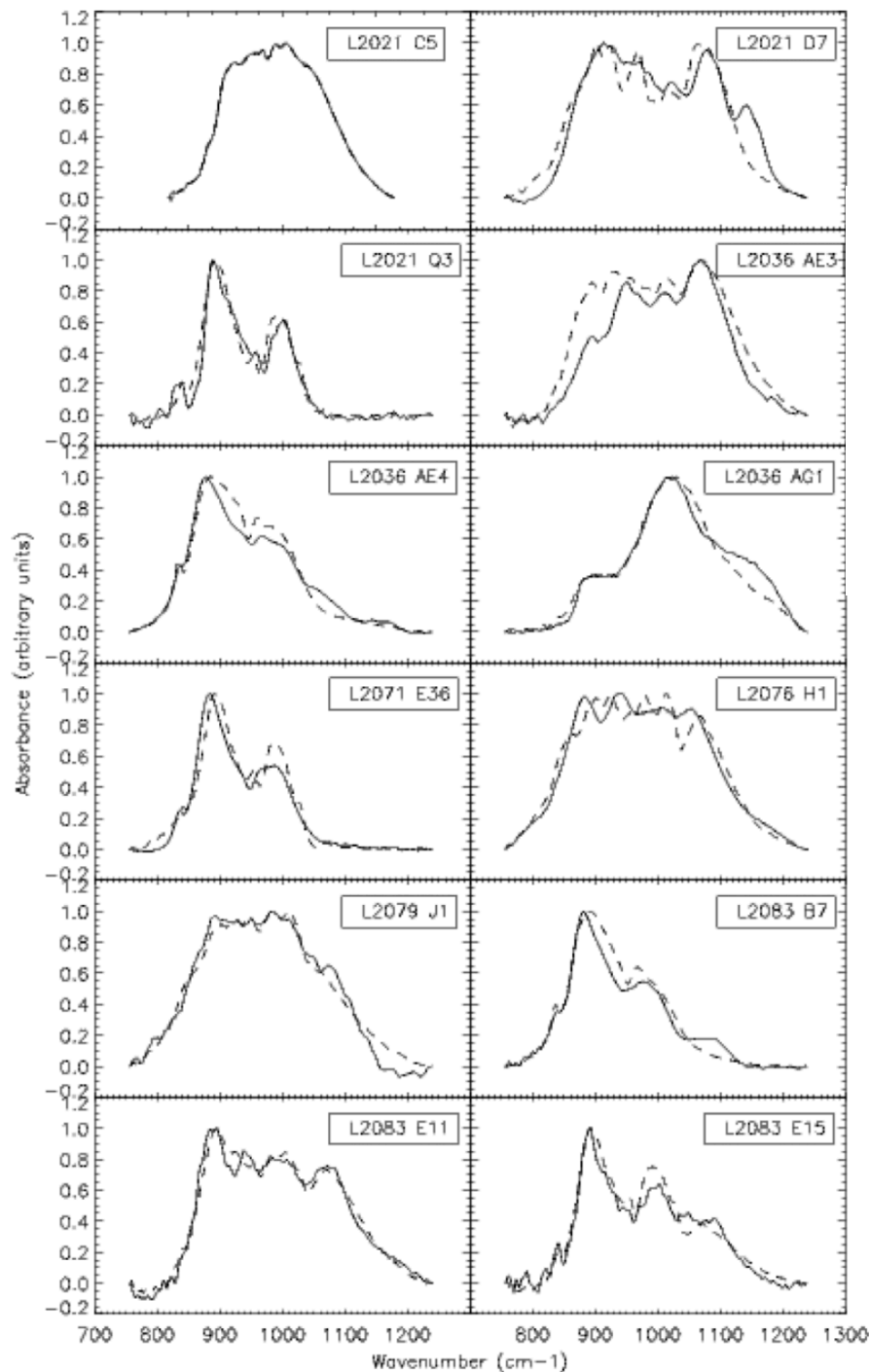
Linear combination of end-members

1. Fe and Mg end members of olivine (forsterite: Mg_2SiO_4 and fayalite: Fe_2SiO_4, noted as Fo and Fa, respectively, in the following sections).
2. Mg end member and Ca–Mg solid solution of pyroxene (enstatite: $MgSiO_3$ and diopside: $CaMgSi_2O_6$ noted as En and Di, respectively, in the following sections).
3. Amorphous compounds of Fe and Mg olivine end members compositions and an amorphous compound of pyroxene Mg end member composition.

Table 3
Silicate Composition of Each Particle Given by Our Fitting Procedure

Particle	ol/(ol+px)	Mg/(Mg+Fe)	Ca/(Ca+Mg)	Amorphous Content
L2021 C5	**0.7**	**1**	**0**	**35%**
L2021 D7	**0.1**	**1**	**0.6**	**0%**
L2021 Q3	1	0.95	⋯	0%
L2036 AE3	0	1	0	0%
L2036 AE4	1	0.45	⋯	0%
L2036 AG1	0.15	1	0.025	80%
L2071 E36	**1**	**0.75**	⋯	**5%**
L2076 H1	0.3	1	0.075	0%
L2079 J1	0.7	1	0	45%
L2083 B7	**0.95**	**1**	**0**	**0%**
L2083 E11	**0.65**	**1**	**0**	**0%**
L2083 E15	**0.35**	**1**	**0**	**0%**

Mg-Rich Silicate Crystals in Comet Hale–Bopp: ISM Relics or Solar Nebula Condensates?
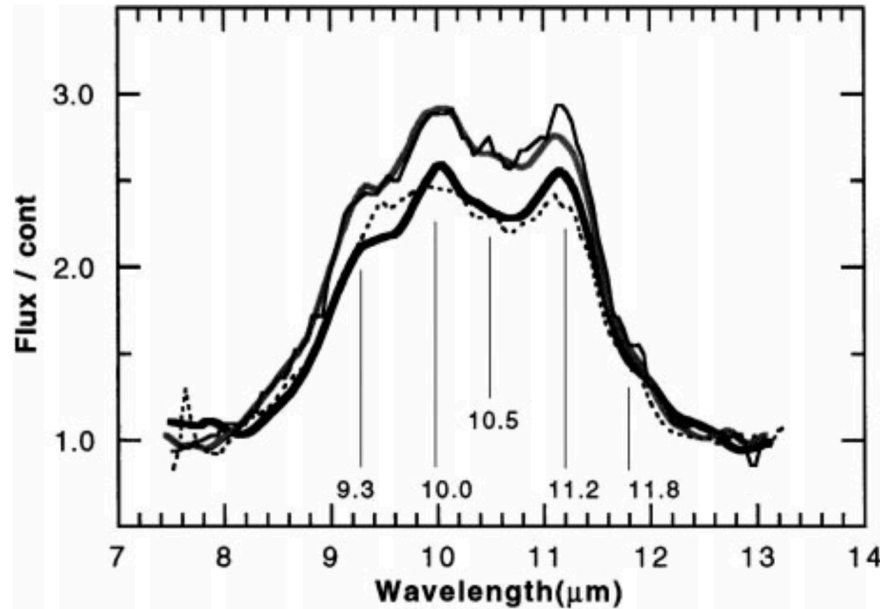
FIG. 1. Silicate features in Comet Hale–Bopp at four epochs, fitted with smooth curves (smoothed over ∼0.24 μm at all epochs except over ∼0.48 μm at 2.8 AU) using a least-squares algorithm (Bevington 1969). The silicate features are shown by the flux-to-continuum ratios (Hanner *et al*. 1994b), with continuum parameters from Wooden *et al*. (1999). The silicate features flux/cont are derived from the HIFOGS spectra on 1996 October 07–14 UT at 2.8 AU (preperihelion) (*heavy black line*), 1997 February 14–15 UT at 1.2 AU (preperihelion) (*heavy gray line*), 1997 April 11 UT at 0.93 AU (∼perihelion) (*thin black line*), and June 24–25 UT at 1.7 AU (post-perihelion) (*dotted line*). The principal peaks of the crystalline ortho-pyroxene at 9.3 and 10.5 μm and of crystalline olivine at 10.0, 11.2, and 11.8 μm (Koike *et al*. 1993) are marked (*vertical hairlines*).
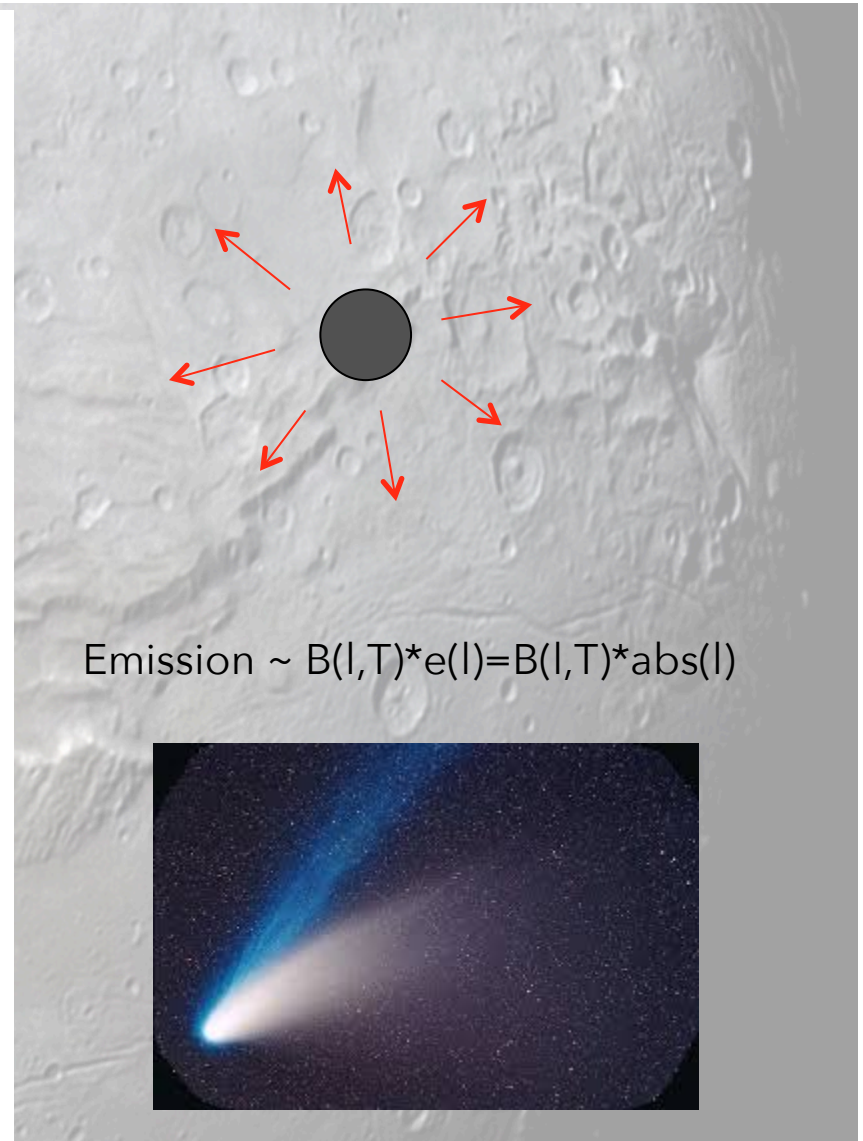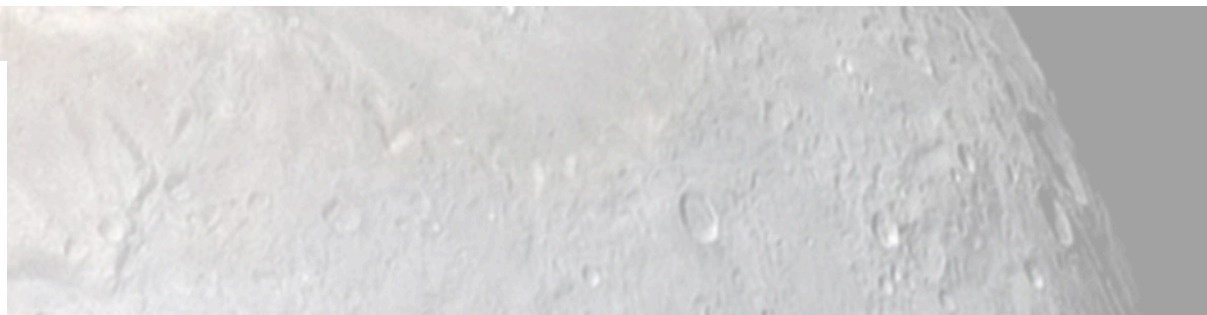

Emission ~ B(l,T)*e(l)=B(l,T)*abs(l)

a) Olivine IDP

b) Pyroxene IDP

Optical Extinction Q_{ext}

c) Layer-lattice IDP

Wavelength (μm)

a) 2.8 AU

b) 1.2 AU

Flux / cont

c) 0.93 AU

d) 1.7 AU

Wavelength (μm)
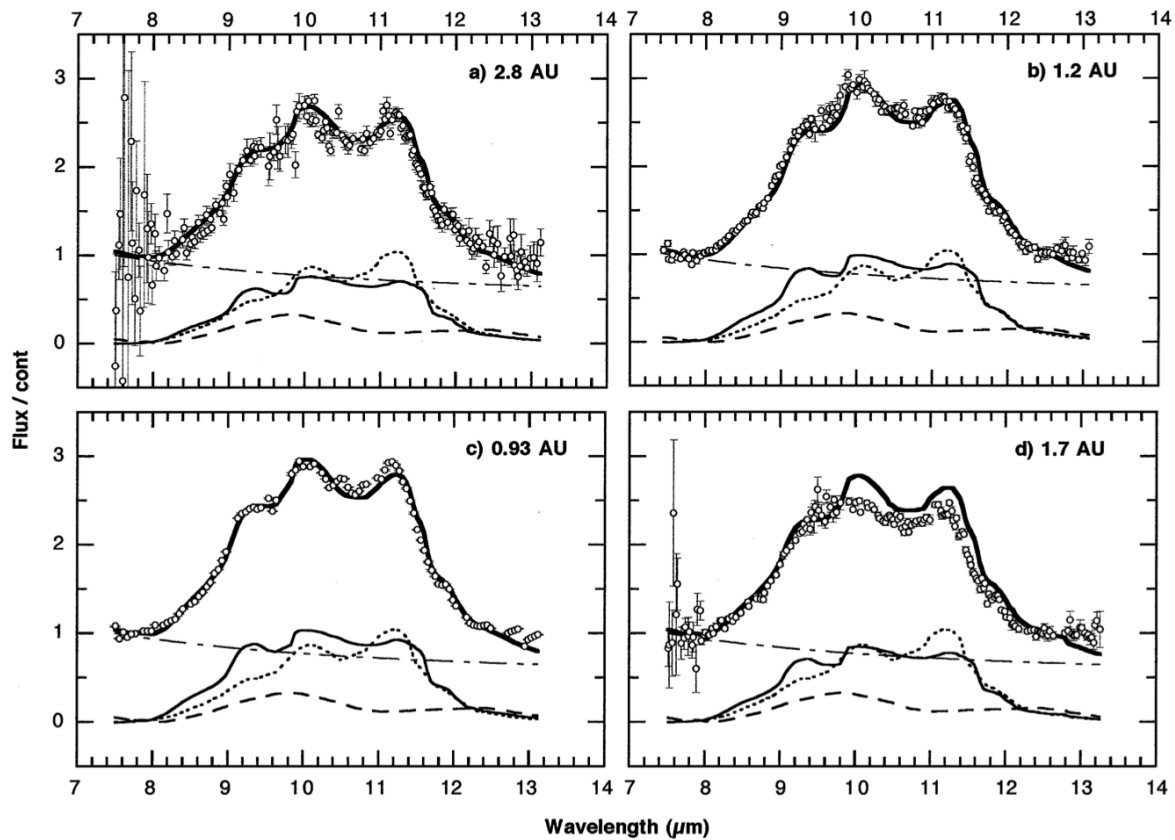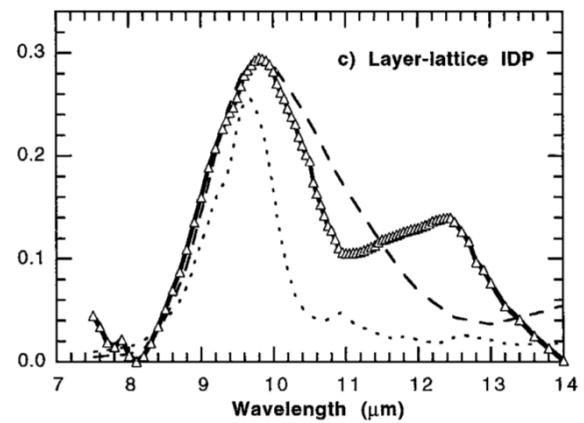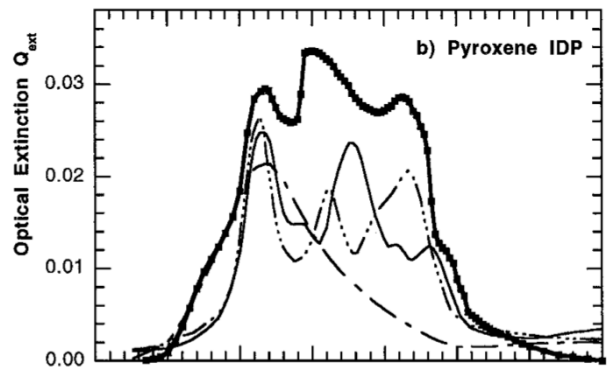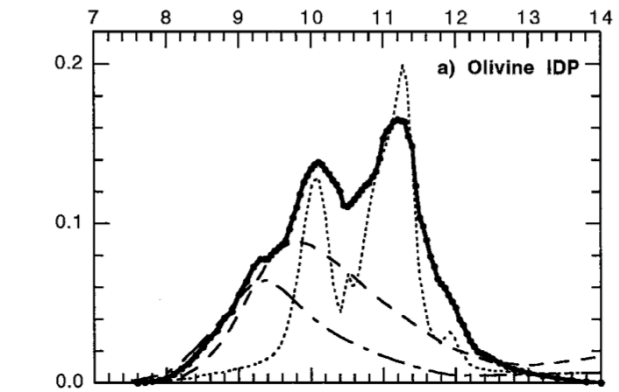
THE INFRARED SPECTRUM OF COMET HALE-BOPP*

J. Crovisier[1], K. Leech[2], D. Bockelée-Morvan[1], T.Y. Brooke[3],
M.S. Hanner[3], B. Altieri[2], H.U. Keller[4], E. Lellouch[1]

almost pure forsterite
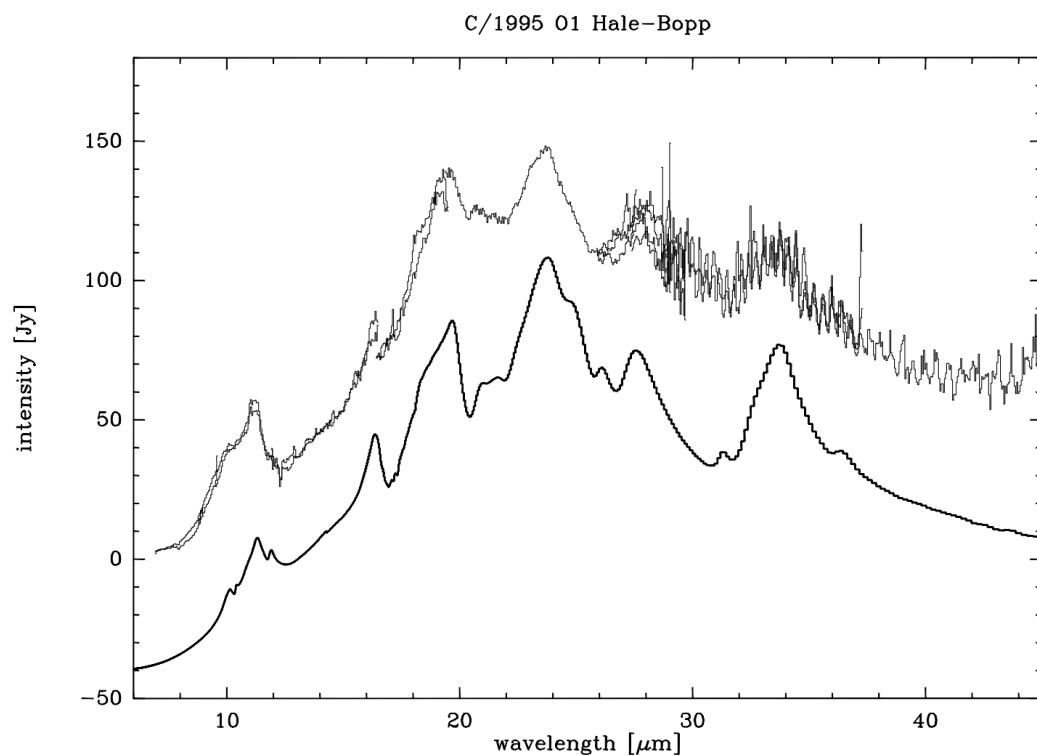
Figure 4. The SWS spectrum of C/1995 O1 (Hale-Bopp) and a modelled spectrum of forsterite (from a laboratory spectrum provided by W.-F. Thi and L. d'Hendecourt).

Probing water in geomaterials
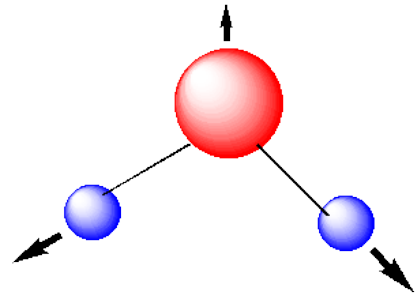
Symmetric Stretch
3657 cm^{-1}
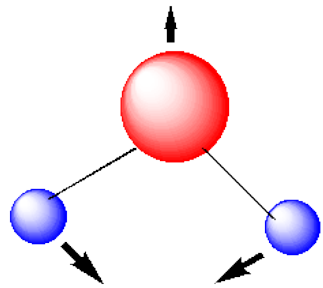
Bend 1595 cm^{-1}
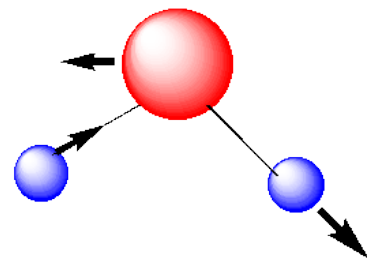
Asymmetric Stretch
3756 cm^{-1}

Liaison hydrogène

Oxygène

Hydrogène

a)

b)

H_2O

crystalline 60 K
········ Amophous 15-35 K

1.0

0.5

0.0

4000   3000   2000   1000   0

Wavenumber (cm^{-1})

a.

b.

OH$^-$

H_3O^+

D

L
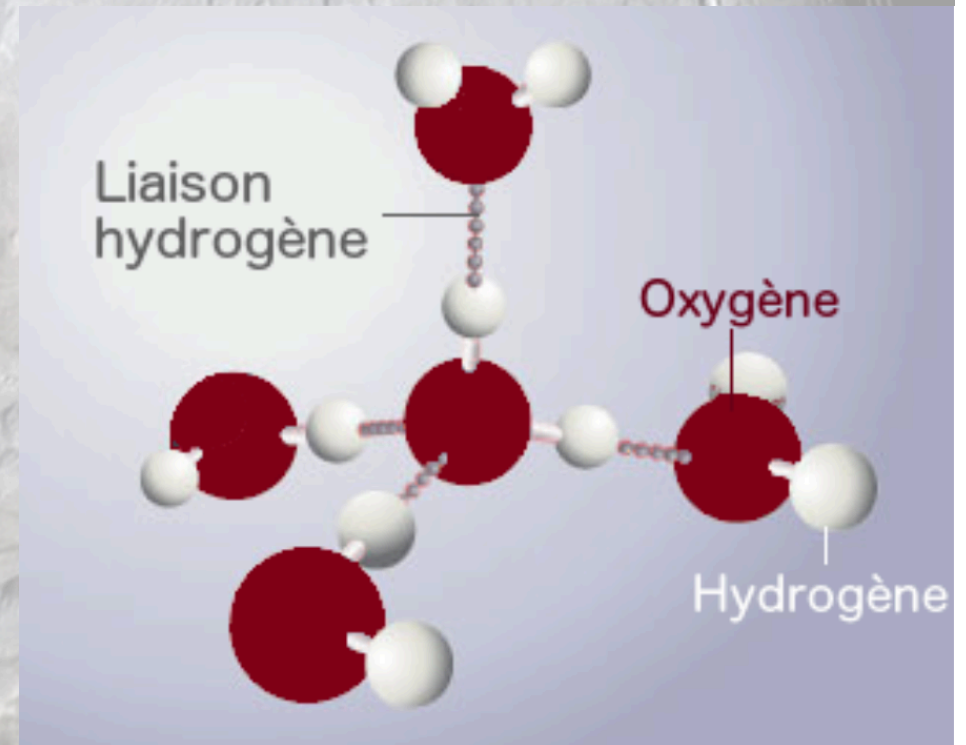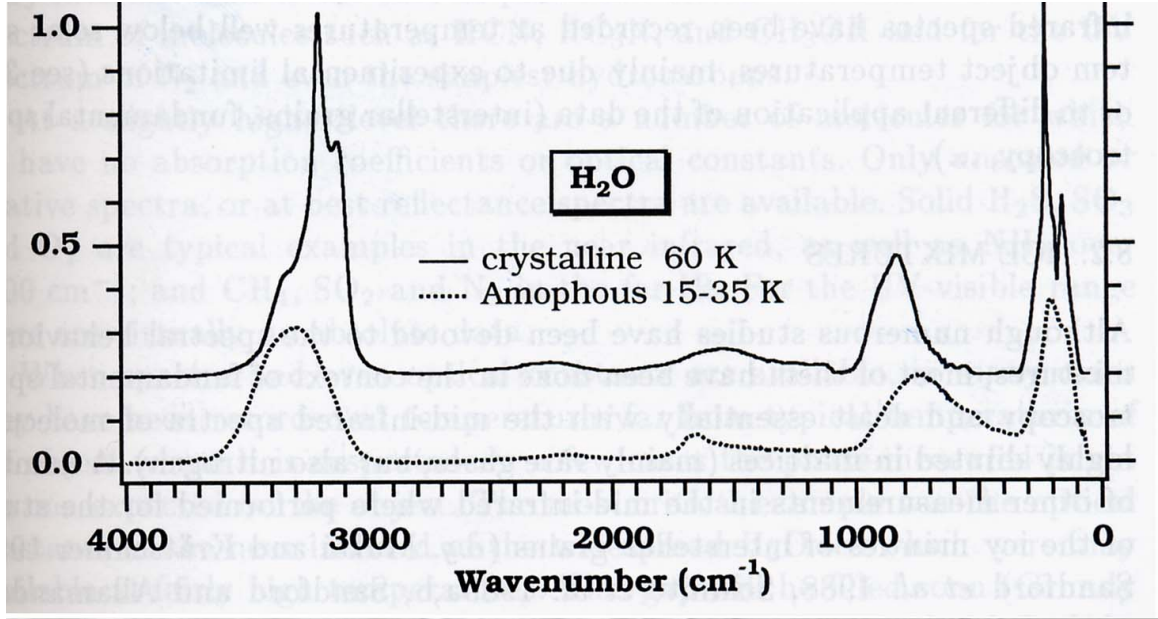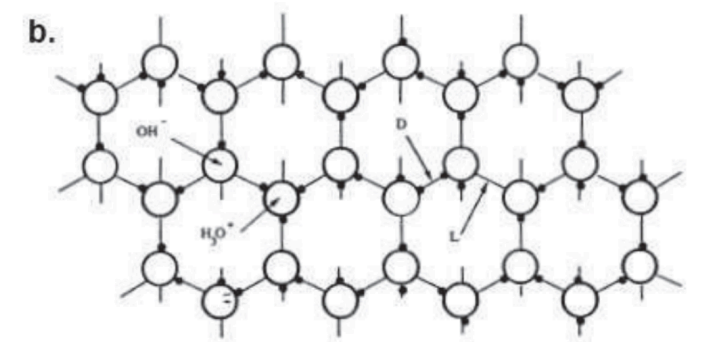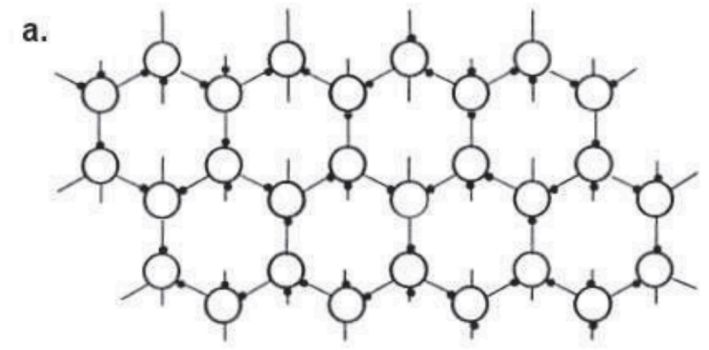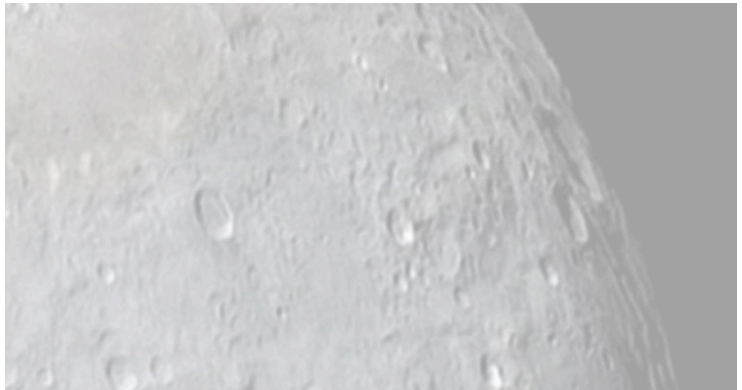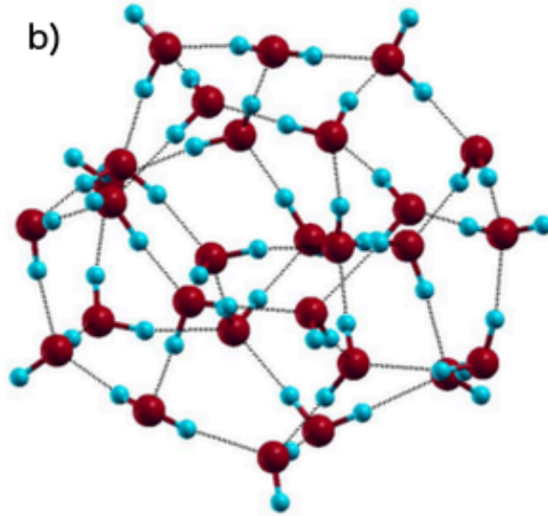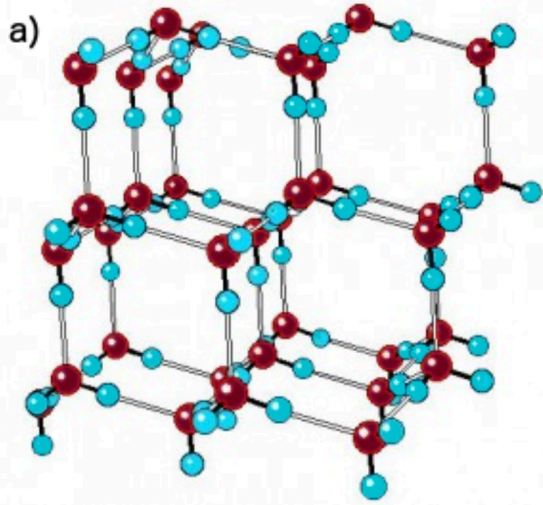
Hydroxyls and molecular water in clays

SERPENTINE - KAOLIN
$(x \sim 0)$

$c \cdot \sin \beta = 7.1 - 7.3$ Å

TALC - PYROPHYLLITE
$(x \sim 0)$

9.1 - 9.4 Å
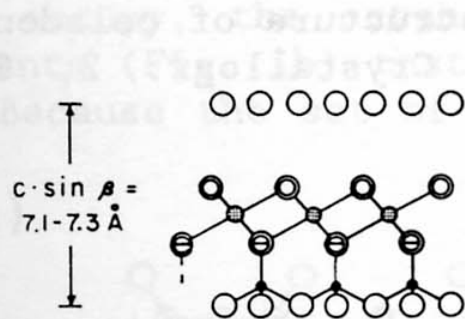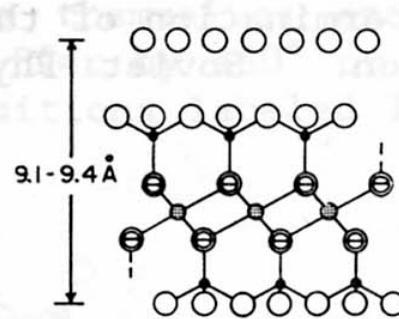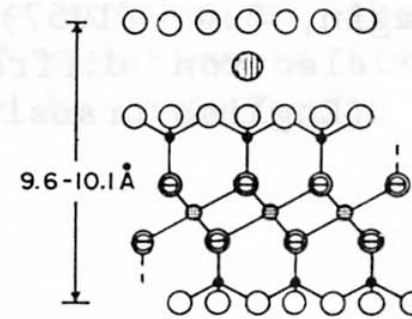
MICA $(x \sim 1.0)$ and
BRITTLE MICA $(x \sim 2.0)$

9.6 - 10.1 Å
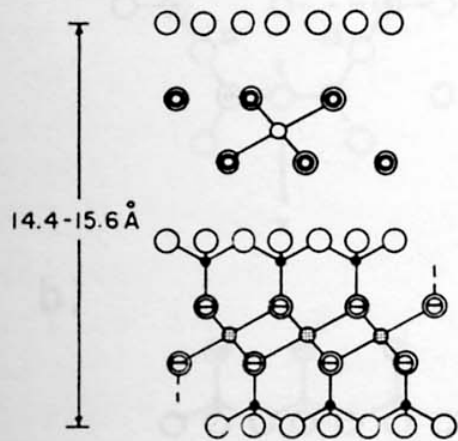
SMECTITE $(x \sim 0.25 - 0.6)$ and
VERMICULITE $(x \sim 0.6 - 0.9)$

14.4 - 15.6 Å
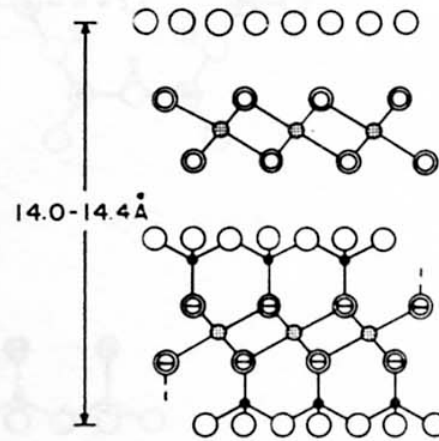
CHLORITE
$(x$ is variable$)$

14.0 - 14.4 Å

• = Tetrahedral cation
⊖ = Octahedral cation
⦀ = Interlayer cation
○ = Exchangeable cation

○ = Oxygen
◎ = Hydroxyl group
◉ = Water molecule
⊖ = Oxygen + Hydroxyl
       (in projection)

Layer type	Interlayer	Group*	Subgroup	Species
1:1	None or H₂O only	Serpentine-kaolin $x \sim 0$	Serpentines	Chrysotile, lizardite, amesite, berthierine, cronstedtite, etc
			Kaolins	Kaolinite, dickite, nacrite, halloysite
2:1	None	Talc-pyrophyllite $x \sim 0$	Talcs	Talc, willemseite
			Pyrophyllites	Pyrophyllite, ferripyrophyllite
	Hydrated exchangeable cations	Smectite $x \sim 0.2-0.6$	Saponites	Saponite, hectorite, sauconite, stevensite, etc.
			Montmorillonites	Montmorillonite, beidellite, nontronite, volkonskoite, etc.
	Hydrated exchangeable cations	Vermiculite $x \sim 0.6-0.9$	Trioctahedral vermiculites	Trioctahedral vermiculite
			Dioctahedral vermiculites	Dioctahedral vermiculite
	Non-hydrated cations	True mica $x \sim 0.5-1.0$	Trioctahedral true micas	Phlogopite, biotite, lepidolite, zinnwaldite, annite, etc.
			Dioctahedral true micas	Muscovite, illite, glauconite, tobelite, paragonite, etc.
	Non-hydrated cations	Brittle mica $x \sim 2.0$	Trioctahedral brittle micas	Clintonite, bityite, anandite, kinoshitalite
			Dioctahedral brittle micas	Margarite
	Hydroxide sheet	Chlorite x variable	Trioctahedral chlorites	Clinochlore, chamosite, nimite, pennantite, baileychlore
			Dioctahedral chlorites	Donbassite
			Di,trioctahedral chlorites	Cookeite, sudoite

* x is charge per formula unit.

$\beta = 105°$

7.15 Å

c axis

6(OH)

4 Al

2(OH) + 4O

4 Si

6 O

b axis

Kaolinite

$\beta = 100°$

9.3 Å

c axis

6 O

4 Si

2(OH) + 4O

4 Al

2(OH) + 4O

4 Si

6 O

b axis
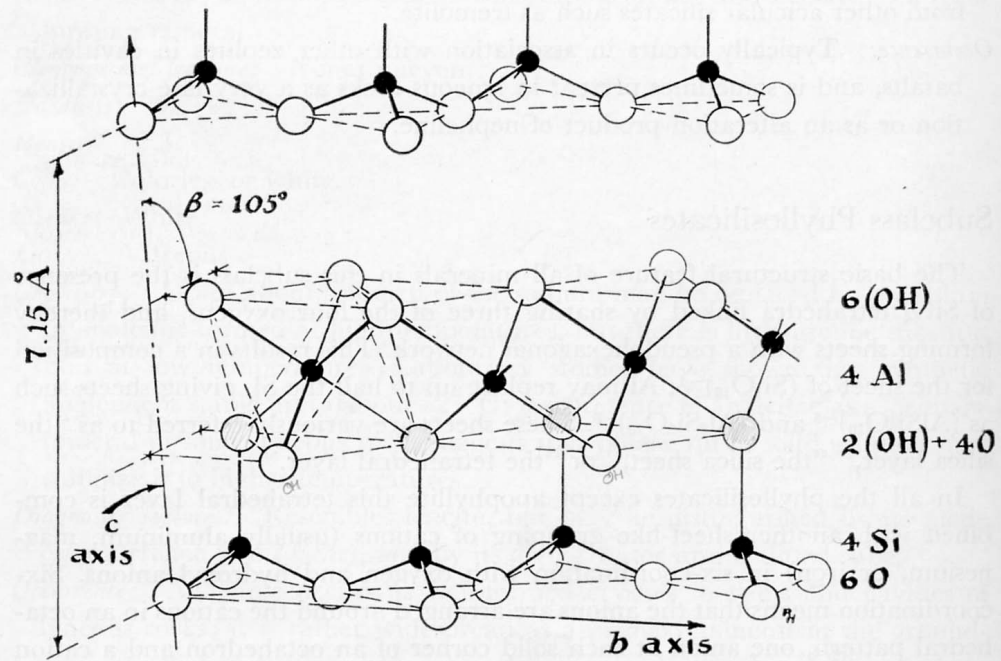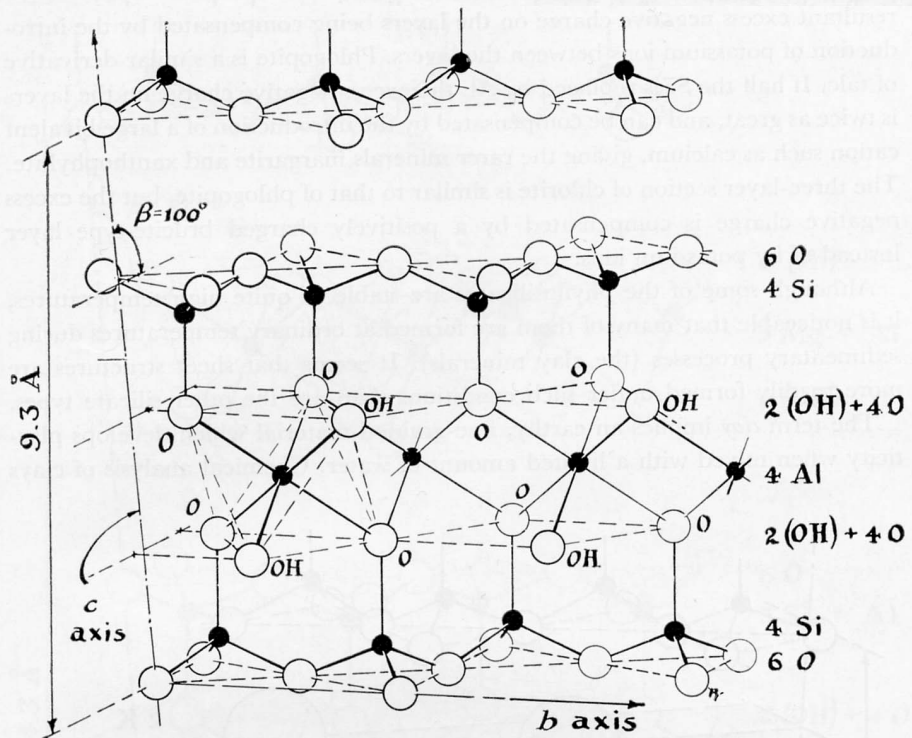
Pyrophillite
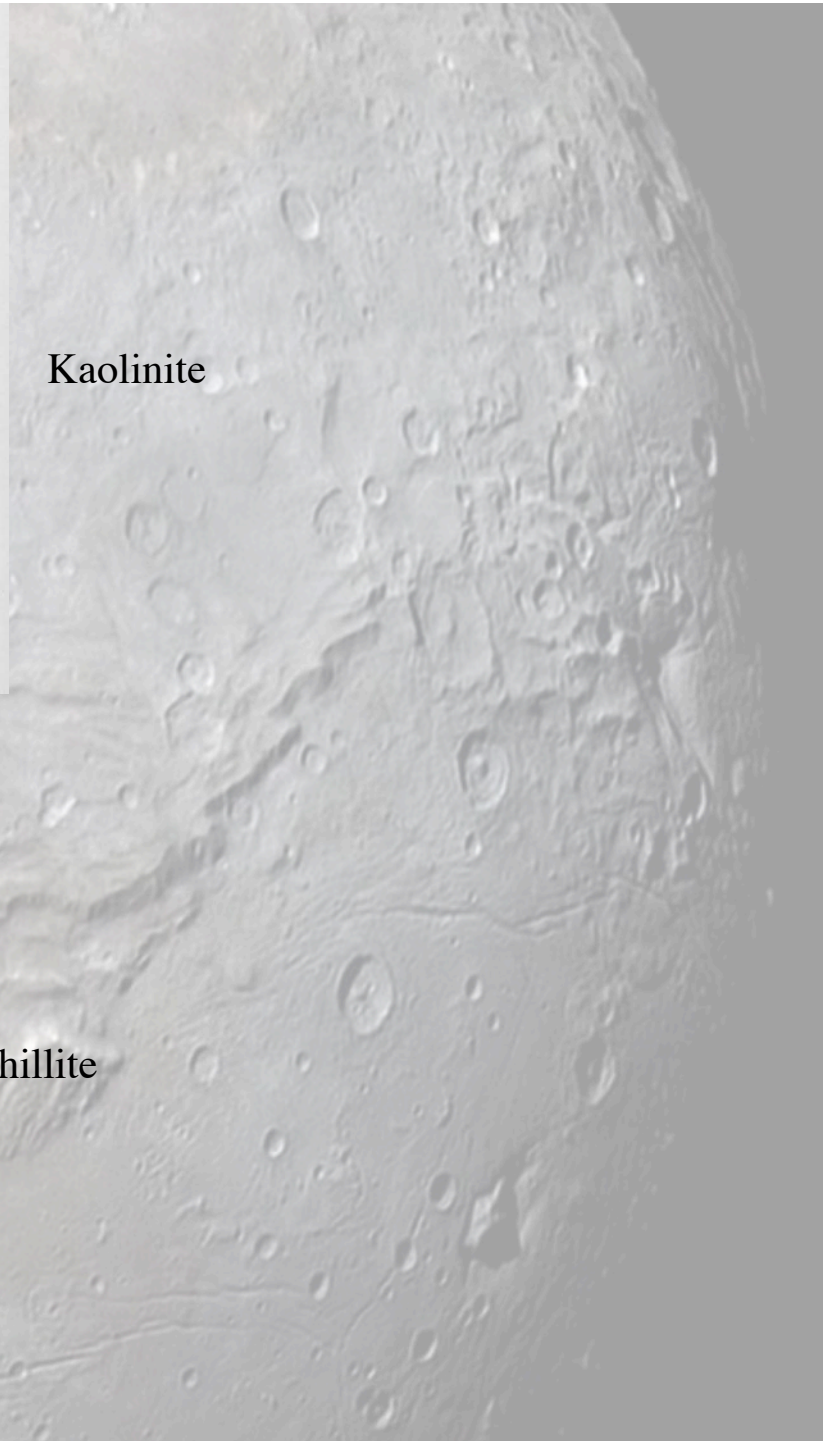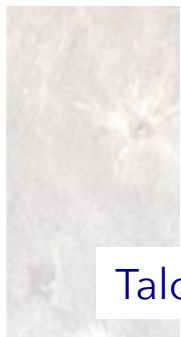
Talc

Hectorite

Saponite

Phlogopite

Biotite

Biotite

FIG. 15.3 (*left*). Hydroxyl absorption of A, talc; B, hectorite; C, saponite; D, phlogopite; E, biotite; F, biotite. The mica spectra were obtained from single flakes at normal (N) and 45° incidence (R). The spectra of hectorite and saponite correspond to anhydrous K-saturated specimens.

FIG. 15.4 (*centre*). Hydroxyl absorption of randomly oriented samples of A, pyrophyllite; B, beidellite; C, rectorite; D, muscovite or paragonite; E, margarite; F, Wyoming montmorillonite; G, Skyrvedalen montmorillonite; H, Woburn montmorillonite; J, nontronite and K, ferric celadonite.

FIG. 15.5 (*right*). Hydroxyl absorption of A, kaolinite; B, dickite; C, nacrite; D, Pugu kaolin (disordered). R indicates randomly oriented specimens, and N films at normal incidence. Spectra (Figs 3, 4, 5) from Farmer and Russell (1964).

WAVELENGTH (MICRONS)
2·70   2·75   2·80   2·85

WAVELENGTH (MICRONS)
2·70   2·75   2·80

Pyrophillite

Beidelite
Rectorite

Muscovite
Margarite
Montmorillonite

Montmorillonite

Montmorillonite

Nontronite

Celadonite (Fe)

3675
3647
3661
3645
3627
3636
3632
3620
3564
3557
3534
3601

3697
3620
3669
3652
3622
3654
3704
3647
3629
3703
3701
3622
3652

FREQUENCY (CM⁻¹)
3750 3700 3650 3600 3550 3500

FREQUENCY (CM⁻¹)
3750 3700 3650 3600 3550

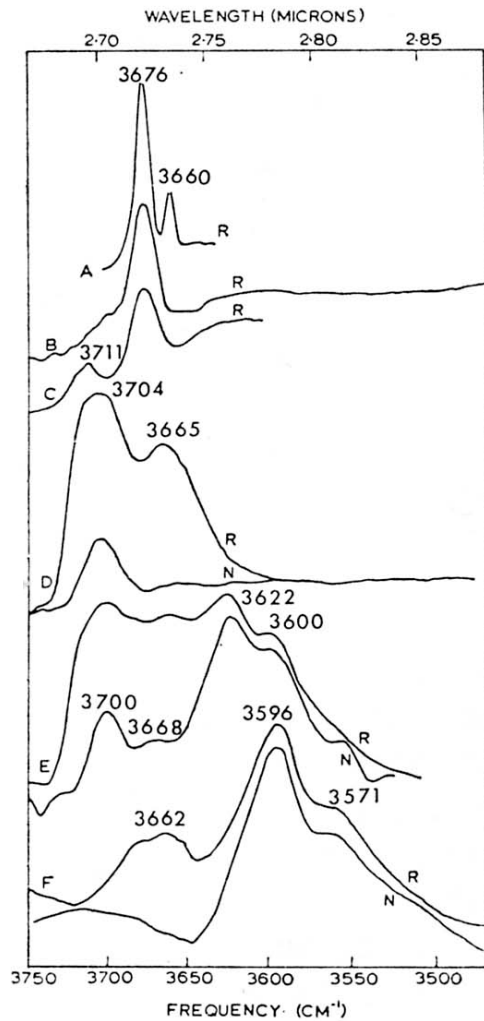FIG. 15.3 (*left*). Hydroxyl absorption of A, talc; B, hectorite; C, saponite; D, phlogopite; E, biotite; F, biotite. The mica spectra were obtained from single flakes at normal (N) and 45° incidence (R). The spectra of hectorite and saponite correspond to anhydrous K-saturated specimens.

FIG. 15.4 (*centre*). Hydroxyl absorption of randomly oriented samples of A, pyrophyllite; B, beidellite; C, rectorite; D, muscovite or paragonite; E, margarite; F, Wyoming montmorillonite; G, Skyrvedalen montmorillonite; H, Woburn montmorillonite; J, nontronite and K, ferric celadonite.

FIG. 15.5 (*right*). Hydroxyl absorption of A, kaolinite; B, dickite; C, nacrite; D, Pugu kaolin (disordered). R indicates randomly oriented specimens, and N films at normal incidence. Spectra (Figs 3, 4, 5) from Farmer and Russell (1964).
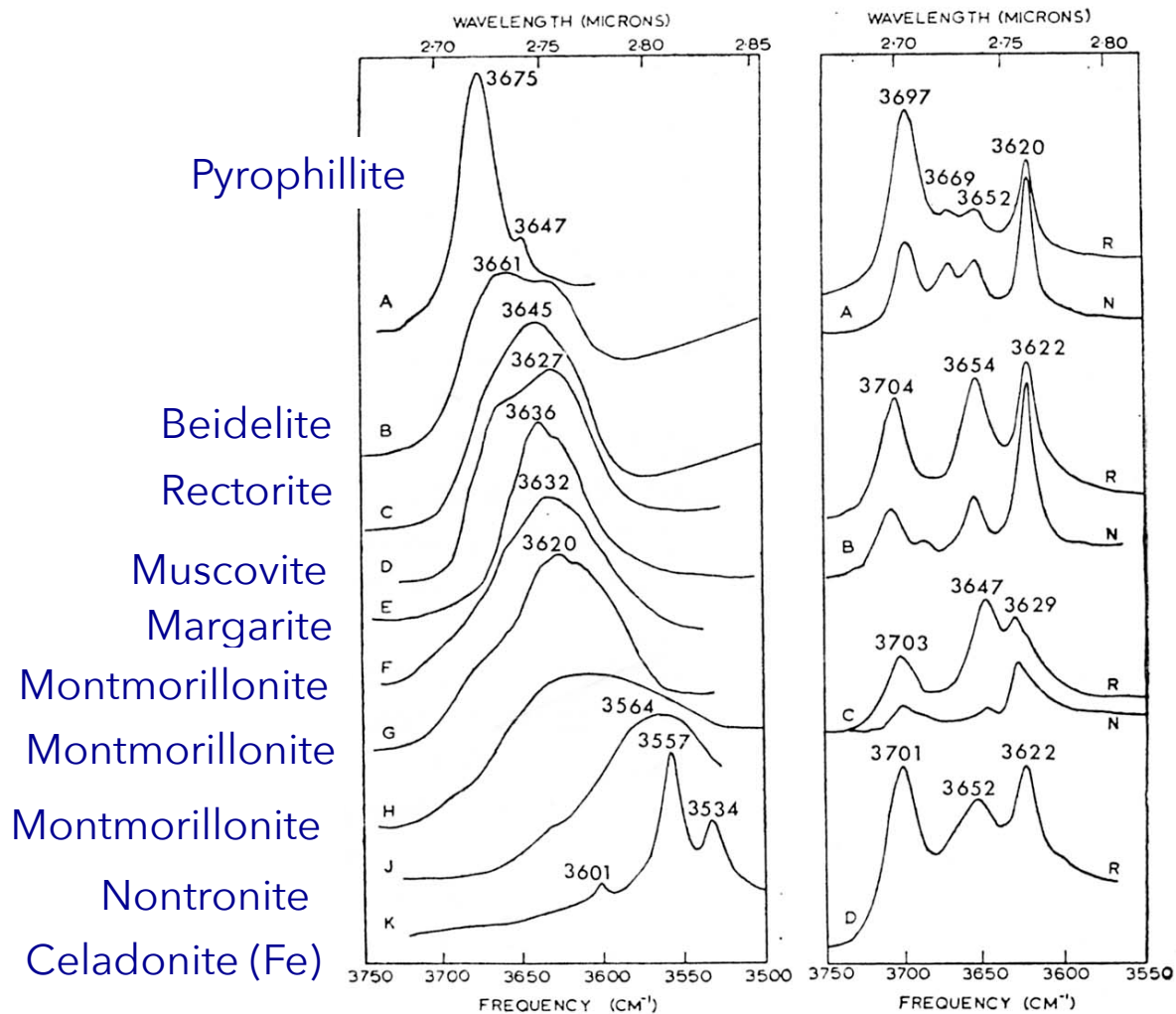
OH cationic environment controls OH peak positions

TABLE 15.I. Band frequencies (cm^{-1}) in the hydroxyl stretching region of the infrared spectrum of some synthetic talcs, from Wilkins and Ito (1967)

| Talc composition	OH ion vibration frequency close to			
	Mg Mg Mg	Mg Mg R	Mg R R	R R R
Mg_{100}	3676·6	—	—	—
$Mg_{84}Ni_{16}$	3676·5	3661·9	3644·8	—
$Mg_{76}Ni_{24}$	3676·6	3662·3	3645·2	3624·1
$Mg_{52}Ni_{48}$	3676·5	3662·5	3645·9	3625·0
$Mg_{28}Ni_{77}$	3676·7	3662·9	3646·2	3625·9
$Mg_1 Ni_{99}$	—	—	3646·9	3627·2
$Mg_{54}Co_{46}$	3677·4	3661·4	3643·3	3622·3
$Mg_{92}Zn_8$	3676·6	3664·4	3649·7	—
$Mg_{86}Zn_{14}$	3676·8	3665·2	3651·6	3634·6
$Mg_{52}Fe_{48}$	3678·3	3663·5	3646·0	3624·2
$Mg_{92}Mn_8$	3677·1	3663·6	3650·0	—
$Mg_{55}Cu_{45}$	3676·0	3669·9	3663·7	3656·3
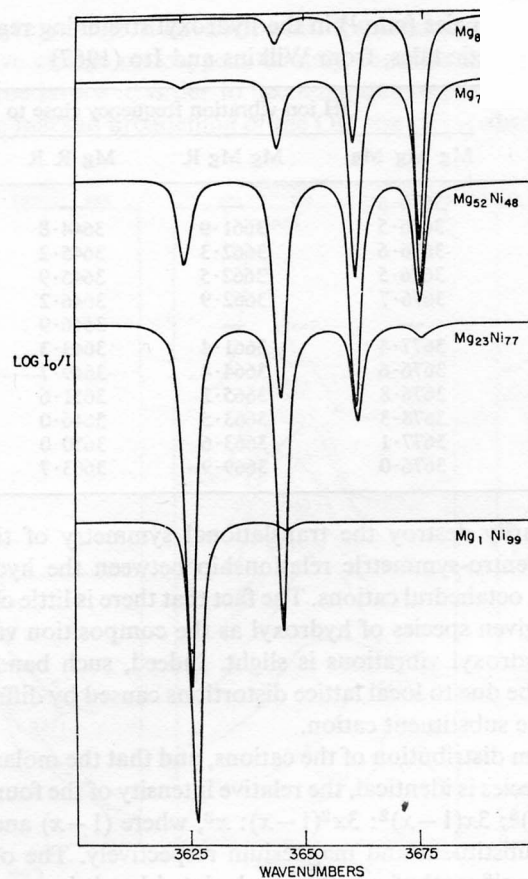
FIG. 15.2. OH stretching vibrations of synthetic Mg–Ni talcs. 5–7·5 mg samples in KBr disks (from Wilkins and Ito, 1967).
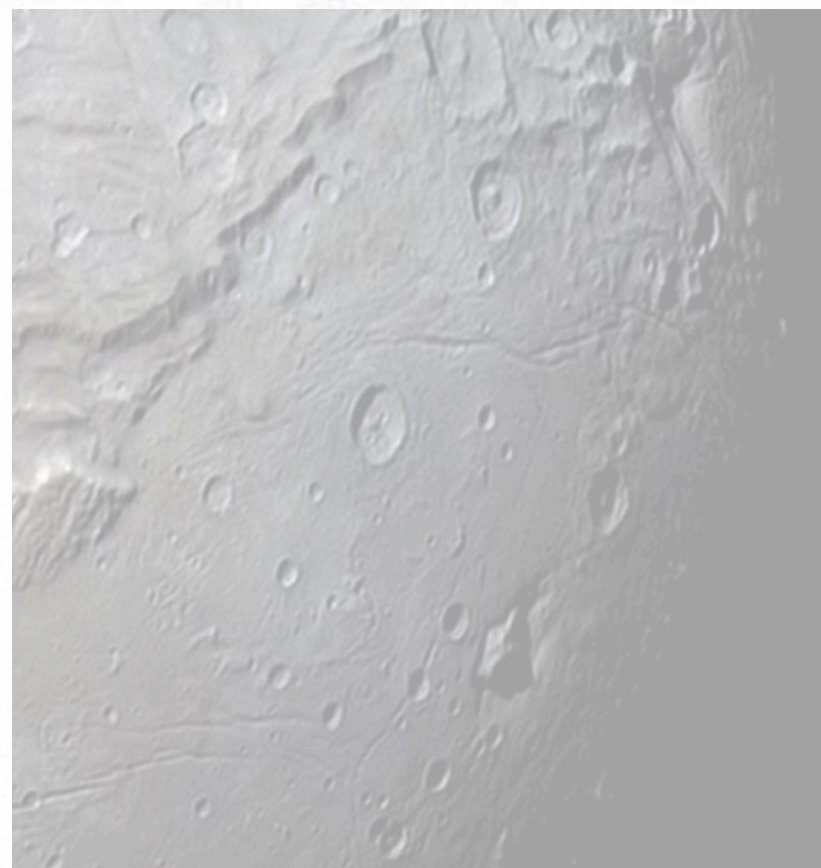
Cations in octahedral layers of micas

Easy to implement
Probe only octahedric catrions bound to OH
Whatever the cation (e.g. NMR, Fe)

Well-known standards

Cation	Zavalye c (I)	69G (II)	31 (III)	B. Patom G (IV)	655 G (V)	Taiheisan c (VI)	E8/2 G (VII)	5/1 (VIII)	Oya c (IX)	933/3 (X)	132 (XI)	133G (XII)	
Si	3·96	3·94	3·94	3·46	3·64	3·72	3·65	3·69	3·99	3·88	3·96	3·84	Si substitution in T
Al_{IV}	0·04	0·06	0·06	0·54	0·36	0·28	0·35	0·31	0·01	0·02	0·04	—	
Fe^{3+}_{IV}										0·10		0·16	
Al_{VI}	0·05	0·05	1·10	1·11	0·08	0·16	0·68	0·13	0·93				
Fe^{3+}_{VI}	0·96	1·15	0·17	0·41	1·08	1·07	0·79	1·30	0·25	1·47	1·32	0·75	In O layer
Fe^{2+}	0·26	0·36	0·07	0·13	0·12	0·14	0·10	0·07	0·44		0·07	1·05	
Mg	0·73	0·41	0·64	0·35	0·66	0·67	0·43	0·50	0·31	0·53	0·54	0·55	
K	0·89	0·83	0·91	0·74	0·90	0·82	0·78	0·78	0·73	0·43	0·65	0·59	
Na		0·01	0·07	0·01		0·18	0·01		0·18	0·08	0·02	0·03	Interfoliar
Ca	0·10	0·03		0·06					0·02	0·02	0·01		
Mg				0·07				0·02		0·05			

TABLE 2. Correlations between OH stretching frequencies and octahedral cations to which the hydroxyl groups are coordinated, and integrated optical densities of IR band (%).

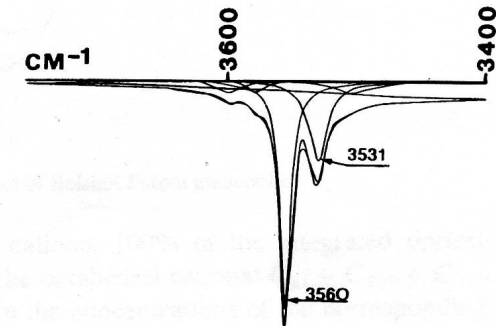| Wave number (cm⁻¹)	Cation pair	Zavalye (I)	69G (II)	31 (III)	B. Patom (IV)	655 (V)	Taiheizan (VI)	E8/2 (VII)	5/1 (VIII)
3495	$Fe^{2+}Fe^{2+}$	—	6·5	—	—	—	—	—	—
3505	MgMg	9·1	3·0	2·9	—	8·4	9·9	—	5·0
3531*	$Fe^{2+}Fe^{3+}$ $Fe^{3+}Fe^{3+}$	30·0	49·8	3·2	20·2	28·0	30·1	14·9	35·9
3545	$Fe^{3+}Fe^{3+}$	—	3·6	—	—	4·3	—	—	11·5
3560	Mg Fe^{3+}	54·0	30·0	16·4	6·9	38·3	35·6	32·8	23·1
3580	Fe^{2+}Al	2·6	—	1·7	8·1	6·8	11·4	7·6	8·9
3605	Mg Al	4·3	6·8	46·8	26·7	10·4	8·8	12·9	12·0
3620	Al Al	—	—	12·8	22·6	3·2	3·3	27·6	3·6
3640	Al Al	—	—	16·2	15·2	0·6	0·9	4·2	—
χ^2		1·55	0·65	0·23	0·29	0·12	0·75	1·01	0·17
* 3528	$Fe^{2+}Fe^{3+}$	21·1	23·0	3·2	6·0	6·3	2·1	0·9	—
* 3534	$Fe^{3+}Fe^{3+}$	8·9	26·8	—	14·2	21·7	28·0	14·0	35·9

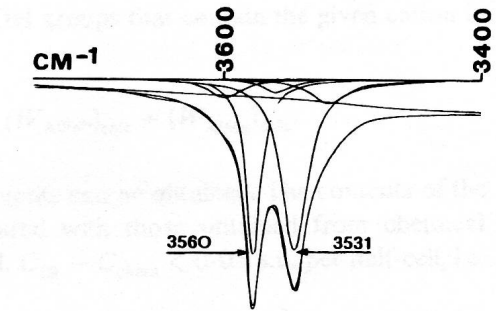FIG. 1. Decomposition of the IR spectrum of Zavalye celadonite.

FIG. 2. Decomposition of the IR spectrum of celadonite 69G.

Lorentzian profiles

Free parameters:
- ✓ **Position**
- ✓ **FWHM**
- ✓ **Integrated intensity**

Absorption coefficient similar for all components

TABLE 2. Correlations between OH stretching frequencies and octahedral cations to which the hydroxyl groups are coordinated, and integrated optical densities of IR band (%).

Wave number (cm⁻¹)	Cation pair	Zavalye (I)	69G (II)	31 (III)	B. Patom (IV)	655 (V)	Taiheizan (VI)	E8/2 (VII)	5/1 (VIII)
3495	$Fe^{2+}Fe^{2+}$	—	6·5	—	—	—	—	—	—
3505	MgMg	9·1	3·0	2·9	—	8·4	9·9	—	5·0
3531*	$Fe^{2+}Fe^{3+}$ $Fe^{3+}Fe^{3+}$	30·0	49·8	3·2	20·2	28·0	30·1	14·9	35·9
3545	$Fe^{3+}Fe^{3+}$	—	3·6	—	—	4·3	—	—	11·5
3560	Mg Fe^{3+}	54·0	30·0	16·4	6·9	38·3	35·6	32·8	23·1
3580	Fe^{2+}Al	2·6	—	1·7	8·1	6·8	11·4	7·6	8·9
3605	Mg Al	4·3	6·8	46·8	26·7	10·4	8·8	12·9	12·0
3620	Al Al	—	—	12·8	22·6	3·2	3·3	27·6	3·6
3640	Al Al	—	—	16·2	15·2	0·6	0·9	4·2	—
χ^2		1·55	0·65	0·23	0·29	0·12	0·75	1·01	0·17
*{ 3528	$Fe^{2+}Fe^{3+}$	21·1	23·0	3·2	6·0	6·3	2·1	0·9	—
3534	$Fe^{3+}Fe^{3+}$	8·9	26·8	—	14·2	21·7	28·0	14·0	35·9

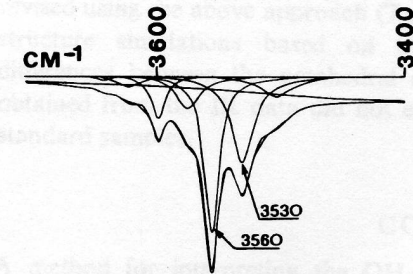FIG. 5. Decomposition of the IR spectrum of gauconite 655.

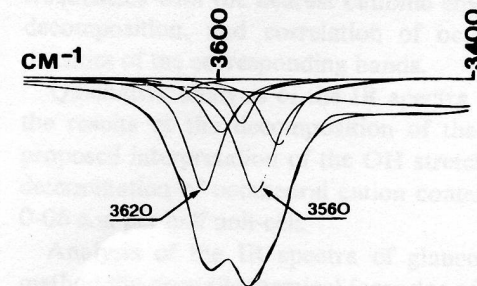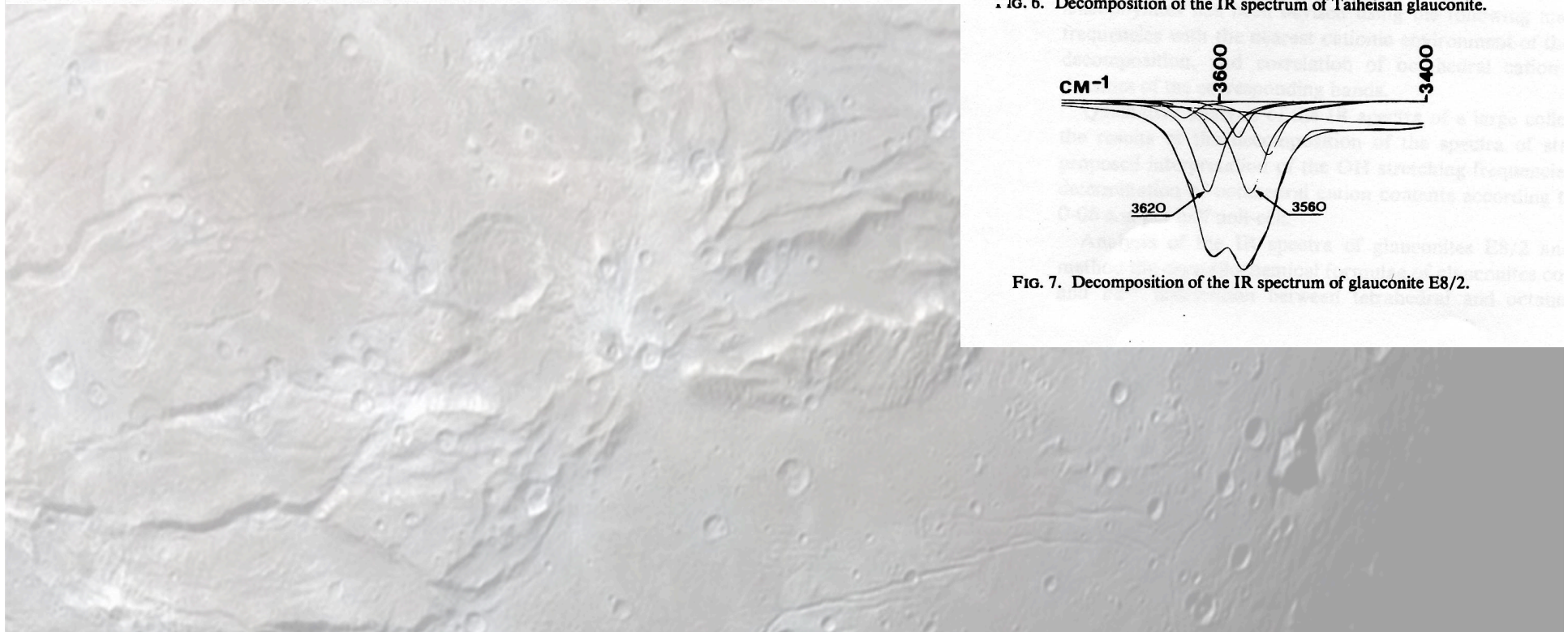FIG. 6. Decomposition of the IR spectrum of Taiheisan glauconite.

FIG. 7. Decomposition of the IR spectrum of glauconite E8/2.

TABLE 2. Correlations between OH stretching frequencies and octahedral cations to which the hydroxyl groups are coordinated, and integrated optical densities of IR band (%).

Wave number (cm^{-1})	Cation pair	Zavalye (I)	69G (II)	31 (III)	B. Patom (IV)	655 (V)	Taiheizan (VI)	E8/2 (VII)	5/1 (VIII)
3495	$Fe^{2+}Fe^{2+}$	—	6·5	—	—	—	—	—	—
3505	MgMg	9·1	3·0	2·9	—	8·4	9·9	—	5·0
3531*	$Fe^{2+}Fe^{3+}$ $Fe^{3+}Fe^{3+}$	30·0	49·8	3·2	20·2	28·0	30·1	14·9	35·9
3545	$Fe^{3+}Fe^{3+}$	—	3·6	—	—	4·3	—	—	11·5
3560	Mg Fe^{3+}	54·0	30·0	16·4	6·9	38·3	35·6	32·8	23·1
3580	Fe^{2+}Al	2·6	—	1·7	8·1	6·8	11·4	7·6	8·9
3605	Mg Al	4·3	6·8	46·8	26·7	10·4	8·8	12·9	12·0
3620	Al Al	—	—	12·8	22·6	3·2	3·3	27·6	3·6
3640	Al Al	—	—	16·2	15·2	0·6	0·9	4·2	—
χ^2		1·55	0·65	0·23	0·29	0·12	0·75	1·01	0·17
* { 3528	$Fe^{2+}Fe^{3+}$	21·1	23·0	3·2	6·0	6·3	2·1	0·9	—
{ 3534	$Fe^{3+}Fe^{3+}$	8·9	26·8	—	14·2	21·7	28·0	14·0	35·9

FIG. 3. Decomposition of the IR spectrum of leucophyllite 31.
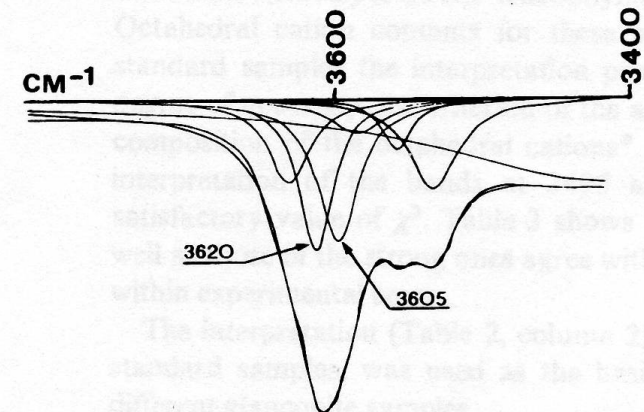
FIG. 4. Decomposition of the IR spectrum of Bolshoi Patom glauconite.

$C_{Al}+C_{Fe3}+C_{Fe2}+C_{Mg}=2$

$$C_{Al} = (2W_{AlAl})_{calc} + (W_{AlFe^{2+}})_{calc} + (W_{AlFe^{3+}})_{calc} + (W_{AlMg})_{calc}.$$

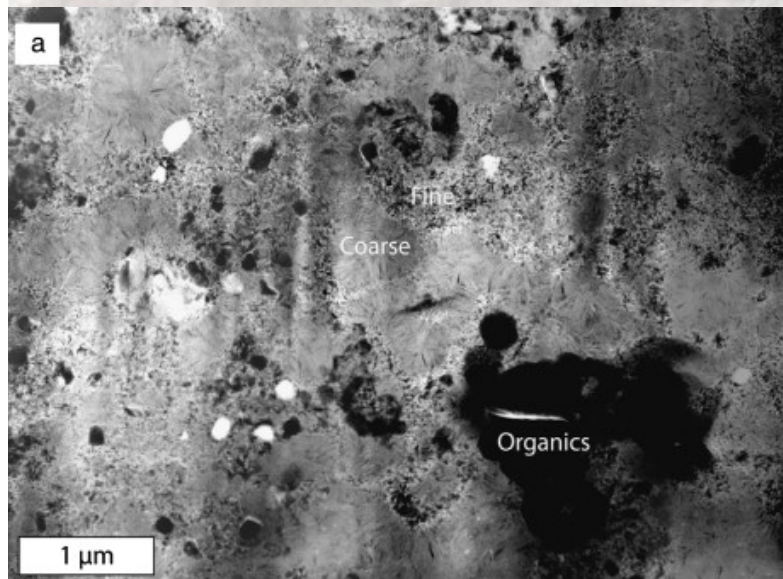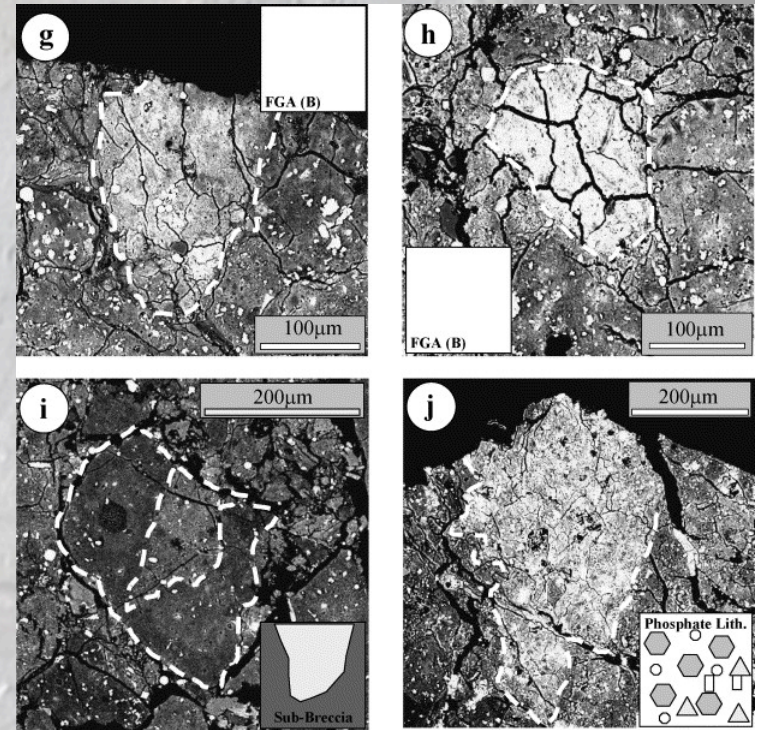W : Integrated absorbance of the Lorentzian component

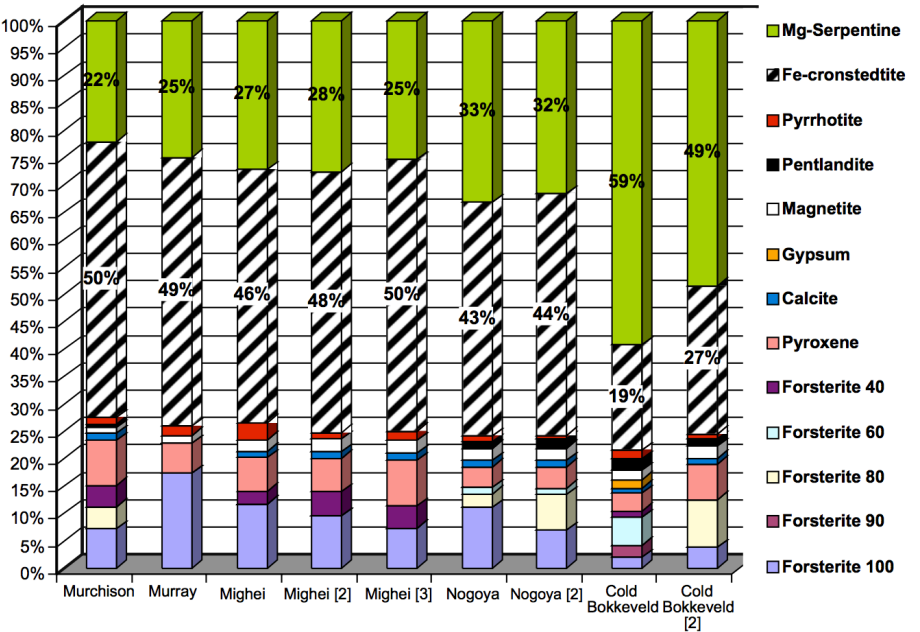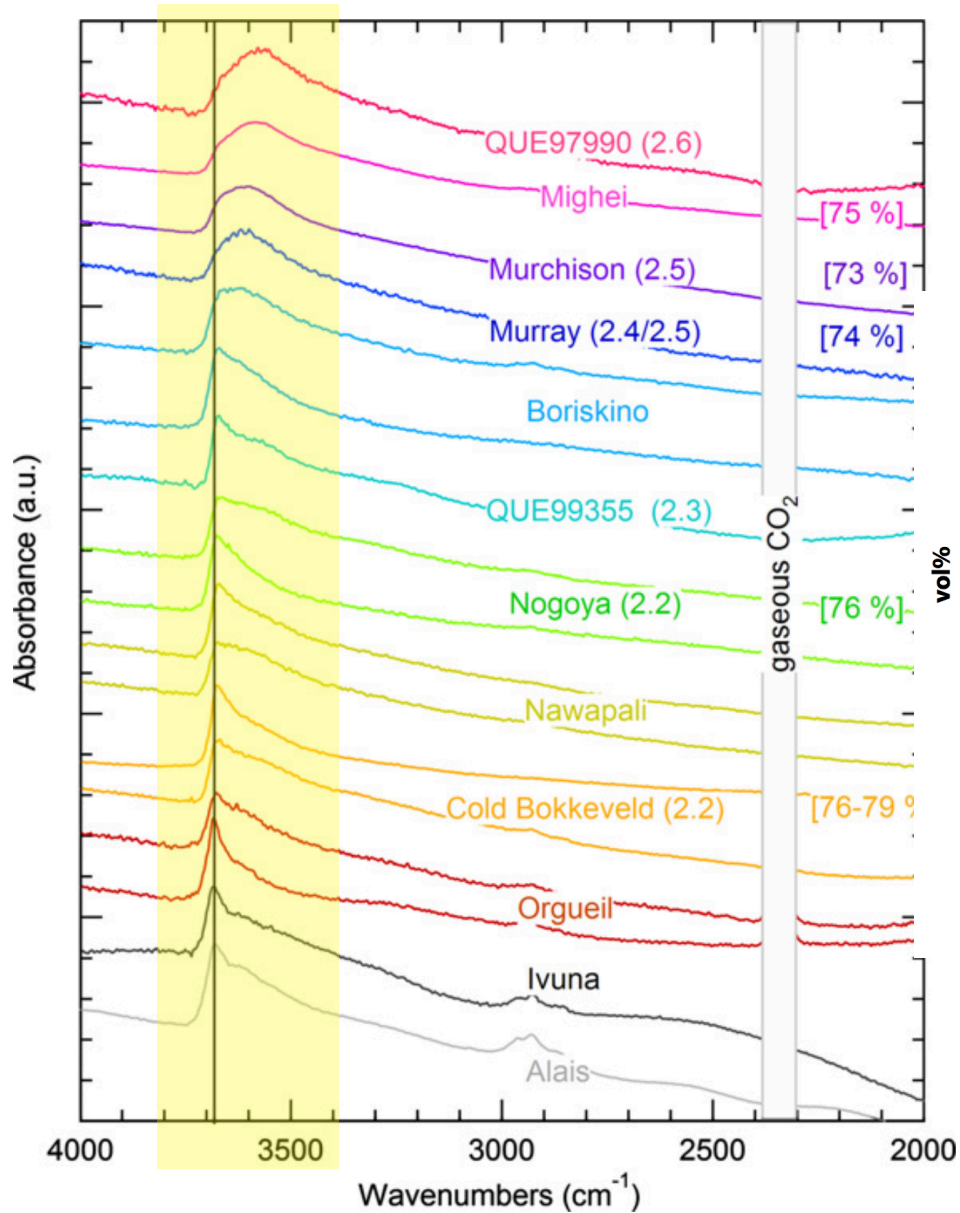# Insights into long and short range orders in extraterrestrial proto-serpentines
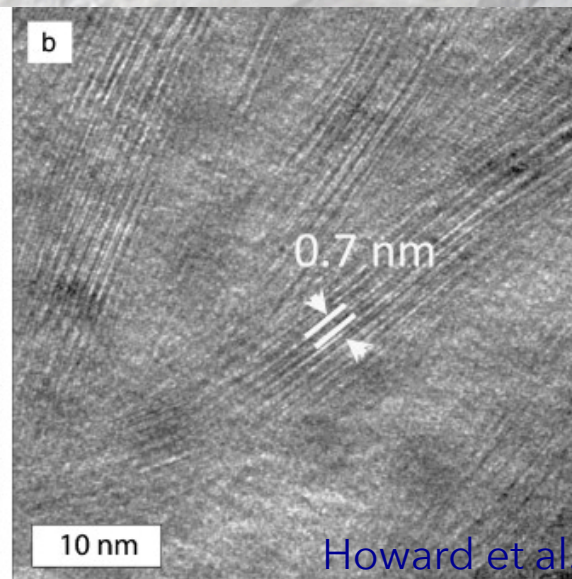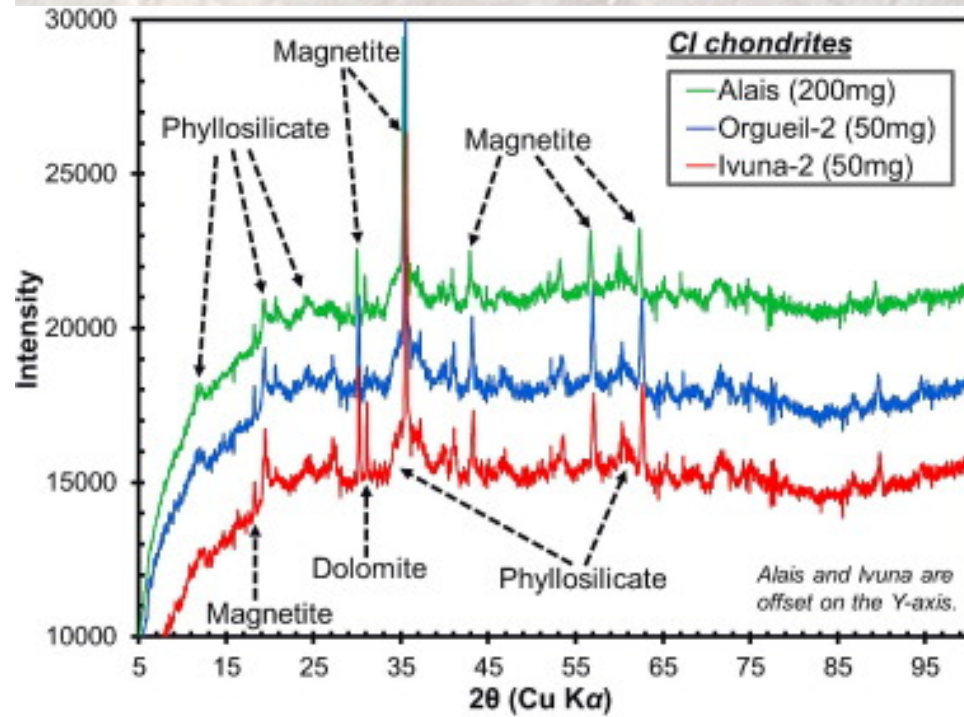
Howard et al., 2014; Leguillou et al. 2015

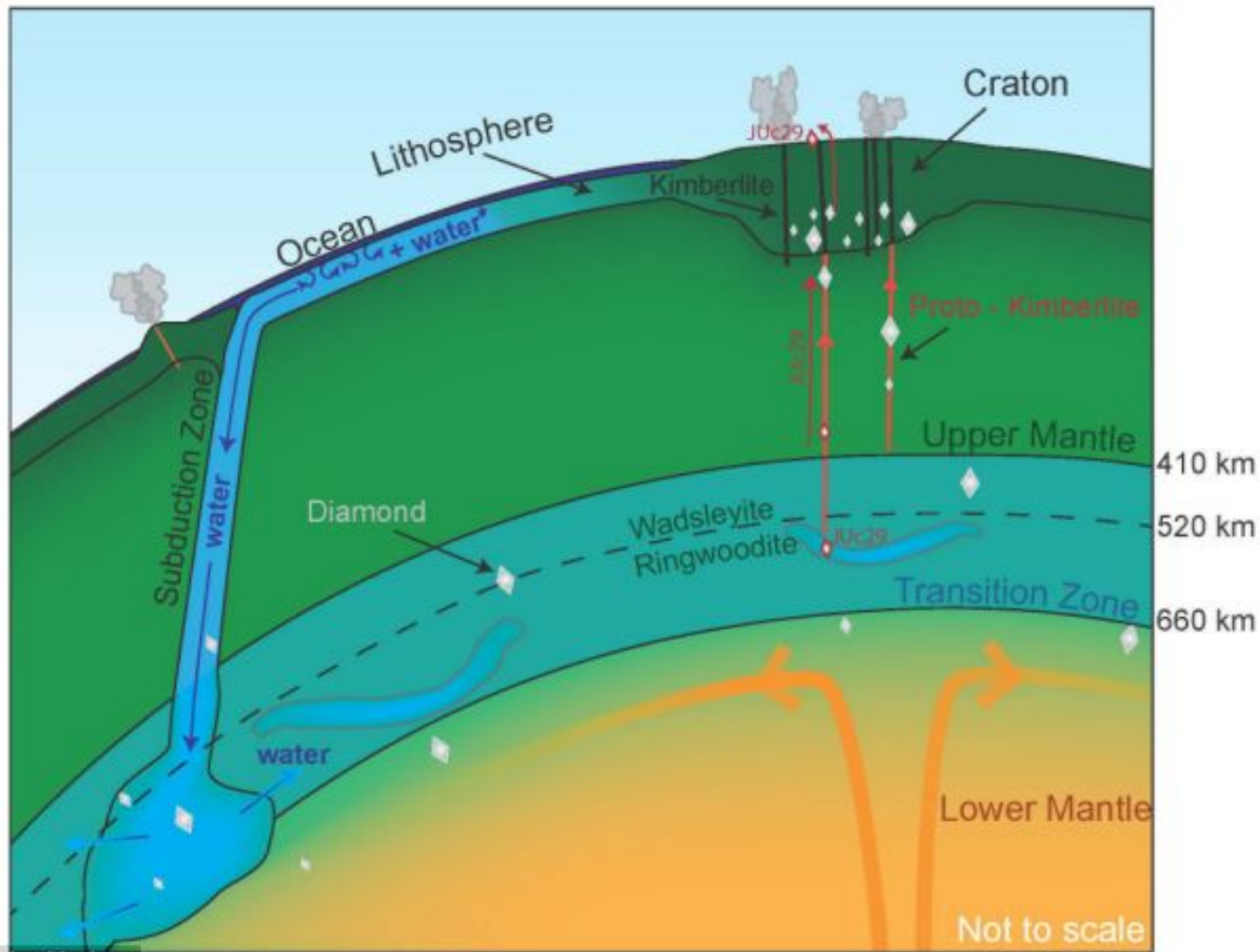Insights into long and short range orders in extraterrestrial proto-serpentines
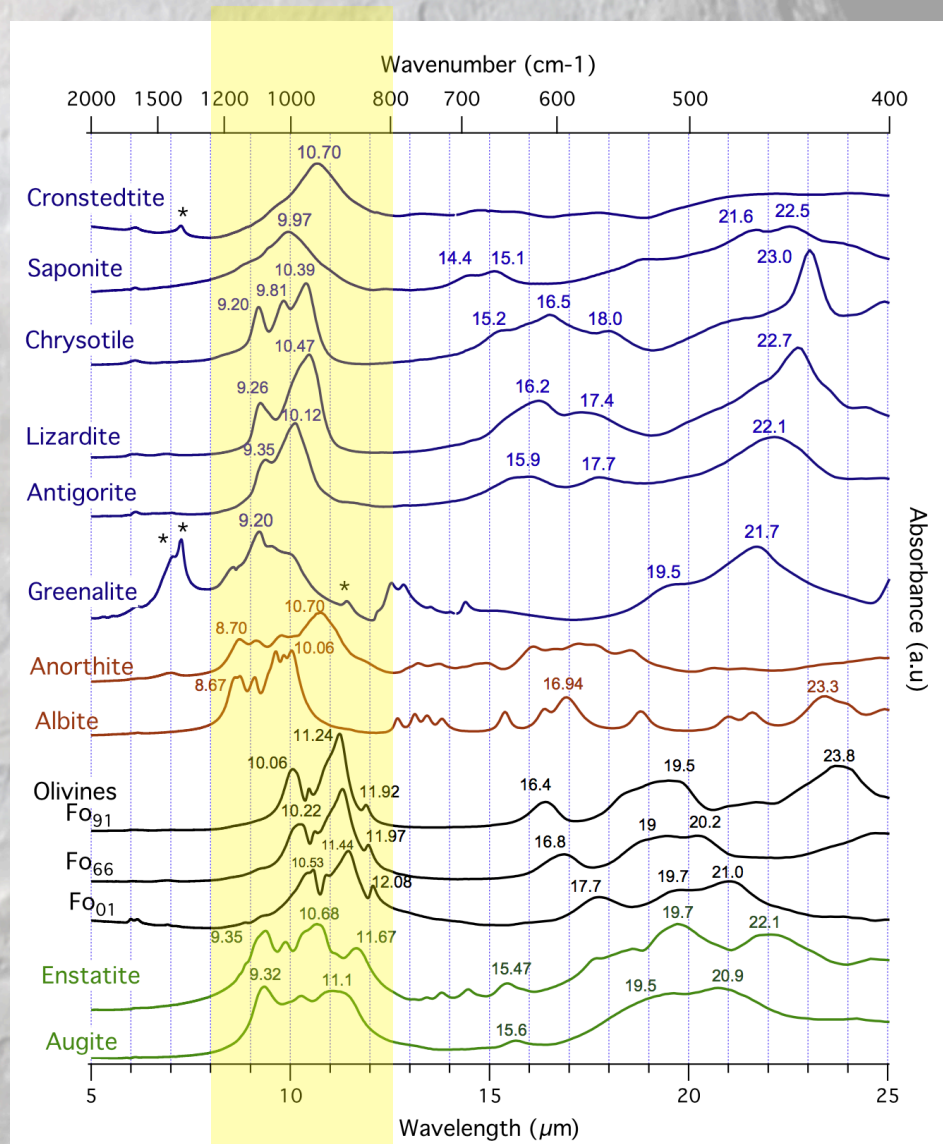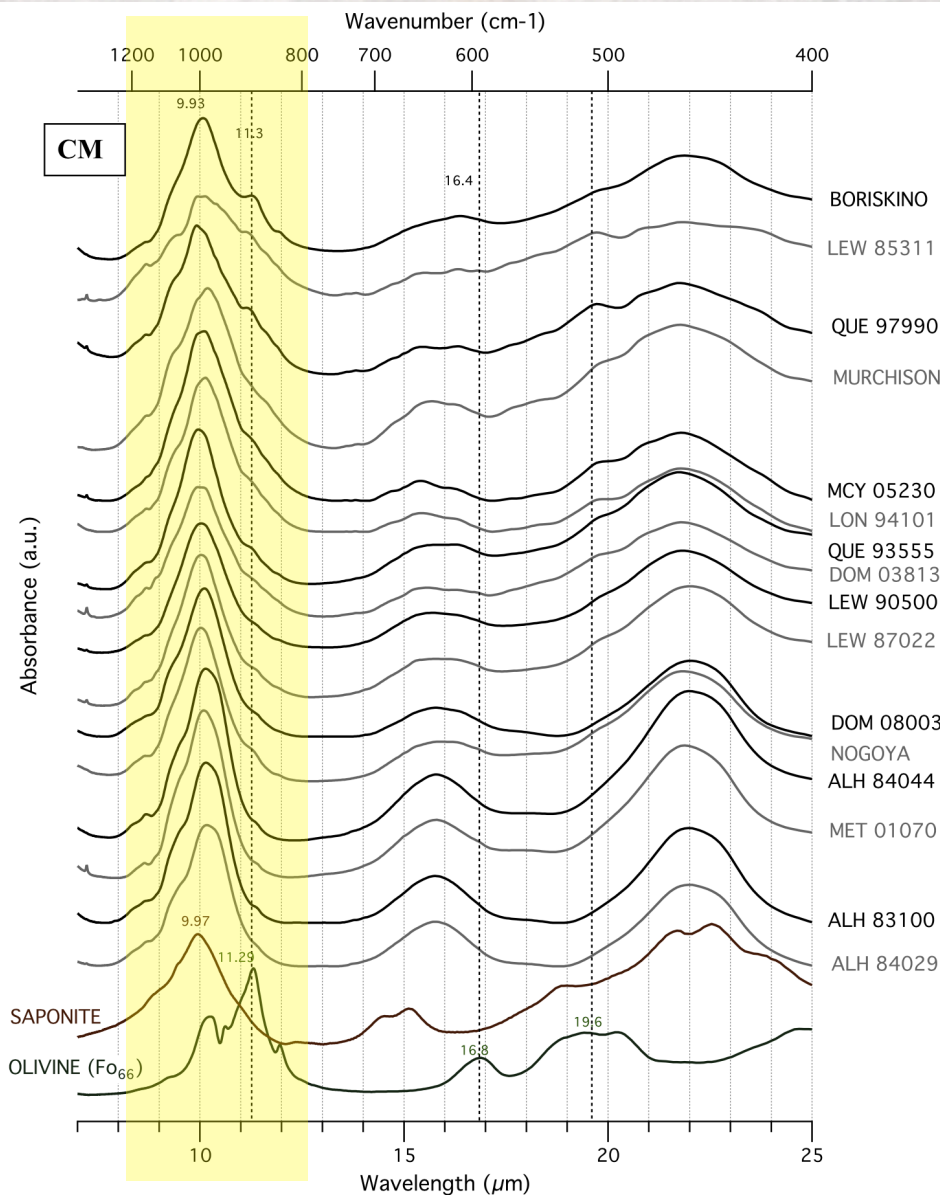
Beck et al., 2014

Fe/Mg ratio controls with and position of 3 μm OH feature
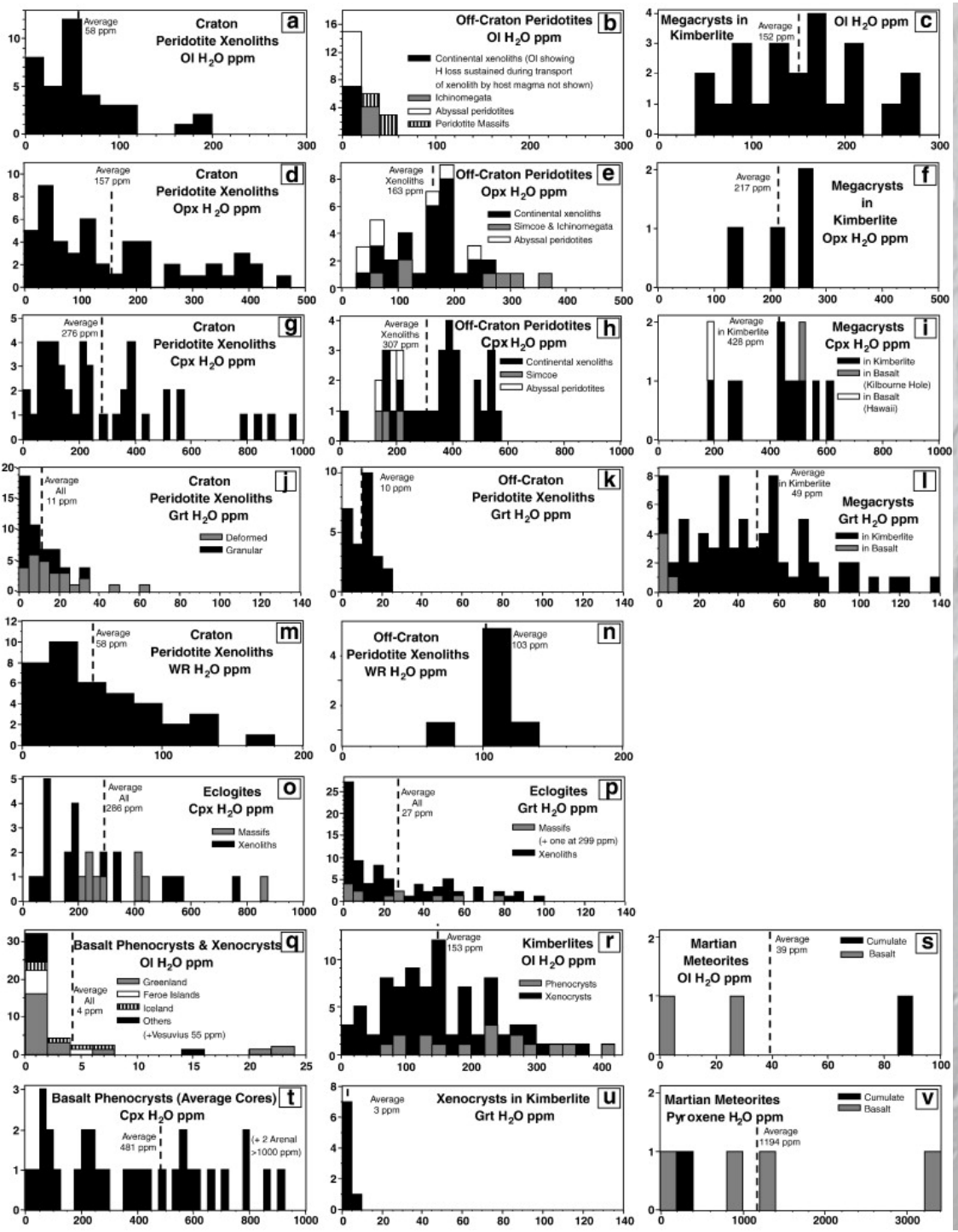

Howard et al., 2009; Beck et al., 2010
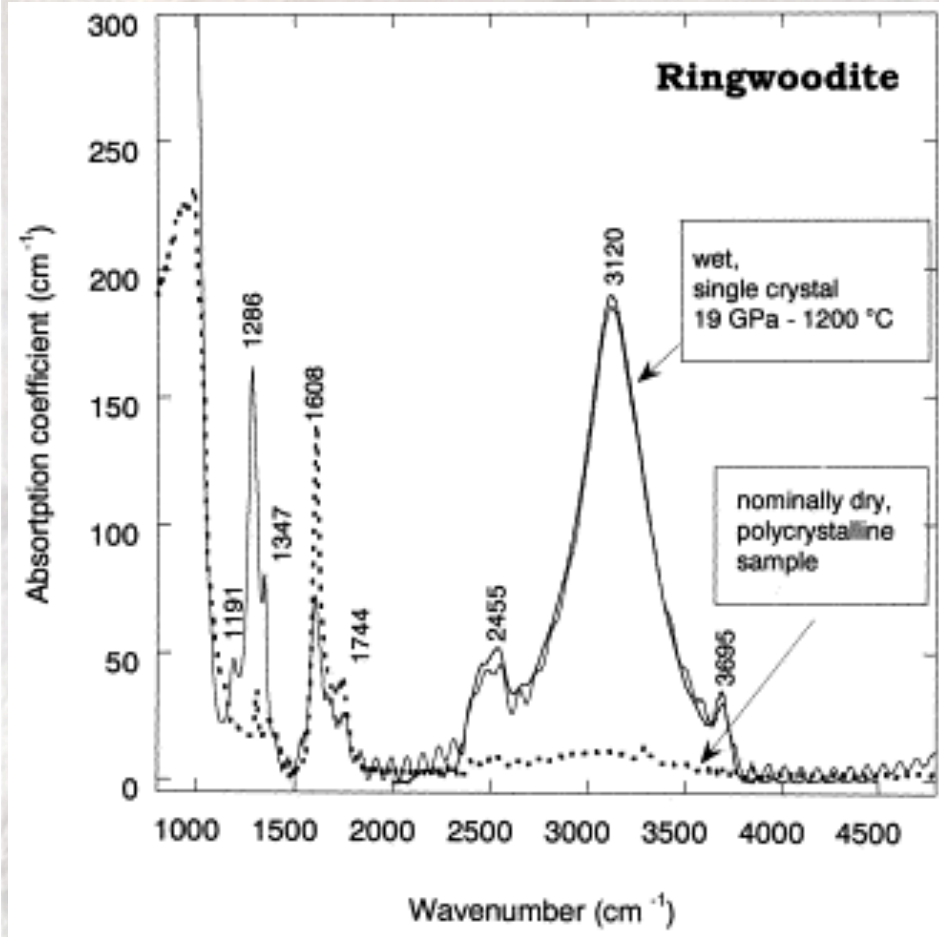
Water in Earth mantle: where and how much?
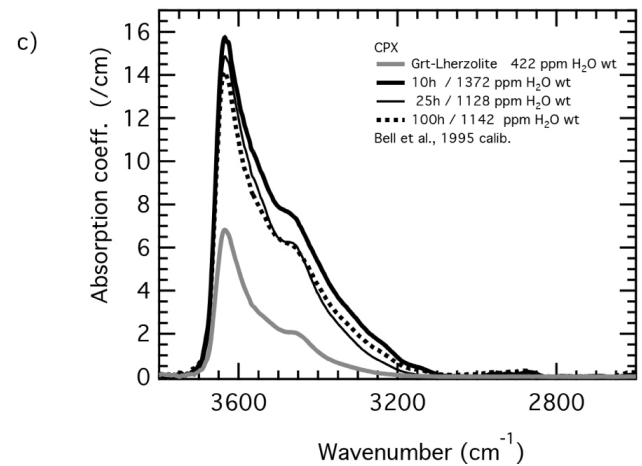

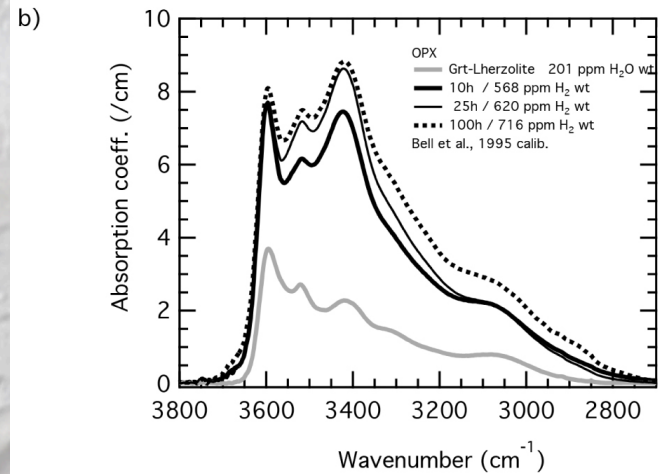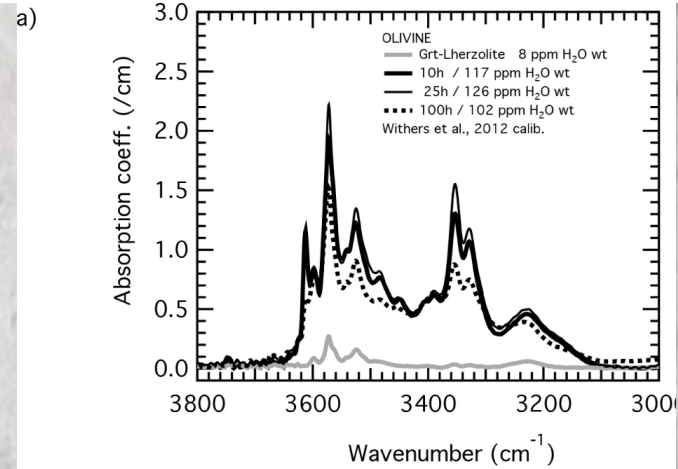**Water reservoir as large as oceans ?!**

- hydrated mineals (phyllosilicates, amphiboles, ...)
- nominally anhydrous minerals (olivines, pyroxenes, ringwoodite, ...)

Ringwoodite

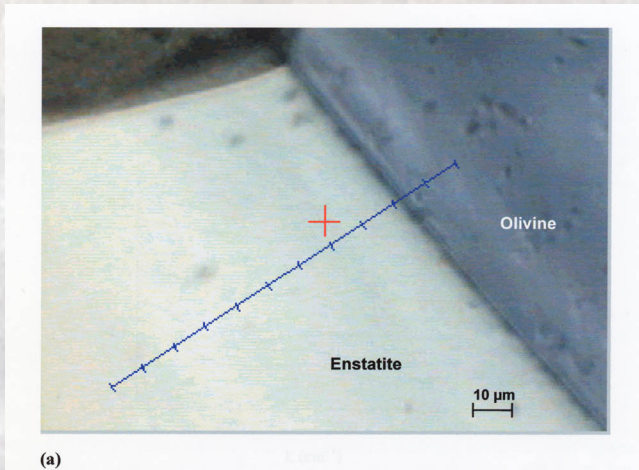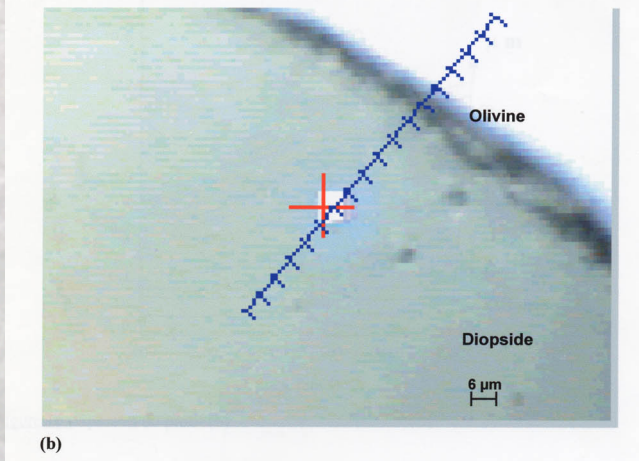wet, single crystal 19 GPa - 1200 °C

nominally dry, polycrystalline sample

Bolfan-Casanova et al. EPSL 2000

Demouchy et al. Am Min. 2017

a) OLIVINE
- Grt-Lherzolite 8 ppm H_2O wt
- 10h / 117 ppm H_2O wt
- 25h / 126 ppm H_2O wt
- 100h / 102 ppm H_2O wt
- Withers et al., 2012 calib.

b) OPX
- Grt-Lherzolite 201 ppm H_2O wt
- 10h / 568 ppm H_2 wt
- 25h / 620 ppm H_2 wt
- 100h / 716 ppm H_2 wt
- Bell et al., 1995 calib.

c) CPX
- Grt-Lherzolite 422 ppm H_2O wt
- 10h / 1372 ppm H_2O wt
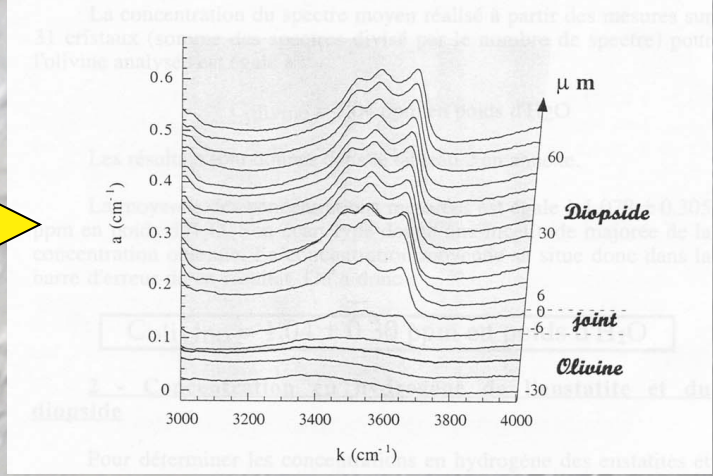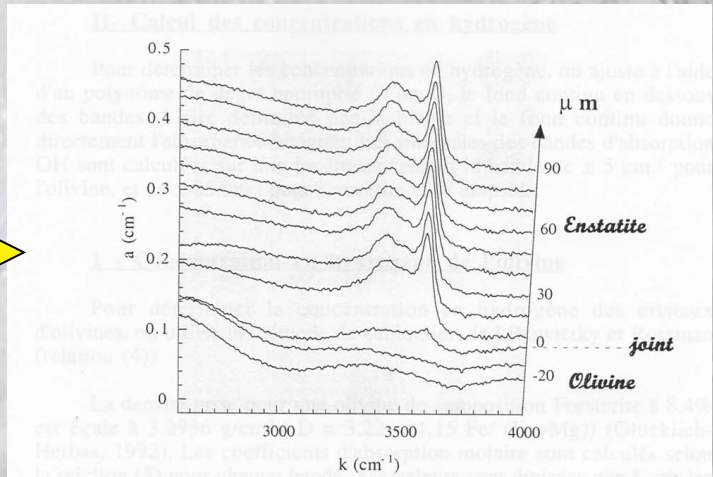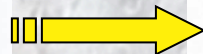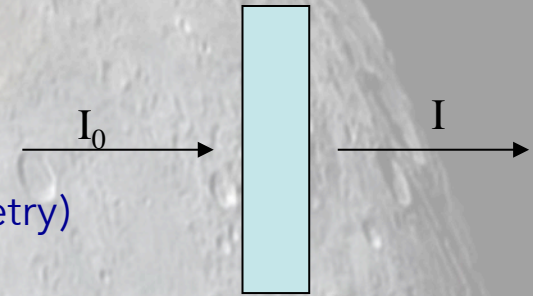- 25h / 1128 ppm H_2O wt
- 100h / 1142 ppm H_2O wt
- Bell et al., 1995 calib.

After N. Bournhonnet, stage DEA / dir. J. Ingrain Beamline SA5 - LURE (Orsay)

Abundance estimation

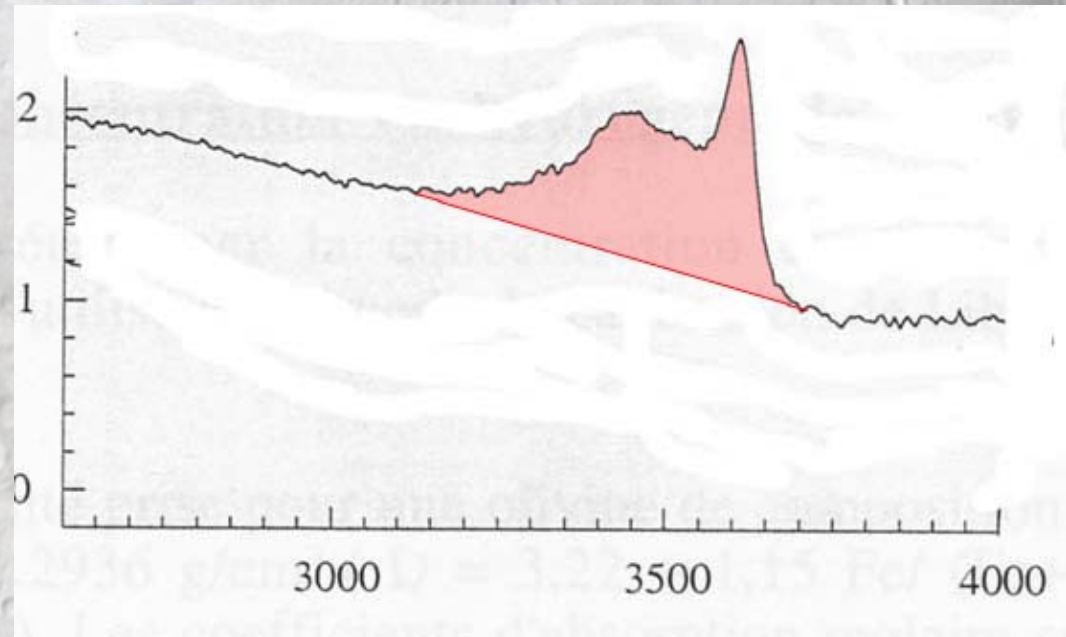Calibration with standards (hydrogen measured by mass spectrometry)

$$I = I_0 \exp(-\alpha.e.c)$$

$$A = \alpha.e.c$$

$$\int A(\sigma)d\sigma = \alpha_i.e.c$$
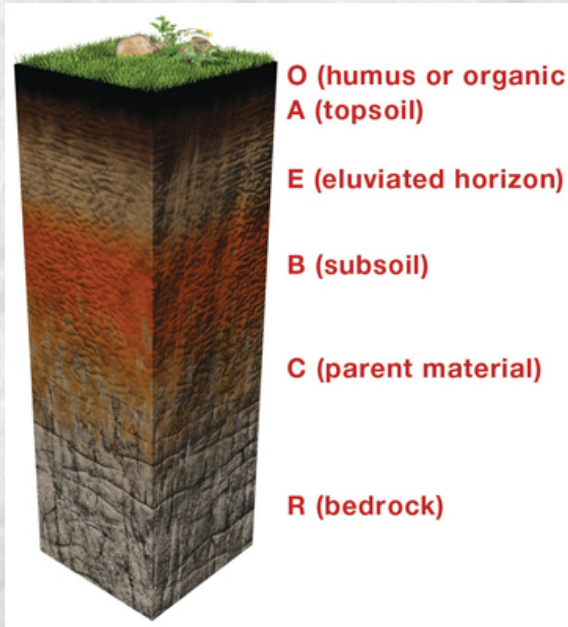
$$c = \frac{1}{\alpha_i e}\int A(\sigma)d\sigma$$

Example:
$C_{enstatite}$ = 174 +/- 32 ppm H_2O (poids) - (ER=20 %)
$C_{diopside}$ = 388 +/- 41 ppm H_2O (poids) - (ER = 10 %)

Soil characterization

O (humus or organic
A (topsoil)

E (eluviated horizon)

B (subsoil)

C (parent material)

R (bedrock)

Humic substances (pigmented polymers)				
Fulvic acid		Humic acid		Humin
Light yellow	Yellow brown	Dark brown	Grey-black	Black

increase in intensity of colour →
increase in degree of polymerization →
2 000 ——— increase in molecular weight ———→ 300 000 ?
45% ——— increase in carbon content ———→ 62%
48% ——— decrease in oxygen content ———→ 30%
1 400 ——— decrease in exchange acidity ———→ 500
decrease in degree of solubility →

Chemical properties of humic substances. (Stevenson 1982)

Model structure of humic acid (Stevenson 1982)
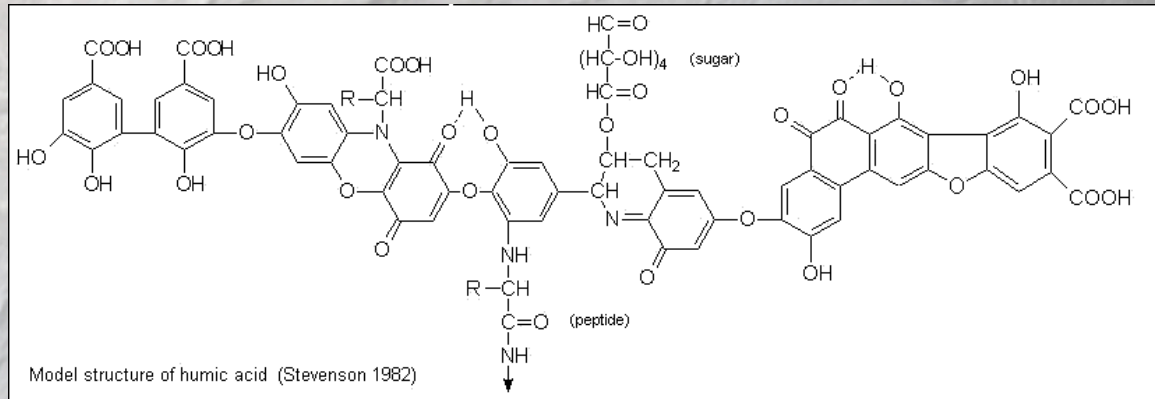
SOM=Soil Organic Matter
Via HF
HS = humic substance
Via NaOH
HA=Humic Acid
FA=Fulvic acid
Purification (resin, HF/Hcl)

Oxidation = H2O2

Aliphatic+ in SOM
Carbonyl+
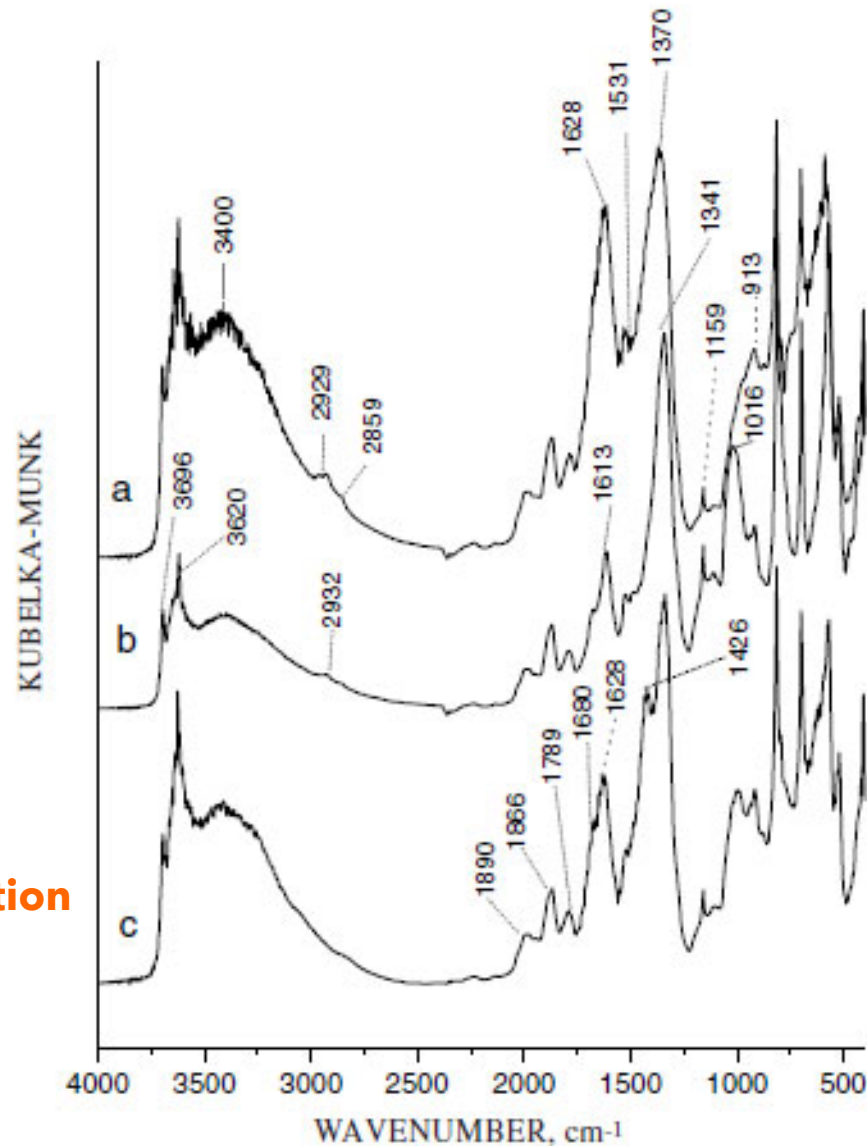**Effect of HF+alkaline extraction**

Figure 1. DRIFT spectra of the whole soil (a), of the HS-extracted soil (b) and of the oxidized soil (c) of the Chernosol.

Multi-variate statistical approaches

Waruru et al. 2015, Soils and Foundations
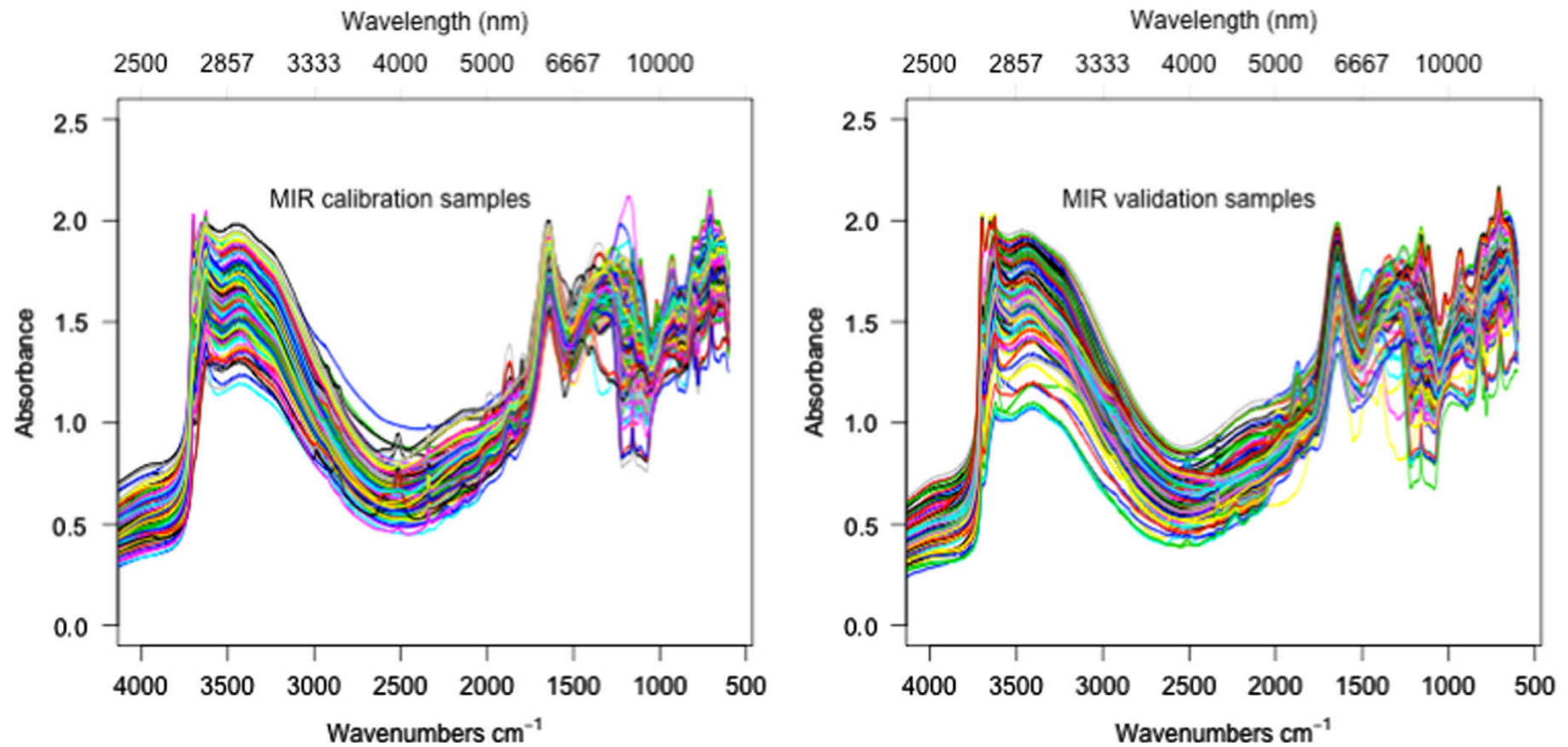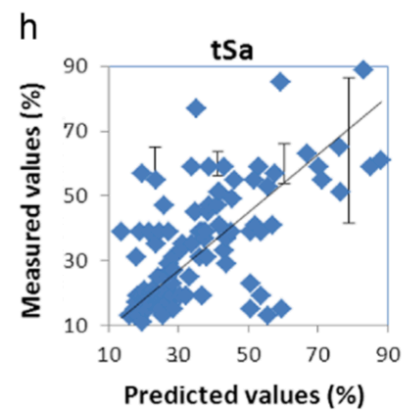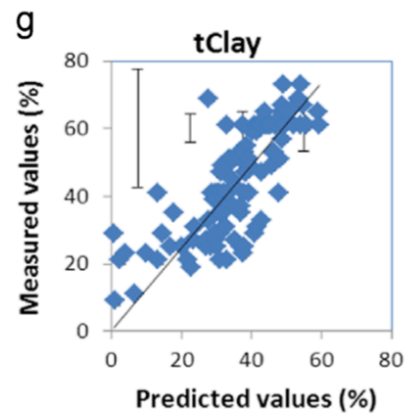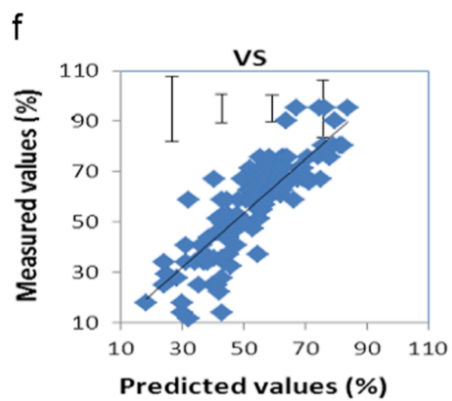
Estimate soil quality for ingeneering purposes

Fig. 6. Mid-infrared absorbance spectra for calibration ($n=135$) and validation ($n=120$) of soil samples after removal of the noisy part (< 600 cm^{-1}) of the signal (spectra is shown in both wavenumbers (cm^{-1}) and wavelength (nm) for easy reference, where [(10,000,000/wavenumbers)$=$wavelength)].
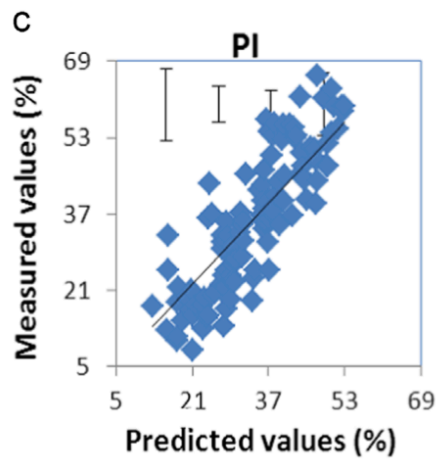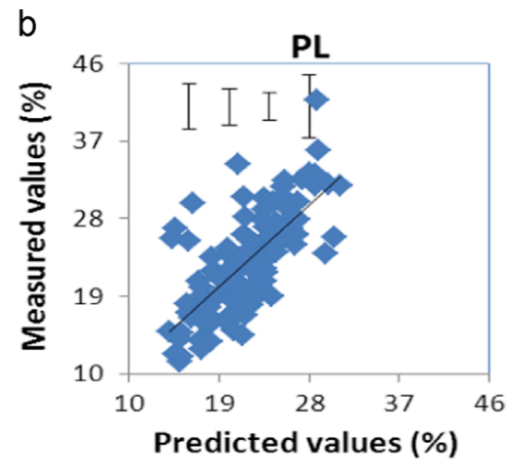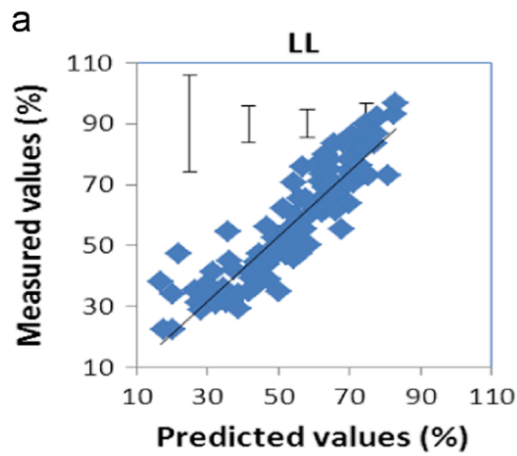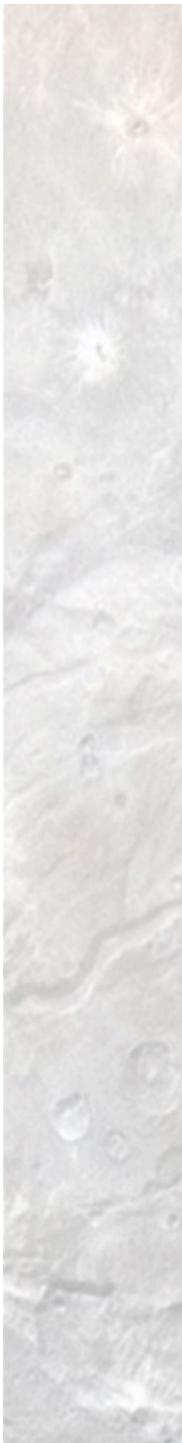
Table 1
Soil properties and methods.

Soil property	Method of determination	Reference
Air-dried moisture content (**W**)	Gravimetric (%)	Islam et al. (2003)
Particle-size distribution tClay, tSi, tSa	Hydrometer (%)	Gee and Bauder (1986)
Exchangeable Ca (eCa), Mg (eMg)	1:10 soil-to-1.0 N KCL extraction followed by AAS (cmol(+)kg^{-1})	Shepherd and Walsh (2002)
Exchangeble Na (eNa)	1:10 soil-to-1.0 N KCL extraction followed by AES (cmol(+) kg^{-1})	Shepherd and Walsh (2002)
Exchangeable K (eK)	1:10 soil-to-modified Olsen solution extraction followed by AAS (cmol(+)kg^{-1})	Shepherd and Walsh (2002)
Cation exchange capacity (CEC)	Sum of eCa+eMg+eNa+eK (cmol(+)kg^{-1})	Shepherd and Walsh (2002)
ESP	Ratio [(eNa/CEC)*100] (%)	Viscarra Rossel et al. (2008)
Sodium-ion concentration	1:5 soil-to-water extract read on Na-ion electrode meter (Na5, mg kg^{-1})	Irvine and Reid (2001)
Soil organic carbon (SOC)	Dry combustion using CN analyzer (%)	Viscarra Rossel et al., 2008
Atterberg limits: LL, PL, LS	BSI BS: 1377 (%)	BSI (1975)
Plasticity index (PI)	Numeric difference (PI=LL−PL) (%)	BSI (1975)
Coefficient of extensibility (COLE)	from LS data [(COLE=(Lm−Ld)/Ld)] (unit); where Lm=length moist soil (=140 mm), Ld=length dry soil (140–LS mm)	Igwe (2003)
Volumetric shrinkage (VS)	From COLE data, VS=[(COLE+1)^3−1]*100 (%)	Igwe (2003)
Activity number (A)	A=PI/tClay (%)	Fratta et al. (2007)